The Dissertation Committee for Ganesh Vijayaraghavan Certifies that this is the approved version of the following dissertation:

Synthesis and Characterization of Carbon Nanotube Supported Nanoparticles for Catalysis

Committee:

Keith J. Stevenson, Supervisor

Jennifer S. Brodbelt

Bert D. Chandler

Arumugam Manthiram

David A. Vanden Bout

Synthesis and Characterization of Carbon Nanotube Supported Nanoparticles for Catalysis

by

Ganesh Vijayaraghavan, B.Tech.; M.S.

Dissertation

Presented to the Faculty of the Graduate School of
The University of Texas at Austin
in Partial Fulfillment
of the Requirements
for the Degree of

Doctor of Philosophy

The University of Texas at Austin
December 2007

Dedication

To S.R and V.V

Acknowledgments

I would like to thank Keith Stevenson for the opportunity to be a part of his research group and learn from him. I have benefitted tremendously in both professional and personal aspects under his guidance.

I would also like to thank members of the Stevenson research group for all their help and support. Stephen Maldonado was a huge help right from the beginning. I'd like to thank Steve for his dedication to the CNT project and offering sane advice when I needed it most. I wish him luck on his pursuit in academia. Tim Smith was helpful whenever I needed help with the lab instrumentation. I'd like to thank Jen Lyon or adding a touch of color to the lab and insightful discussions. Ryan Williams was of great help in analyzing samples on the SEM and the AFM. I'd also like to thank Ryan for help with labView. I'd like to thank Ben Hahn and Lilia Kondrachova for equally insightful discussions and help with the XPS analyses and ITO samples. I'd like to wish the best of luck to Jaclyn Wiggins and Cori Atkinson with their projects and thank them for unique perspectives on their respective areas of research.

I'd like to thank the undergraduate researchers at the Stevenson lab for bringing fresh insight and energy into the lab. I'd like to thank Sawyer Croley and

Joe Martini in particular for hard work and dedication to their projects. I wish them the best in their future endeavors. In the same vein I'd like to thank Jenni Soliz, Emily Barton, Stephen Morin and Alex Barksdale for enriching my research experience. I'd like to thank Hugo Celio for his friendship, optimism and help with various aspects of data acquisition and analysis.

I'm indebted to various members of the Department of Chemistry and Biochemistry for their help and assistance. Members of the Vanden Bout, Bard, Crooks, Brodbelt, Shear, Holcombe, Jones, Krische, Iverson and Cowley groups were very gracious in sharing their equipment and knowledge. I'd also like to thank members of the Manthiram group at the Department of Mechanical Engineering and the Chandler group at Trinity University for help with experiments.

Finally I'm indebted to my friends and family for their unconditional love and support. I couldn't have done this without them.

Synthesis and Characterization of Carbon Nanotube Supported Nanoparticles for Catalysis

Publication No._____________

Ganesh Vijayaraghavan, PhD
The University of Texas at Austin, 2007

Supervisor: Keith J. Stevenson

This dissertation describes the synthesis and characterization of nitrogen doped carbon nanotube (NCNT) supported nanoparticles for catalysis, specifically, the cathodic oxygen reduction reaction (ORR) in fuel cells. Strategies for synthesis of mono- and bimetallic nanoparticle catalysts through dendrimer based templating techniques and with the aid of metal organic chemical vapor deposition (MOCVD) precursors and efficient assembly protocols of the catalysts with the NCNTs are discussed in detail. Physicochemical properties of the NCNTs and NCNT supported catalysts were characterized using a host of tools including scanning electron microscopy, transmission electron microscopy, Raman spectroscopy, x-ray photoelectron spectroscopy (XPS), thermo gravimetric analysis, BET surface area and pore size analysis and electrochemical techniques including cyclic voltammetry, chronocoulometry, chronoamperometry and rotating disk electrode voltammetry. Chapter 1 serves as a general introduction and provides a brief overview of challenges associated with the synthesis, characterization and utilization of graphitic carbons and graphitic carbon supported catalysts in heterogeneous catalysis. Chapter 2 provides an overview of the synthesis and characterization of systematically doped iron and nickel catalyzed NCNTs in an effort to understand the effect of nitrogen doping on ORR. Chapter 3 describes the use of NCNTs as supports for dendrimer templated nanoparticle catalysts for ORR. A facile synthetic strategy for the immersion based loading of catalysts onto NCNTs by spontaneous adsorption to achieve specific catalyst loadings is explored. Chapter 4 details the loading of monodisperse Pt, Pd and PtPd catalysts on the as synthesized NCNTs using MOCVD precursors. The MOCVD route offers promise for direct dispersion and activation of ORR catalysts on NCNT supports and eliminates a host of problems associated with traditional solvent based catalyst preparation schemes. Chapter 5 details future directions on a few topics of interest including efficient electrodeposition strategies for preparing NCNT supported catalysts, studies on PtCu catalysts for ORR and finally prospects of using NCNT supported catalysts in fuel cell applications.

Table of Contents

List of Tables xii

List of Figures xiii

List of Schemes xviii

Chapter 1. Nitrogen Doped Nanocarbon Supported Catalysts for Heterogeneous Catalysis

- 1.1 Introduction 1
- 1.2 References 9

Chapter 2. Synthesis and Characterization of Nitrogen Doped Carbon Nanotubes for Oxygen Reduction

- 2.1 Introduction 12
- 2.2 Experimental 16
  - 2.2.1 Fe Catalyzed CNT Synthesis 16
  - 2.2.2 Ni Catalyzed CNT Synthesis 18
  - 2.2.3 Electron Microscopy 18
  - 2.2.4 BET Surface Area and Pore Size Analysis 19
  - 2.2.5 Raman Spectroscopy 19
  - 2.2.6 X-Ray Photoelectron Spectroscopy 19
  - 2.2.7 Thermo Gravimetric Analysis 20
  - 2.2.8 Electrochemical Analysis 20
- 2.3 Results and Discussion 22
  - 2.3.1 CNT Growth on Substrates 22
  - 2.3.2 TEM Observations of the Fe Catalyst and CNT Crystallinity 24
  - 2.3.3 Surface Area and Porosity of CNTs 26
  - 2.3.4 Raman Analysis 29
    - 2.3.4.1 Raman Analysis at Fe Catalyzed CNTs 29
    - 2.3.4.2 Raman Analysis at Ni Catalyzed CNTs 29
  - 2.3.5 XPS Analysis 31
    - 2.3.5.1 XPS Analysis at Fe Catalyzed CNTs 31
    - 2.3.5.2 XPS Analysis at Ni Catalyzed CNTs 31
  - 2.3.6 Effect of Increasing Fe Content in CNTs on ORR 37
  - 2.3.7 Electrochemical Analysis at CNTs 39
    - 2.3.7.1 ORR at Fe Catalyzed CNTs 39
    - 2.3.7.2 ORR at Ni Catalyzed CNTs 43

2.3.7.3 Effect of Pyridinic Nitrogen on ORR 45
2.4 Conclusions 51
2.5 References 52

Chapter 3. Synergistic Assembly of Dendrimer Templated Catalysts and Nitrogen Doped Carbon Nanotube electrodes for Oxygen Reduction 55
3.1 Introduction 55
3.2 Experimental 60
3.2.1 Synthesis of Monometallic Dendrimer Encapsulated NPs 60
3.2.2 Synthesis of Bimetallic Dendrimer Encapsulated NPs 61
3.2.3 Synthesis of Undoped CNTs and NCNTs 62
3.2.4 Adsorption of Pt-DENs on CNTs and NCNTs 62
3.2.5 Electron Microscopy 64
3.2.6 Thermo Gravimetric Analysis 64
3.2.7 Electrochemistry at CNT/ DEN Composites 64
3.3 Results and Discussion 66
3.3.1 Structure and Composition of DENs 66
3.3.2 Analysis of Pt-DEN Adsorption at CNTs and NCNTs 66
3.3.3 TEM Analysis of DENs Adsorbed on NCNTs 76
3.3.4 Comparison of Adsorption Characteristics of dendrimers 78
3.3.5 TGA Analysis of Pt-DEN Loading on NCNTs 81
3.3.6 Electrochemical Analysis of CNT/ DEN Composites 83
3.3.6.1 CV Analysis at CNT/ Pt-DEN Composites 83
3.3.6.2 Rotating Disk Electrode Studies 84
3.4 Conclusions 89
3.5 References 91

Chapter 4. Metal Organic Chemical Vapor Deposition of Nanocarbon Supported Mono- and Bimetallic Catalysts for Oxygen reduction 94
4.1 Introduction 94
4.2 Experimental 99
4.2.1 Synthesis of Undoped CNTs and NCNTs 99
4.2.2 CVD of Mono- and Bimetallic Nanoparticles on CNTs 99
4.2.3 Electron Microscopy 100
4.2.4 Raman Characterization 100
4.2.5 XPS Characterization 101
4.2.6 TGA 101
4.2.7 Electrochemical Analysis 101
4.3 Results and Discussion 103
4.3.1 Morphology of Catalysts Synthesized by MOCVD 103

        4.3.2 Raman Analysis 107
        4.3.3 XPS Analysis 107
        4.3.4 TGA Analysis 110
        4.3.5 Electrochemical Analysis 113
            4.3.5.1 Cyclic Voltammetry 113
            4.3.5.2 ESA Analysis by CO Stripping 115
            4.3.5.3 Chronoamperometric Studies 117
            4.3.5.4 RDE Studies 119
            4.3.5.5 Stability of PtPd Catalysts 121
    4.4 Conclusions 126
    4.5 References 127

Chapter 5. Future Directions 130
    5.1 Introduction 130
    5.2 Results and Discussion 132
        5.2.1 Electrodeposition of Nanoparticle Catalysts on NCNTs 132
        5.2.2 Synthesis and Characterization of NCNT Supported PtCu 139
            5.2.2.1 Studies on Dealloying at Au Thin Films 140
            5.2.2.2 Effects of Electrochemical Dealloying at NCNT/PtCu 143
            5.2.2.3 Development of New Characterization Strategies 145
        5.2.3 CNT Supported Catalysts in Fuel Cells 146
    5.4 Conclusions 148
    5.4 References 148
Vita.....150

List of Tables.

Table 2.1 Comparison of parameters derived from Raman, XPS, cyclic voltammetry, surface area analysis and TGA analysis for Fe and Ni catalyzed NCNTs 50

Table 3.1 Comparison of Pt-DEN adsorption parameters, BET surface area, electroactive surface area and peak potential for ORR at undoped CNT/ Pt-DEN, and NCNT/ Pt-DEN composites for 4 % NCNTs and 7.5 % NCNTs 86

Table 4.1 Comparison of BET surface areas and edge plane content for pristine nanocarbons calculated from Raman data for undoped CNTs, 4 % NCNTs and 6.5 % NCNTs. Also compared are catalyst loadings on the nanocarbons and ESAs obtained from integrated charge associated with the oxidation of CO and hydrogen adsorption/ desorption for supported PtPd catalysts 118

List of Figures.

Figure 1.1 Representation of disparity in classic and new carbons. Plot shows comparison of surface areas between the two classes of carbons 2

Figure 2.1 Schematic of the apparatus used to synthesize undoped and nitrogen doped CNTs 17

Figure 2.2 Representative SEM image of CNTs grown directly on a Ni mesh current collector. Image shows that CNTs retain their alignment even after acid dissolution of the Ni 23

Figure 2.3 Representative TEM images of residual Fe catalyst particles encased within the graphitic sheets of CNTs. a) Encapsulated Fe in undoped CNTs. b) Fe encapsulated within 5 % NCNTs 25

Figure 2.4 Plot of differential surface area corresponding to pore sizes at undoped CNTs and NCNTs measured using nitrogen 28

Figure 2.5 Raman spectra showing the D and G bands on nitrogen doped Ni catalyzed NCNTs 30

Figure 2.6 Plot of I_D / I_G vs. the pyridinic concentration at Ni based NCNTs. Also shown is the length of crystallinity (L_a) correlating degree of structural disorder to the pyridinic fraction of surface nitrogen 32

Figure 2.7 XPS spectra showing the nitrogen region in nitrogen doped Ni catalyzed NCNTs 34

Figure 2.8 Quantitative comparison of the different nitrogen fractions in nitrogen doped Ni catalyzed NCNTs based on XPS spectra 36

Figure 2.9 Oxygen reduction at 4 % NCNTs with varying concentrations of Fe added to the electrolyte solution 38

Figure 2.10 Plot showing correlation between peak potential for ORR activity corresponding to mass of iron precursor used to synthesize nitrogen doped CNTs 40

Figure 2.11 ORR activity for undoped CNTs and NCNTs in oxygen saturated 0.1 M H_2SO_4. $\nu = 20$ mVs^{-1} 42

Figure 2.12 Comparison of cyclic voltammograms for ORR at undoped CNTs and NCNTs synthesized using Fe and Ni precursors in oxygen saturated 0.1 M H_2SO_4. $\nu = 20$ mVs^{-1} 44

Figure 2.13 Plot showing correlation between peak potential for ORR activity corresponding to edge plane content calculated from Raman spectra at Fe and Ni based NCNTs. ORR activity was measured in oxygen saturated 0.1 M H_2SO_4 46

Figure 2.14 Plot showing correlation between peak potential for ORR activity corresponding to the pyridinic nitrogen fraction at Fe and Ni based NCNTs. ORR activity was measured in oxygen saturated 0.1 M H_2SO_4 47

Figure 2.15 Plot showing correlation between peak potential for ORR activity corresponding to the total nitrogen content at Fe and Ni based NCNTs. ORR activity was measured in oxygen saturated 0.1 M H_2SO_4 48

Figure 3.1 Representative TEM image of Pt –DENs. The histogram depicts a typical particle size distribution for the Pt-DENs 67

Figure 3.2 Representative TEM image of Pd –DENs. The histogram depicts a typical particle size distribution for the Pd-DENs 68

Figure 3.3 Representative TEM image of PdAu –DENs. The histogram depicts a typical particle size distribution for the PdAu-DENs 69

Figure 3.4 Representative energy dispersive spectrum for PdAu- DENs 70

Figure 3.5 UV-Vis spectra showing cumulative adsorption measurements observed over 24 hours for the adsorption of Pt-DEN nanoparticles on 4 % NCNTs 71

Figure 3.6 Picture representing the Pt-DEN adsorption process on NCNTs. A) 20 μM Pt-DENs. B) Pt-DENs with NCNTs suspended in solution. C) NCNT/ Pt-DEN suspension after 24 hrs showing all DENs having been adsorbed onto the NCNTs rendering the solution colorless 73

Figure 3.7 Adsorption isotherms for G_4-NH_2 Pt-DEN adsorption on undoped CNT and NCNT supports 74

Figure 3.8 TEM image of G4-NH_2 Pt-DENs adsorbed on 4 % NCNT supports (Scale bar is 20nm). The inset shows high resolution structure of Pt nanoparticles (Scale bar is 5nm) 77

Figure 3.9 TEM images of dendrimer encapsulated nanoparticles adsorbed on the NCNT surface. a) Pd DENs adsorbed on 4 % NCNTs. b) PdAu DENs adsorbed on 4 % NCNTs 79

Figure 3.10 Representative TEM images comparing the adsorption of $-NH_2$ terminated and –OH terminated Pt DENs on 4 % NCNTs. a) G4-NH_2 Pt DENs adsorbed on 4 % NCNTs. b) G4-OH Pt DENs adsorbed on 4 % NCNTs 80

Figure 3.11 Representative TGA heating curves for blank NCNTs and Pt-DENs adsorbed on 7.5 % NCNTs. Mass loading of Pt on NCNTs is calculated by subtracting final wt. % of NCNT/ Pt-DEN from final wt. % at blank NCNT 82

Figure 3.12 Cyclic voltammograms for ORR at control undoped CNTs and NCNTs synthesized using Fe and Ni precursors compared to NCNT/ Pt-DEN composites in oxygen saturated 0.1 M H_2SO_4. $\nu = 20$ mVs^{-1} 85

Figure 3.13 Polarization curves for the ORR on G_4-NH_2 Pt-DEN/CNT and NCNT composites supported on a glassy carbon electrode immersed in an O_2 saturated 0.1M H_2SO_4 solution. In all cases the Pt loading is 18±1 μg. Also shown are polarization curves for CNT and NCNT supports. Rotation rate =1600 rpm, scan rate =20 mV s^{-1} 87

Figure 4.1 TEM images of a) Pt and c) Pd catalysts on NCNT supports. Corresponding particle size histograms for b) Platinum and d) Palladium catalysts 105

Figure 4.2 TEM image of a) PtPd particles on 6.5 % NCNT supports. Inset shows high resolution image of a PtPd bimetallic catalyst particle. b) Corresponding particle size histogram for PtPd catalysts. c)

Representative energy dispersive spectrum of a single PtPd nanoparticles 106

Figure 4.3 Raman spectra of PtPd bimetallic catalysts on NCNT supports with varying surface concentrations of nitrogen 108

Figure 4.4 XPS spectra of PtPd supported on 6.5 % NCNTs. a) Survey spectrum of PtPd showing Pt and Pd regions. b) High resolution XPS spectrum of Pt and c) Pd catalysts supported on 6.5 % NCNTs 109

Figure 4.5 TGA heating curves for PtPd catalysts on various CNT supports 111

Figure 4.6 Effect of edge plane content at NCNTs on PtPd loading as determined by TGA 112

Figure 4.7 Representative cyclic voltammogram for PtPd catalysts supported on 6.5 % NCNTs in O_2 saturated 0.1M H_2SO_4 114

Figure 4.8 CO stripping voltammogram on PtPd catalysts supported on 6.5 % NCNTs. CO was dosed into solution for 20 min followed by 30 min of Ar purge to remove CO in bulk 116

Figure 4.9 CO stripping transients on PtPd catalysts supported on 6.5 % NCNTs. CO was dosed into solution for 20 min followed by 30 min of Ar purge to remove CO in bulk. The working electrode was held at 0.11V during CO dosing and raised to stripping potentials 120

Figure 4.10 Polarization curves for ORR on PtPd catalysts supported on 6.5 % NCNTs in O_2 saturated 0.1 M $HClO_4$. The RDE was rotated between 250 – 3000 rpm in increments of 250 rpm. Scan rates were set at 20 mV /s 122

Figure 4.11 Polarization curves for ORR on PtPd catalysts supported on 6.5 % NCNTs in O_2 saturated 0.1 M H_2SO_4 showing the effects of adsorbed bisulfate. The RDE was rotated between 250 – 3000 rpm in increments of 250 rpm. Scan rates were 20 mV /s 123

Figure 4.12 Extended cycling of PtPd catalysts supported on 6.5 % NCNTs in O_2 saturated 0.1 M H_2SO_4 124

Figure 5.1 Chronocoulometric profile of the electrodeposition of Au nanoparticles from 0.2 mM $HAuCl_4$ solutions on NCNTs 134

Figure 5.2 Representative TEM images of nanoparticle catalysts deposited on 4 % NCNTs. a) Au nanoparticles. b) PtAu nanoparticles 135

Figure 5.3 High resolution TEM image of PtAu nanoparticles electrodeposited on NCNTs 137

Figure 5.4 Cyclic voltammograms for oxygen reduction at PtAu catalysts deposited on NCNTs. CV's were run in O_2 saturated 1 M KNO_3 138

Figure 5.5 Scanning electron microscope image of Au film subjected to 30 alloy/ dealloy cycles in a $ZnCl_2$ / benzyl alcohol solution 141

Figure 5.6 Cyclic voltammograms of an Au film in 0.5 M H_2SO_4 before and after alloying/ dealloying cycles in a $ZnCl_2$ / benzyl alcohol solution. Integration of the cathodic AuO peak showed a 17.1 % increase in the electrochemical surface area on the dealloyed Au film 142

Figure 5.7 Electrochemical dissolution of Cu from PtAu bimetallic catalysts synthesized using dendrimer templates. The PtCu/ DEN catalysts were supported on 6.5 % NCNTs. Dissolution studies were carried out in 0.1 M $HClO_4$ 144

Figure 5.8 Half cell trial of CNT supported Pt DEN catalysts for ORR in 1 M H_2SO_4 147

List of Schemes.

Scheme 3.1 Preparation of amine terminated PAMAM dendrimer encapsulated Pt nanoparticles (G_4-NH_2 Pt-DENs) and adsorption onto carbon nanotube (CNT) supports 58

Scheme 3.2 Representation of synergistic ORR activity at NCNT/ Pt-DEN composites 90

CHAPTER 1

Nitrogen Doped Nanocarbon Supported Catalysts for Heterogeneous Catalysis

1.1 INTRODUCTION

The use of carbon in a chemical process dates back as far as 3750 BC in the Bronze Age. Early Egyptians and Sumerians were known to have used charcoal to reduce copper, tin and zinc ores for producing bronze. Since then carbons have evolved for use in a multitude of processes. Traditional carbons[1,2] or 'classic carbons' such as soot, charcoal and diamond have been mostly replaced with new and novel carbon materials or 'new carbons'.[3] Since the 1960's a variety of synthetic strategies have been employed to produce carbons that have favorable structure, texture and composition that allow for these new carbons to perform significantly better than classic carbons.[4] Early examples of these new carbons included carbon fibers, porous carbons and pyrolitic graphite electrodes.[3] Of these new carbons, graphitic carbons have shown promise for usage in energy storage and conversion processes due to their high electronic conductivity, resistance to corrosion and physical stability.[5,6,7]

Diverse synthetic protocols have been utilized in the preparation of graphitic carbons. Fullerenes,[8] are one form of graphitic carbons that were discovered in 1985 and have been synthesized by the evaporation of carbon using an electric arc between graphite electrodes in an inert atmosphere. Carbon nanotubes (CNTs) discovered by Ijima[9] in 1991 are another form of graphitic

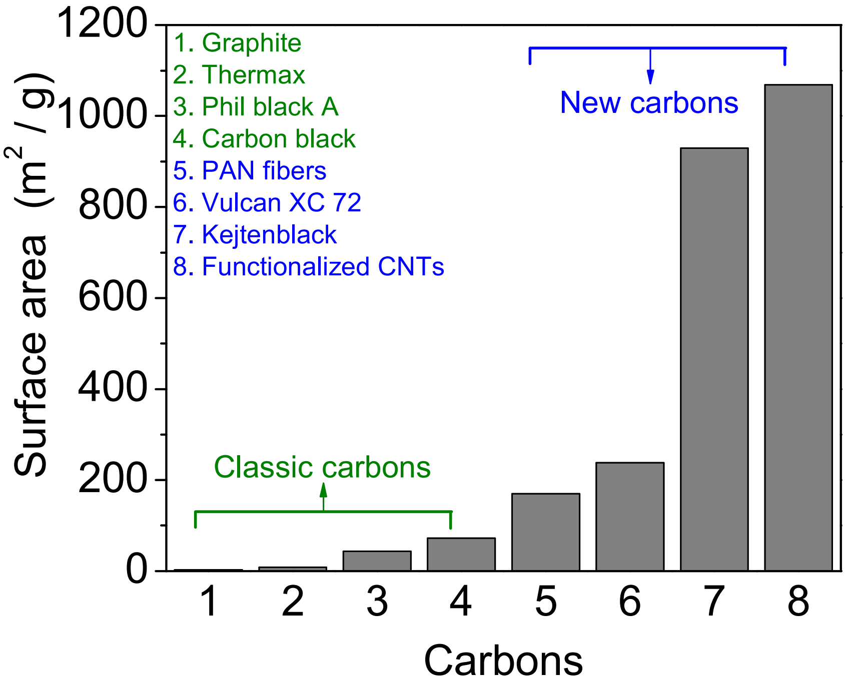

Figure 1.1 Representation of disparity in classic and new carbons. Plot shows comparison of surface areas between the two classes of carbons.

carbons that have been synthesized by various routes. CNTs have been produced using templated techniques, some of which involve the deposition of carbon from propylene gas at 800 ^{0}C on the inner walls of nanoscale channels in an aluminum oxide film.[10,11] The CNTs were then recovered by dissolution of the film in HF. Other techniques include CNTs produced using a polymer blend process,[12,13] CNTs produced with the help of a steep thermal gradient in alcohols,[14] CNTs produced by the decomposition of SiC in a single crystal wafer[15] and the more popular laser ablation technique.[16,17]

The popularity of CNTs stems from favorable properties such as good electronic conductivity, surface area, preferred pore structure, ability to be synthesized in ordered arrays,[18] ease of assembly on a secondary substrate through Van der Waal's interactions,[19,20] facility for directed growth[21] – typically brought upon by application of an electric field and scalability of the patterned growth.[22]

While these as-synthesized CNTs perform well in their primary purpose as electron conductors in chemical and electrochemical processes, it would be of tremendous advantage if this class of graphitic carbons were modified to be active in these chemical and electrochemical reactions themselves. Efforts towards this end have involved heteroatom doping – most notably nitrogen doping on graphitic carbons. A number of groups such as Thrower et al,[23,24] Wang et al[25], Boehm et al,[26,27] Gooding et al,[28,29] Compton et al,[30,31] Cai et al[32] and Dodelet et al[25,33] have studied the effects of nitrogen doping in graphitic carbons especially on the oxygen reduction reaction (ORR). ORR is a technologically important reaction that takes place in the cathodic side of a fuel cell.

A number of synthetic strategies have been employed in the nitrogenation of graphitic carbons. The most popular method being the introduction of the as-prepared carbon into an atmosphere of NH_3 or HCN at high temperatures.[25] The resulting carbon was found to be enriched in nitrogen and had a significantly higher activity for electrochemical reduction of oxygen. While it has been of general consensus that nitrogen doping increases the activity at these carbons, there has been ambiguity as to what physicochemical factor or factors effect this difference in activity. Most of the ambiguity stems from poor reproducibility[33] and stability problems associated with the post- synthetic modification step at these carbons. To this end, effort in the Stevenson research lab has been concentrated on developing facile synthetic protocols[34,35,36] that enable synthesis of systematically doped graphitic nanocarbons in order to elucidate individual physicochemical properties and their contribution to ORR activity.

Chemical vapor deposition (CVD) is employed for the controlled synthesis of nitrogen doped carbon nanotubes (NCNTs) at the Stevenson research lab. The use of synthetic precursors in CVD synthesis allows for systematic manipulation of structure, composition, surface area and the degree of structural disorder at NCNTs. This systematic manipulation allows for distinctive delineation of the effects brought upon by nitrogen doping on the electrochemical properties of the NCNTs. Accordingly, Maldonado et al have published a series of papers[34,35,36] elucidating the influence of systematic nitrogen doping at NCNTs on several electrochemical processes including ORR.

While a systematic increase in nitrogen doping at graphitic carbons increases the activity for ORR at these nanocarbons, their activities are lower than what is seen at metals known for exhibiting high ORR activity. Efforts undertaken to improve on this particular aspect have involved using these carbons as supports for active metal nanoparticle catalysts to be used in heterogeneous catalysis.

Conventional strategies employed for loading metal catalysts on carbons typically involve inducing surface functionalities such as carbonyl, carboxylate, ester-like oxygen or alcohol on the carbon to facilitate anchoring of catalysts on the support. This is done using aggressive protocols that involve the use of strong acids[37] like HNO_3, H_2SO_4, HCN or strong oxidizing agents[38] like H_2O_2, $KMnO_4$. These protocols are often not reproducible and degrade the preferred structural and compositional properties of both the carbon support and active metal catalyst.

The ability to manipulate *in-situ*, the structure, composition, surface area and the density of edge plane sites on NCNTs provides a significant advantage over traditional carbons for use as catalyst supports because there is no further need to modify the surface to facilitate catalyst loading. This offers tremendous advantages in using NCNTs as catalyst supports while circumventing the time consuming and often structurally degrading pre- synthesis steps that are used in catalyst loading protocols like microemulsion,[39] impregnation,[40] co-precipitation,[41] sonochemical[42] and fluidized bed CVD processes.[43] NCNTs as catalyst supports also allow for uniform catalyst dispersion and utilization stemming from control of their surface properties such as the density of edge plane sites and porosity.

Challenges in defining physicochemical properties of nitrogenated graphitic carbons (esp. NCNTs) that contribute to oxygen reduction and the advantages in using these properties efficiently and synergistically with active metal catalysts for ORR are discussed in this dissertation.

This dissertation is organized into five chapters. Chapter 1 serves as a general introduction and provides a brief overview of challenges associated with the synthesis, characterization and utilization of graphitic carbons and graphitic carbon supported catalysts in heterogeneous catalysis.

Chapter 2 provides an overview of the synthesis and characterization of systematically doped iron and nickel catalyzed NCNTs in an effort to understand the effects of nitrogen doping on ORR. The influence of nitrogen doping on the physicochemical and electrochemical properties at these NCNTs is characterized using transmission electron microscopy (TEM), scanning electron microscopy (SEM), Raman spectroscopy, x-ray photoelectron spectroscopy (XPS), thermo gravimetric analysis (TGA), BET surface area and pore size analyses and electrochemical characterization including cyclic voltammetry (CV) and rotating disk electrode voltammetry (RDE). Raman analysis in conjunction with XPS and electrochemical analysis suggests that the presence of increased edge plane sites at NCNTs along with increased surface concentrations of pyridinic nitrogen are influencing factors for remarkable ORR activity at NCNTs. BET surface area and pore size analyses indicate that the porosity at NCNTs does not correlate to ORR activity. ORR activity studies at Ni based NCNTs suggest that an Fe based active center does not provide for a complete picture of the ORR mechanism.

Chapter 3 describes the use of CNTs as supports for dendrimer templated catalysts (DENs) for ORR. A facile synthetic strategy for the immersion based loading of catalysts onto a carbon support by spontaneous adsorption to achieve specific catalyst loadings is explored. The resultant CNT-DEN composites were assembled without necessitation of time consuming and irreproducible pre- and post- synthetic processing steps. The advantage of this synthetic strategy is that the compositional and structural properties of both the carbon support and the DEN catalyst can be reproducibly prepared and synergistically tuned to directly assemble carbon-supported catalyst composites via adsorption from aqueous solution. The as loaded Pt-DENs were found to be uniformly dispersed throughout the CNTs and CNT/ Pt-DEN composites were found to be active for ORR. A synergistic activity is envisioned where the NCNT support is reactive and serves to reduce the peroxide formed as a byproduct during oxygen reduction at the metal catalyst.

Chapter 4 details the loading of monodisperse Pt, Pd and PtPd catalysts on as synthesized NCNTs using metal organic chemical vapor deposition (MOCVD) precursors. The MOCVD route offers promise for the direct dispersion and activation of mono- and multimetallic ORR catalysts on NCNT supports and eliminates the current inevitable problems involving loading, sintering and activation steps associated with traditional solvent based catalyst preparation schemes. The tunability of the amount of edge plane content on the NCNT support offers distinct advantages with regard to preferential catalyst loading and decomposition of peroxide specific to ORR. The MOCVD process is expected to serve as a model system for rapid and direct assembly of carbon supports and varied catalyst compositions that provide promising activity for oxygen reduction.

Chapter 5 details future directions in studies on a few topics of interest involving efficient synthetic strategies for NCNT/ nanoparticle catalysts and their application towards ORR. In this regard, electrodeposition aspects of loading mono- and bimetallic catalysts directly on as synthesized NCNT electrodes is reported. Facile characterization protocols that allow for TEM observations of the as synthesized NCNT/ catalyst composite and the composite after being subject to ORR are also discussed. These characterization protocols show marked improvements to existing strategies and are expected to play a vital role in the design of effective ORR catalysts. Other future directions discussed include studies on PtCu catalysts for ORR. The selective dissolution of Cu from a bimetallic PtCu catalyst presents intriguing possibilities as to a more active catalyst surface for ORR. The electrochemical dealloying of Cu is speculated to improve the electrochemical surface area and enhance mass transport. Characterization of such interfaces will help design stable and active catalyst combinations for ORR.

1.2 REFERENCES

1. Inagaki, M. Old but new materials: carbons. In *Carbons- control of structure and functions*; Elsevier, 2000; p. 1 – 29.

2. Walker Jr. P. L. *Carbon*, **1990**, *28*, 261.

3. Inagaki, M.; Radovic, L. R. *Carbon*, **2002**, *40*, 2263.

4. Inagaki, M. In *New carbons – control of structure and functions*; Inagaki, M., Ed.; Elsevier, 2000; p. 82-123.

5. Sato, K.; Noguchi, M.; Demachi, A.; Oki, N.; Endo, M. *Science*, **1994**, *264*, 556.

6. Endo, M.; Maeda, T.; Takeda, T., Kim, Y. J.; Koshiba, K.; Hara, H.; Dresselhaus, M. S. *J. Electrochem. Soc.* **2001**, *148*, A910.

7. Endo, M.; Hayashi, T.; Hing, S. H.; Enoki, T.; Dresselhaus, M. S. *J. Appl. Phys.* **2001**, *90*, 5670.

8. Kroto, H. W.; Heath, J. R.; O' Brien, S. C.; Curl, R. F.; Smalley, R. E. *Nature*, **1985**, *318*, 162.

9. Ijima, S. *Nature*, **1991**, *354*, 56.

10. Kyotani, T.; Tsai, L.; Tomita, A. *Chem. Mater.* **1995**, *7*, 1427.

11. Kyotani, T.; Tsai, L.; Tomita, A. *Chem. Mater*. **1996**, *8*, 2109.

12. Oya, A.; Kasahara, N. *Carbon*, **2000**, *38*, 1141.

13. Hulicova, D.; Sato, F.; Okabe, K.; Koishi, M.; Oya, A. *Carbon*, **2001**, *39*, 1438.

14. Zhang, Y.; Nishitani- Gamo, M.; Nagakawa, K.; Ando, T. *J. Mater. Res*. **2002**, *17*, 2457.

15. Kusunoki, M.; Rokkaku, M.; Suzuki, T. *Appl. Phys. Lett.* **1997**, *18*, 2620.

16. Kocabas, C.; Meitl, M. A.; Gaur, A.; Shim, M.; Rogers, J. A. *Nano Lett*. **2004**, *4*, 2421.

17. Krungleviciute, V.; Heroux, V.; Migone, A. D.; Kingston, C. T.; Simard, B. *J. Phys. Chem. B* **2005**, *109*, 9317.

18. Fan, S.; Chapline, M.; Franklin, N.; Tombler, T.; Cassell, A.; Dai, H. *Science*, **1999**, *283*, 512.

19. Cassell, A.; Franklin, N.; Tombler, T.; Chan, E.; Han, J.; Dai, H. *J. Am. Chem. Soc.* **1999**, *121*, 7975.

20. Franklin, N.; Dai, H. *Adv. Mater*. **2000**, *12*, 890.

21. Zhang, Y.; Chan, A.; Cao, J.; Wang, Q.; Kim, W.; Dai, H. *Appl. Phys. Lett*. **2001**, *79*, 3155.

22. Franklin, N.; Li, Y.; Chen, R. J.; Javey, A.; Dai, H. *Appl. Phys. Lett*. **2001**, *79*, 4571.

23. Strelko, V. V.; Kuts, V. S.; Thrower, P. A. *Carbon*, **2000**, *38*, 1499.

24. Thrower, P. A.; Radovic, L. R.; *Carbon*, **2000**, *39*, 1.

25. Wang, H.; Cote, R.; Faubert, G.; Guay, D.; Dodelet, J. P. *J. Phys. Chem. B* **1999**, *103*, 2042.

26. Boehm, H. P.; Mair, G.; Stoehr, T.; DeRincon, A. R.; Tereczki, B. *Fuel* **1984**, *63*, 1061.

27. Stohr, B.; Boehm, H. P.; Schlogl, R. *Carbon* **1991**, *29*, 707.

28. Gooding, J. *J. Electrochimica Acta* **2005**, *50*, 3049.

29. Chou, A.; Bocking, T.; Singh, N. K.; Gooding, J. *J. Chem. Commun*. **2005**, *7*, 842.

30. Banks, C. E.; Moore, R. R.; Davies, T. J.; Compton, R. G. *Chem. Commun*. **2004**, *16*, 1804.

31. Salimi, A.; Banks, C. E.; Compton, R. G. *Analyst*, **2004**, *129*, 225.

32. Jaouen, F.; Lefevre, M.; Dodelet, J. P.; Cai, M. *J. Phys. Chem. B* **2006**, *110*, 5553.

33. Jouen, F.; Charreteur, F.; Dodelet, J. P. *J. Electrochem. Soc*. **2006**, *153*, A689.

34. Maldonado, S.; Stevenson, K. J. *J. Phys. Chem. B* **2004**, *108*, 11375.

35. Maldonado, S.; Stevenson, K. J. *J. Phys. Chem. B* **2005**, *109*, 4707.

36. Maldonado, S.; Morin, S.; Stevenson, K. J. *Carbon* **2006**, *44*, 1429.

37. Wang, J.; Musameh, M.; Lin, Y. *J. Am. Chem. Soc*. **2003**, *125*, 2408.

38. Tian, Z. Q.; Jiang, S. P.; Liang, Y. M.; Shen, P. K. *J. Phys. Chem. B.* **2006**, *110*, 5343.

39. Yoon, B.; Wai, C. M. *J. Am. Chem. Soc.* **2005**, *127*, 17174.

40. Gaur, V.; Sharma, A.; Verma, N. *Carbon* **2005**, *42*, 3041.

41. Li, X.; Hsing, I. -M. *Electrochim. Acta* **2006**, *51*, 5250.

42. Xing, Y. *J. Phys. Chem. B* **2004**, *108*, 19255.

43. Serp, P.; Hierso, J. C.; Feurer, R.; Kihn, Y.; Kalck, P.; Faria, J. L.; Aksoylu, A. E.; Pacheco, A. M.; Figueiredo, J. L. *Carbon* **1999**, *37*, 527.

CHAPTER 2

Synthesis and Characterization of Nitrogen Doped Carbon Nanotubes for Oxygen Reduction

2.1 INTRODUCTION

Graphitic carbons have been used as supports for a variety of processes and especially in heterogeneous catalysis.[1-4] The interest in using these carbons stems from their good electrical conductivity,[5,6] high surface area[7] and good mechanical and chemical stability.[8] While these carbons perform well in their primary purpose as electron conductors for chemical and electrochemical processes, it would be of tremendous advantage if these carbons were tuned to take part in these chemical and electrochemical reactions themselves. This scenario would make more efficient use of the surface area of these supports in devices like fuel cells and batteries.

One technologically important reaction where graphitic carbons are used as catalyst supports is the oxygen reduction reaction (ORR) that takes place in the cathodic side of a fuel cell.[9-11] Efforts to enhance the oxygen reduction activity at these carbons have been afoot since the late 60's[12] have increased substantially since the early 80's partly due to the re-emergence of fuel cells as promising 'green' power sources.[13] Heteroatom doping of these graphitic carbons especially with nitrogen has been known to significantly enhance their chemical reactivity,[3,4] although the exact mechanism is not well understood. While a number of protocols have been used to prepare nitrogen doped carbons,[14,15] the more popular methods call for heat treatment of pre-synthesized carbons in an atmosphere of NH_3 or HCN[16] followed by exposure to an Ar atmosphere at higher temperatures. One of the earlier reports by Wang et al[17] details the oxidation of Vulcan carbon using a strong acid and successive heat treatments under NH_3 at 600 °C and Ar at 900 °C. The resulting carbon was found to exhibit enhanced activity for ORR compared to the undoped carbon as shown by a positive shift of ~200 mV in the oxygen reduction peak potential.

The enhancement in activity for nitrogenated graphitic carbons has been attributed to the changes in the electronic structure of the graphene. The Gooding[18,19] and Compton groups[20,21] have attributed the enhanced electrocatalytic activity to the inducement of surface structural disorder characterized by an increase in density of edge plane sites. While it is well known that nitrogen doping on carbons produces pyridinic, pyrrolic and quaternary nitrogen functionalities,[11] reports differ on which of these surface functionalities is responsible for or contributes to ORR activity. Thrower et al[22] and Boehm et al[13] have ascribed pyridinic nitrogen functionalities on the edge plane sites to increased reactivity while other hypotheses[23] have proposed nitrogen substituted in the basal graphene as a vital factor. Literature data have also suggested that the residual iron from precursors used to synthesize these materials bound to nitrogen and carbon in a FeN_xC_y type active site[24] is responsible for ORR activity. Residual iron particles in these carbons have also been attributed to reduction of peroxide which is one of the byproducts of ORR.[25] Although these hypotheses attempt to elucidate the increased activity of nitrogen doped carbons, none of them satisfactorily explain the exact mechanism of ORR at the active centers of these carbons.

The ambiguity in assigning how a factor or a combination of factors contribute to the electrocatalytic activity at nitrogen doped graphitic carbons originates from complexities involved in the nitrogenation of pre existing carbons. To this end, a synthetic protocol to prepare and characterize a series of systematically doped carbon nanotubes was undertaken by Maldonado et al.[11] This synthetic strategy allowed for tuning the diameter, length, structure and composition of nitrogen doped carbon nanotubes (NCNTs).[10,11] These studies elucidated the changes in structure and composition of NCNTs brought upon by systematic nitrogen doping and enabled correlating these changes with the chemical reactivity and the electrochemical properties on the NCNTs as compared to regular undoped carbon nanotubes (undoped CNTs). Parallel studies by Lyon et al[26] dealt with dissolution and passivation of residual Fe encased in NCNTs and have concluded that $Fe^{II/III}$ redox activity and successive passivation of the $Fe^{II/III}$ surface oxides do not impact the onset and activity for ORR at these NCNTs.

This chapter follows up on previous experiments conducted in the Stevenson research group on systematic nitrogen doping of Fe based carbon nanotubes (NCNTs). Knowledge gained from those series of experiments was used to setup a new batch of analyses aimed to clarify the controlling aspects for ORR at NCNTs. A new variety of NCNTs synthesized using a Ni based precursor was utilized for these measurements. Efforts were also made to elucidate the importance of pyridinic nitrogen functionalities comprising total surface nitrogen concentrations on ORR activity at Ni NCNTs. Raman spectral data were used to quantify the degree of structural disorder on the NCNT surface and account for the involvement of edge plane sites in ORR.

2.2 EXPERIMENTAL

2.2.1 Fe Catalyzed CNT Synthesis

Nitrogen doped and undoped carbon nanotubes were synthesized using a floating catalyst CVD method described previously.[10,11] Briefly, an automated dual zone furnace system (Carbolite HST 12/35/200/2416CG) integrated with lab view controlled mass flow controllers (MKS 1179A) and syringe pumps (New Era Pump Systems NE-1000) was used in a setup as shown in Figure 2.1. NCNTs were prepared with pyridine (Fisher) and ferrocene (Alfa Aesar, 20mg ml $^{-1}$) precursors (xylene and ferrocene were used for undoped CNTs) loaded in an airtight syringe (Hamilton 81320) mounted on the syringe pump. The precursors were injected at a rate of 100μL min^{-1} into zone 1 of the furnace system maintained at 130°C for NCNTs (150°C for undoped CNTs) while the pyrolysis temperature in zone 2 was 800°C (700°C for the undoped CNTs). The total gas flow rate was held constant at 575 sccm for NCNTs and undoped CNTs, and a calculated feed stream (2.5 – 10 %) of anhydrous ammonia (Aldrich, 99.9%) was introduced to facilitate higher levels of nitrogen doping with Ar (99.997% Praxair) making up the reminder of the flow stream. Gas flows for the undoped CNTs constituted 500 sccm Ar and 75 sccm H_2 (99.95% Praxair). The CNTs were grown on the inside wall of a quartz tube (26mm OD, 22mm ID) that acted as the reaction chamber.

The as synthesized undoped CNTs and NCNTs were carefully collected from the inner walls of the quartz reaction chamber and stored in air tight vials

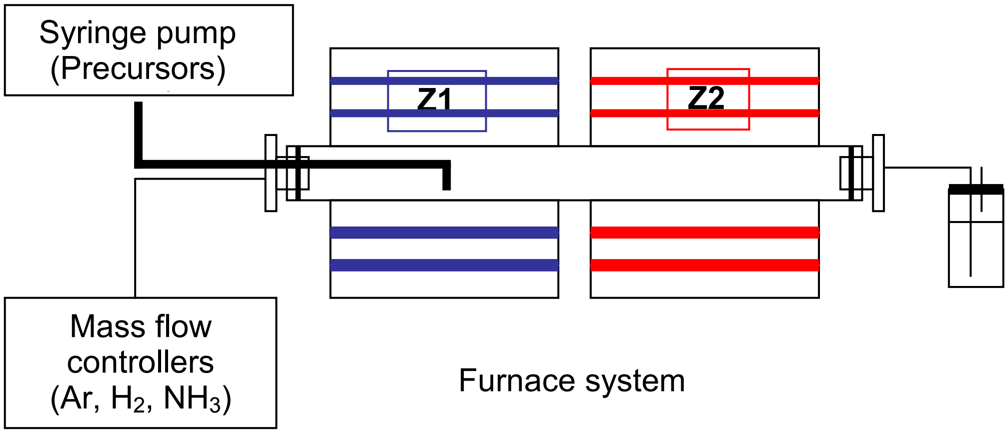

Figure 2.1 Schematic of the apparatus used to synthesize undoped and nitrogen doped CNTs.

prior to successive measurements. Electrochemical measurements were conducted on a measured mass of the CNTs drop cast[27] on a glassy carbon rotating disk electrode (RDE) as detailed in the electrochemical section below. Initial electrochemical measurements were also performed on CNTs grown directly on a nickel mesh substrate[9] that was cut to specific dimensions so as to keep the surface area of the electrode constant. The nickel mesh substrates were supported on a piece of nickel foam and were placed in the center of Z2 of the furnace system for CNT growth. After the synthesis, these substrates were stored in air tight vials prior to electrochemical analysis.

2.2.2 Ni Catalyzed CNT Synthesis

Ni catalyzed CNTs were synthesized using the same experimental setup used for Fe catalyzed CNTs. The precursor mix used for the synthesis consisted of Nickelocene (Alfa Aesar, 15 mg ml $^{-1}$) in Acetonitrile (Fisher). The precursor mix was sonicated for 5 min prior to loading in the injection syringe to facilitate uniform dispersion of the catalyst in acetonitrile. The resulting mixture was dark green in color and care was taken to reduce the presence of precipitates and atmospheric gases in the injection volume. The reaction conditions were similar to that used for the synthesis of NCNTs.

2.2.3 Electron Microscopy

Transmission electron microscope (TEM) analysis of the CNTs was performed on a JEOL 2010F instrument operating at 200 kV. The CNT sample was suspended in anhydrous ethanol and drop cast on a Cu TEM grid covered with a 3 nm thick amorphous carbon film.

Scanning electron microscope (SEM) analysis was performed using either a LEO 1530 or a Hitachi S 4000 instrument operating at 10 kV. Carbon samples collected from the interior of the quartz tube were deposited on an adhesive carbon film prior to analysis. CNTs grown on Ni substrates were introduced per se into the sample chamber.

2.2.4 BET Surface Area and Pore Size Analysis

Surface area and pore size analysis were performed on the undoped CNTs and NCNTs using a Quantachrome Autosorb-1 instrument. Sample masses of atleast 20 mg were introduced into a quartz sample holder and were degassed at 200°C for atleast 5 hrs under vacuum. Nitrogen was used as the probe gas. Surface areas were calculated from an 11 point BET analysis. Micropore distributions were obtained from density functional theory method and Monte Carlo simulation methods available within the instrument software.

2.2.5 Raman Spectroscopy

A Renishaw inVia system equipped with a 514.5 nm Ar laser at 3 mW/ cm^2 and 100X aperture was used. Spectra were scan averaged for a total time of 300 s. Bands at 1220, 1351, 1487, 1583 and 1624 cm^{-1} corresponding to I, D, D″, G, and D′ bands denoted by Cuesta et al[29] were fit using a Peak Fit 4 software package to correlation factors greater than 0.998. A linear baseline correction was used to compensate for photoluminescence background.

2.2.6 X-ray Photoelectron Spectroscopy

X-ray photoelectron spectroscopy (XPS) characterization of the samples was performed using a PHI 5700 ESCA system operating at a scan step size of 0.1 eV and an Al Kα monochromatic line and calibrated with Au $4f_{7/2}$, Ag $3d_{5/2}$ and Cu $2p_{3/2}$ signals. These spectra were scan averaged 5 times. XPS Spectra were also obtained with a Kratos Axis Ultra DLD system equipped with a dual anode (150 W Al Kα and Mg sources) with a resolution of 0.1 eV and calibrated with Au $4f_{7/2}$, Ag $3d_{5/2}$ and Cu $2p_{3/2}$ signals. These spectra were scan averaged 3 times. Atomic percentages were quantified from survey scans relative to carbon, iron and nitrogen. FITT 1.2 (Photoelectron Spectroscopy lab, Seoul National University) software with Shirley background corrections was used to analyze the spectra.

2.2.7 Thermo Gravimetric Analysis

Thermo gravimetric analysis (TGA) was performed using a Perkin Elmer 7000 TGA. CNT samples (3-5 mg) were held in platinum pans heated to 800 °C in flowing air (Praxair, 99.998%).

2.2.8 Electrochemical Analysis

Electrochemical measurements were carried out on an EG&G Instruments 263A potentiostat equipped with a Pine Instruments MSRX controller for rotating disk electrode (RDE) measurements. Data acquisition and analysis was performed on a Corrware (Scribner Associates) software package. Sample slurries prepared with 0.15 wt. % nafion in anhydrous ethanol and de-ionized water were drop cast as a film on a glassy carbon (GC) RDE (0.5 cm diameter, Pine Instruments) polished to a mirror finish and allowed to dry under a stream of Ar (Praxair 99.98%) prior to electrochemical measurements.

Cyclic voltammograms were obtained in a standard three electrode cell with a gold counter electrode and an Hg/Hg_2SO_4 reference electrode in O_2 (Praxair) saturated 0.1 M H_2SO_4 prepared with deionized water (>18 MΩ cm). All potentials were converted to NHE for comparison to literature values. Prior to oxygen reduction, the CNT film was cycled between 0.8 and -0.2V in order to make the film hydrophilic and achieve steady state voltammograms.

2.3 RESULTS AND DISCUSSION

2.3.1 CNT Growth on Substrates

Carbons used throughout this study were undoped and nitrogen-doped multi walled carbon nanotubes and hereafter referred to as undoped CNTs and NCNTs respectively. Carbon nanotubes in general are referred to as CNTs. While a few hypotheses exist as to the mechanism of the growth of CNTs aided by a metal catalyst, the base catalyzed growth mechanism is commonly accepted. The graphene layers that make up the CNTs precipitate out from the metal catalyst after super saturation of the catalyst with gaseous carbon. The graphene layers either originate out from the metal catalyst, leaving the metal particle at the base or push the metal catalyst particle out as the growth progresses. In either of these scenarios the metal particles are encapsulated within the graphene layers.

A variety of electrode supports were chosen for CNT growth to facilitate the ease and reproducibility of measurements conducted. Initial electrochemical measurements were carried out on CNTs grown directly on the surface of nickel mesh electrodes cut to exact dimensions so as to maintain a constant surface area. SEM characterization of undoped CNTs grown on nickel mesh substrates showed a remarkable degree of conformal growth and alignment along a perpendicular axis to the surface of the substrate. Earlier experiments by Maldonado et al. indicate that the as grown CNTs retain their alignment even after the removal of the growth substrate by acid dissolution as shown in Figure 2.2.

A majority of electrochemical experiments were carried out on CNTs drop cast on GC substrates. CNTs used in these experiments were carefully

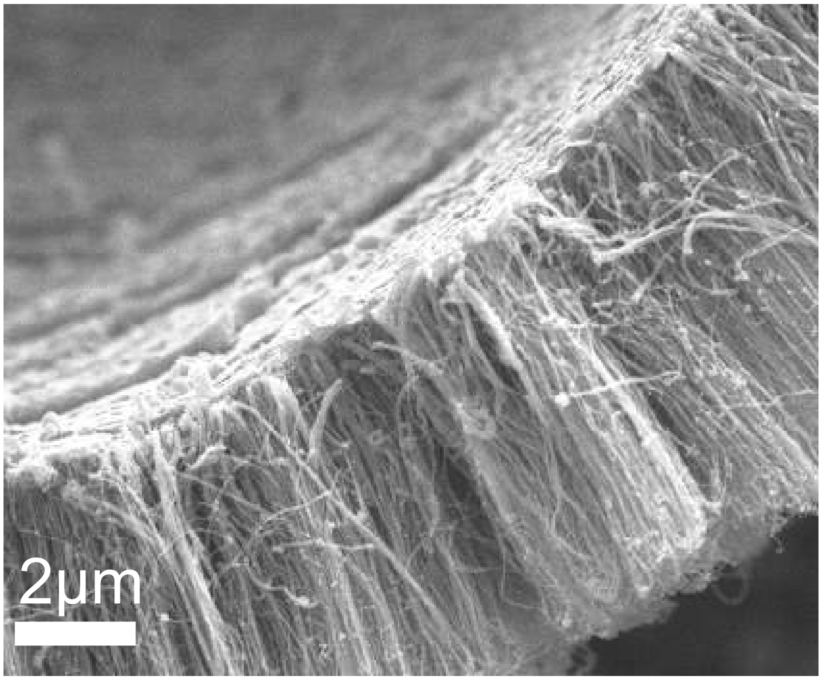

Figure 2.2 Representative SEM image of CNTs grown directly on a Ni mesh current collector. Image shows that CNTs retain their alignment even after acid dissolution of the Ni.

extracted form the inner walls of the quartz tube that was used as a reaction chamber for CNT growth. The extracted CNTs were in the form of carbon mats. These carbon mats had a long range order in the case of the undoped CNTs while they were more powder like in the case of the NCNTs.

2.3.2 TEM Observations of the Fe Catalyst and CNT Crystallinity

Ferrocene was used as an Fe precursor that was used as the growth catalyst for CNTs. TEM observations were carried out on the Fe particles encapsulated within the undoped CNTs and NCNTs to discern the properties of the growth catalyst that remained after CNT synthesis. These observations indicate that the Fe particles were crystalline and were fully encapsulated inside the graphene matrix in both the undoped CNTs and NCNTs. Figure 2.3 shows representative TEM images of Fe particles in undoped CNTs and NCNTs. In the case of the undoped CNTs, the Fe particles are encapsulated within the innermost walls of the CNTs while the NCNTs appear to grow in either direction of the Fe catalyst.

The synthesized CNTs were crystalline and found to have diameters ranging from 20 – 40 nm and lengths of 15 - 20 μm. Undoped CNTs had ordered sidewalls while NCNTs exhibited disruptions in the graphene stacking consistent with the incorporation of nitrogen. Nitrogen doping introduces pentagonal defects causing dislocations in the hexagonal arrangement of the carbon atoms. Nitrogen doping also caused a noticeable change in the length of crystallinity (L_c) of the NCNTs, consistent with earlier reports.[10]

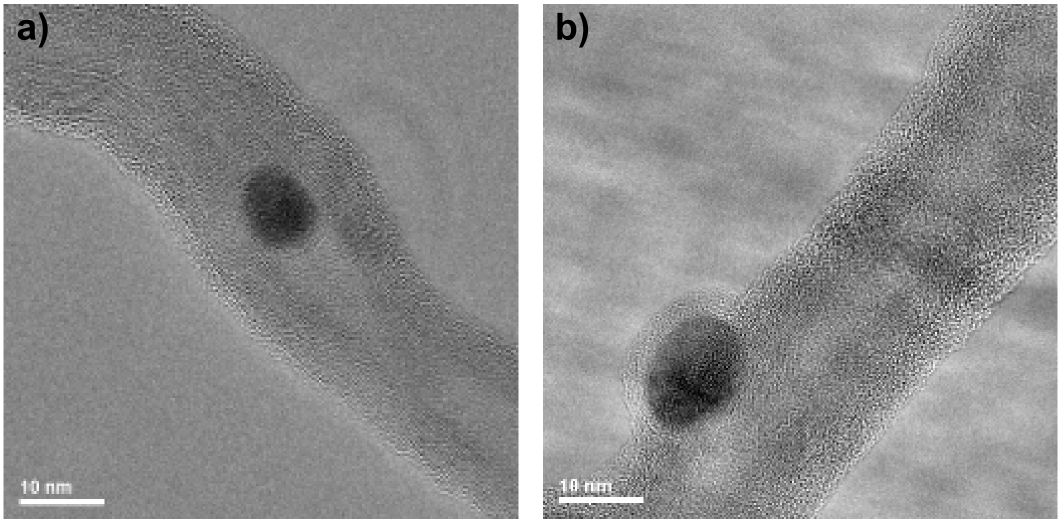

Figure 2.3 Representative TEM images of residual Fe catalyst particles encased within the graphitic sheets of CNTs. a) Encapsulated Fe in undoped CNTs. b) Fe encapsulated within 5 % NCNTs.

2.3.3 Surface Area and Porosity of CNTs

Surface area and porosity measurements were conducted on undoped CNTs and NCNTs to evaluate the effect of an increased surface area and the presence of micropores on ORR activity. Micropores are commonly defined as pores that have widths < 25 Å. Mesopores are pores between 25 – 100 Å while macropores have widths > 100 Å. Porosity and surface area measurements were carried out on the undoped CNTs and NCNTs using nitrogen as the probe molecule. These studies were conducted to determine if there was a difference in the surface area hosted at micropores on NCNTs with increasing nitrogen content that would be consistent with the findings of the Cai group. Earlier reports by Cai et al[28] discuss the activity of nitrogen doped carbons in relation to the incorporation of micropores into the carbon matrix. Cai et al conducted a series of experiments where carbon black was mixed with iron acetate and subjected to heat treatment at 900 ^{0}C under a stream of ammonia. They expected the heat treatment step to incorporate nitrogen atoms into the carbon and also facilitate the formation and activation of micropores in the carbon due to the reaction between the carbon and ammonia. Porosity experiments were also conducted on these carbons before and after the heat treatment steps and the increased activity of the resulting carbons was attributed partially to the formation of micropores in the carbon. Carbons resulting from the heat treatment were found to exhibit no pores between 8.5 – 9 Å and 21.5 – 22.5 Å while the surface area hosted by pores between 7 – 22 Å was found to increase within the first 20 min of heat treatment and subsequently decreased upon further exposure to the heat treatment procedure. A majority (~60 %) of the surface area of these carbons was found to be confined in the micropores while the rest was hosted in mesopores. There was no evidence of the surface area hosted in macropores.

Figure 2.4 shows a plot of the differential surface area vs. the pore width for undoped CNTs and NCNTs. It is seen that a majority of the pores in NCNTs are confined to micropores. Remarkably, micropores at these NCNTs with varying surface concentrations of nitrogen seem to be confined between 5 – 9 Å. In the case of the undoped CNTs, the micropores seem to be confined in a narrower range between 6 – 8 Å. Figure 2.4 also indicates minor differences between the NCNT varieties at pore sizes between 8 – 20 Å. The presence of a small Gaussian feature between 12 – 18 Å for the NCNTs indicates that some of the surface area is confined to pores in that size range. Undoped CNTs were not found to possess pore sizes greater than 9 Å. There was no evidence of the presence mesopores or macropores on the CNTs.

BET surface area measurements were also conducted on the undoped CNTs and NCNTs in order to evaluate the influence of an increase in surface area on the ORR activity. The undoped CNTs had a surface area of 125 m^2 / g while the 4 % NCNTs had a surface area of 130 m^2 / g. Surface area of the NCNTs were found to increase corresponding to increasing nitrogen content with the 7.5 % NCNTs having a surface area of 226 m^2 / g.

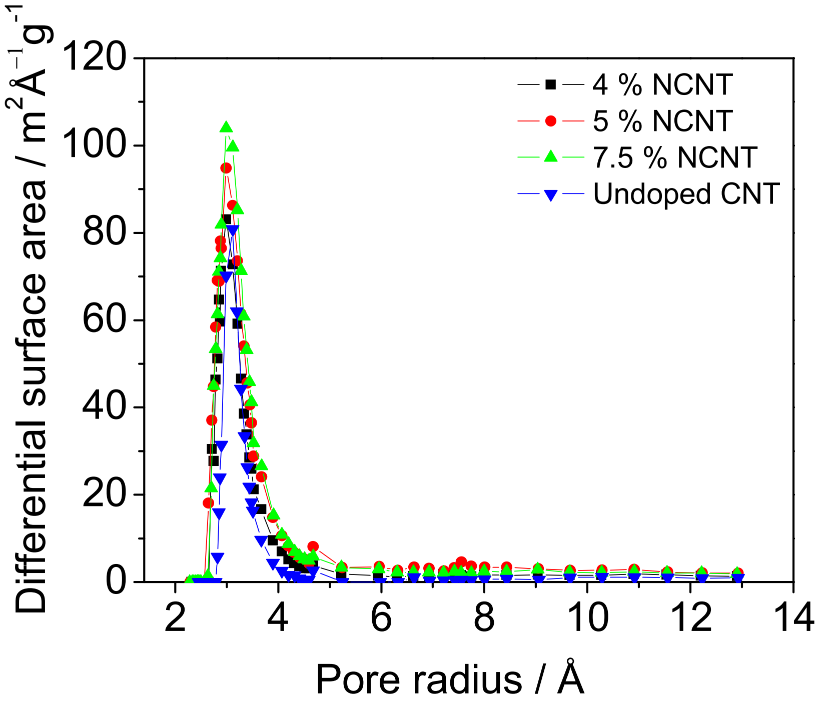

Figure 2.4 Plot of differential surface area corresponding to pore sizes at undoped CNTs and NCNTs measured using nitrogen.

2.3.4 Raman Analysis

2.3.4.1 Raman Analysis at Fe Catalyzed CNTs

Raman analysis was conducted on Fe catalyzed NCNTs to quantify the degree of structural disorder on the NCNTs due to the incorporation of nitrogen on the surface. Previous reports indicate distinct differences in the first order Raman spectra between the undoped CNTs and systematically doped NCNTs.[11] The quantification of D and G bands at 1355 cm^{-1} and 1585 cm^{-1} respectively facilitates study of structural disorder at NCNTs as described by Cuesta et al.[29] Ratios of the integrated intensities of the D and G bands were used to calculate the in plane crystalline length (L_a) at NCNTs with varying nitrogen doping levels. Raman analysis also enabled correlations between the degree of structural disorder and ORR activity at Fe catalyzed NCNTs.[10]

2.3.4.2 Raman Analysis at Ni Catalyzed CNTs

Raman spectra were acquired for Ni based NCNTs to elucidate the extent of structural disorder at these carbons in an effort to compare them to Fe based NCNTs. Figure 2.5 shows a detail of the D and G bands obtained from the Raman spectra between 1000 - 2000 cm^{-1} at Ni based NCNTs. A qualitative comparison of these spectra to Fe based NCNTs showed no discernible differences in the general features of the D and G bands. Spectra were background subtracted and the intensities of the D and G band were integrated to calculate I_D / I_G. This ratio is a quantitative indicator of the degree of structural disorder at these NCNTs and can be used to estimate L_a at these carbons as discussed in earlier sections.[30] Edge plane sites formed at the NCNT surface as a result of the structural disorder have

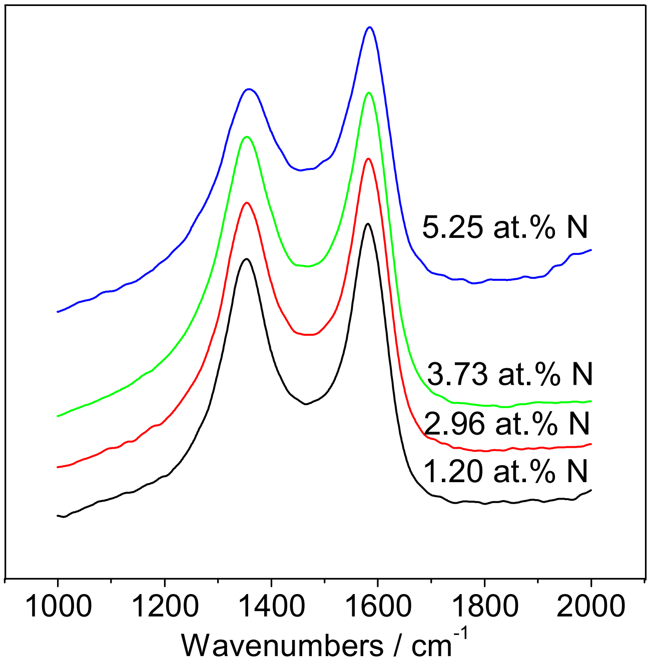

Figure 2.5 Raman spectra showing the D and G bands on nitrogen doped Ni catalyzed NCNTs.

been attributed to an increased activity for ORR. Figure 2.6 shows a plot of the I_D / I_G ratio vs. the pyridinic concentration at Ni based NCNTs. Although there is a decrease in the length of crystallinity from 3.4 nm to 2.8 nm demonstrated by an increase in I_D / I_G for NCNTs with increased nitrogen doping levels, they are quantitatively smaller than that of the Fe based NCNTs (3.4 nm to 1.7 nm) as described by previous literature reports.[11] These quantitative comparisons were made for Ni and Fe based NCNTs that had NH_3 constituting upto 7.5 % of the gas flow stream.

2.3.5 XPS Analysis

2.3.5.1 XPS Analysis at Fe Catalyzed CNTs

XPS studies on nitrogen doping at Fe catalyzed NCNTs indicate the existence of three distinct peaks in the nitrogen area at 398.6 eV, 400.9 eV and 404.2 eV. These peaks are attributed to the pyrrolic, pyridinic and quaternary nitrogen functionalities[31] respectively. A fair degree of ambiguity exists in assigning the peak at 404.2 eV to quaternary nitrogen. Peaks in the near vicinity have been attributed to physisorbed nitrogen[32] in the graphitic lattice and to chemisorbed nitrogen oxide.[33] A systematic study by Maldonado et al. on increasing the nitrogen content on NCNTs revealed an increase in the pyridinic fraction of the total nitrogen content on the NCNT surface.[11]

2.3.5.2 XPS Analysis at Ni Catalyzed CNTs

XPS measurements were performed on systematically doped Ni based NCNTs in an effort to elucidate the nature of the nitrogen species incorporated on the surface and enable correlations to ORR activity. The XPS data on four

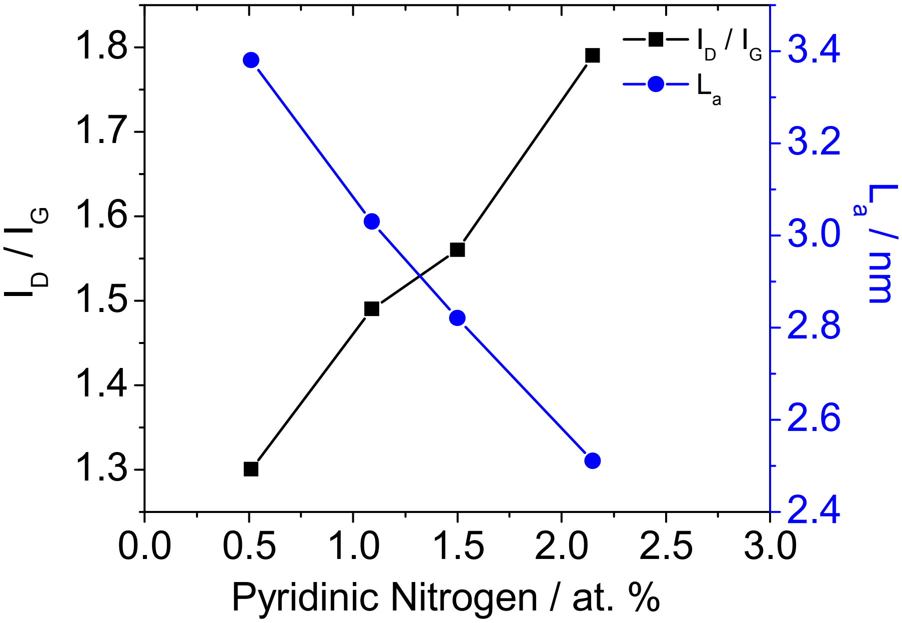

Figure 2.6 Plot of I_D / I_G vs. the pyridinic concentration at Ni based NCNTs. Also shown is the length of crystallinity (L_a) correlating degree of structural disorder to the pyridinic fraction of surface nitrogen.

different Ni based NCNTs with increasing nitrogen contents showed no discernable differences in the oxygen and carbon regions when compared to Fe based NCNTs. The nitrogen region, however, was found to be remarkably different from that of the Fe based NCNTs.

Figure 2.7 shows XPS spectra with high resolution detail of the nitrogen region for Ni based NCNTs with incremental levels of total surface nitrogen concentration. It can be seen that the intensities of peaks assigned to the pyrrolic, pyridinic and quaternary fractions of surface nitrogen are qualitatively different from that reported by Maldonado et al[11] for Fe based NCNTs. The peak near 404 eV as discussed in preceding sections is hereto referred to as the quaternary peak although ambiguity exists as to its particular assignment. While the pyrrolic and quaternary fraction increase almost linearly with an increase in the total nitrogen concentration, the increase in the intensity of the pyridinic peak is less gradual across the entire variety of Ni based NCNTs. These observations are in contrast to observations at Fe based NCNTs as detailed in the subsequent discussion.

Constant flow rates of NH_3 used in Ni catalyzed and Fe catalyzed NCNT synthesis for each variety of carbon resulted in a lower level of nitrogen doping at Ni catalyzed NCNTs. For example when NH_3 constituted 7.5 % of the gas flow stream during Fe catalyzed NCNT synthesis, the resulting carbon had 7.5 at. % nitrogen incorporated on the surface. Under the same conditions for Ni catalyzed NCNT synthesis, the resulting carbon only had 3.7 at. % nitrogen incorporated on the surface.

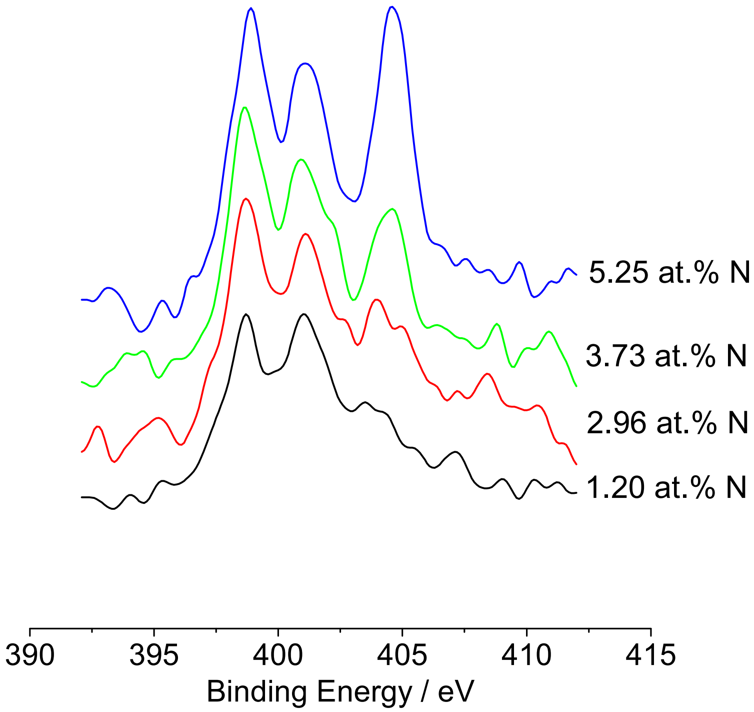

Figure 2.7 XPS spectra showing the nitrogen region in nitrogen doped Ni catalyzed NCNTs.

Quantitative measurements were made on the XPS spectra obtained on the Ni based NCNTs by integrating individual peaks that contributed to the total nitrogen concentration against a Shirley background correction. Literature reports and earlier experiments at the Stevenson research lab have strongly suggested the surface concentration of pyridinic nitrogen as a major factor in promoting ORR at Fe catalyzed NCNTs. A comparison of Ni based NCNTs and Fe based NCNTs that had comparable total surface nitrogen content (4 % NCNT – Fe vs. 3.7 % NCNT – Ni), showed that the distribution of individual nitrogen species (pyridinic, pyrrolic and quaternary) that made up the total concentration was found to be significantly different. Quaternary nitrogen concentrations were found to be relatively minor at 1.2 % NCNTs and 3 % NCNTs but increase dramatically at 3.7 % NCNTs and 5.3 % NCNTs. Earlier reports[11] see a rise in the intensity of the pyrrolic peak at higher overall nitrogen concentrations, but there are no reports of a dramatic rise in the concentration of quaternary/ physisorbed nitrogen.

Figure 2.8 indicates that as the surface nitrogen content increases, the pyrrolic and quaternary fractions in Ni based NCNTs rise in intensity and constitute a majority of the nitrogen content. In the case of Fe based NCNTs, the pyridinic fraction makes up more than 50 % of the total surface nitrogen concentration of NCNTs with total nitrogen concentrations upto 7.5 at. % (3.3 at. % pyridinic nitrogen in Fe catalyzed 7.5 % NCNTs). In contrast to the observations at Fe based NCNTs, Ni based NCNTs seem to support pyridinic fractions that constitute an average of 40 % of the total nitrogen content across a variety of the NCNTs doped with systematically increasing concentrations of

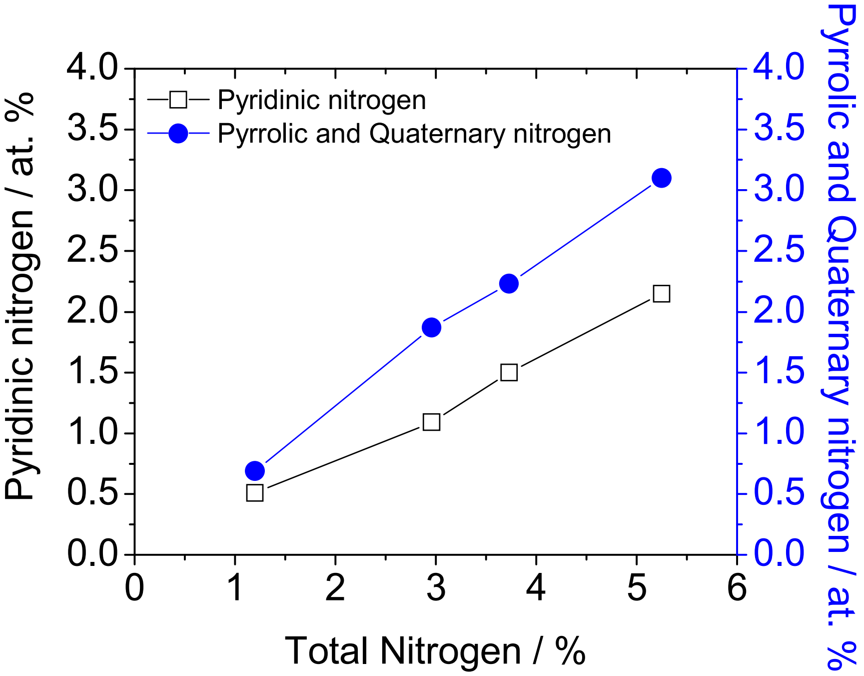

Figure 2.8 Quantitative comparison of the different nitrogen fractions in nitrogen doped Ni catalyzed NCNTs based on XPS spectra.

nitrogen as shown in Figure 2.8. The relative concentration of the pyridinic fraction decreases with increasing nitrogen doping levels with the pyridinic fraction making up 2.1 at. % of the total nitrogen concentration at 5.2 % NCNTs. These observations clearly indicate the differences between nitrogen doping at Fe based NCNTs and Ni based NCNTs especially with regard to the pyridinic nitrogen content.

2.3.6 Effect of Increasing Fe content in CNTs on ORR

This section details experiments performed to discern effects of the Fe catalyst in CNTs on ORR. The first set of experiments was carried out to study the effect of Fe bound to the surface of the CNTs on ORR. A pre-determined mass of 4 % NCNTs was drop cast onto a GC electrode and control ORR studies were conducted in oxygen saturated 0.1 M H_2SO_4. The electrolyte solution was then infused with predetermined volumes of iron sol prepared in accordance with Sorum et al.[34] Fe^{2+} spikes amounting to 1, 2 and 5 mM were injected into the electrolyte with the ORR being run after every subsequent spike. The resulting ORR peak potentials were then compared to the control experiment performed on the blank carbon.

Cyclic voltammograms of ORR performed on the 4 % NCNT with varying Fe spikes is shown in Figure 2.9. It was seen that while there was a slight increase in the current density for ORR in the presence of an Fe spike, there was no effective shift in the peak potential. The increase in current densities were also found to plateau after the first 1 mM spike suggesting no strong correlations to the

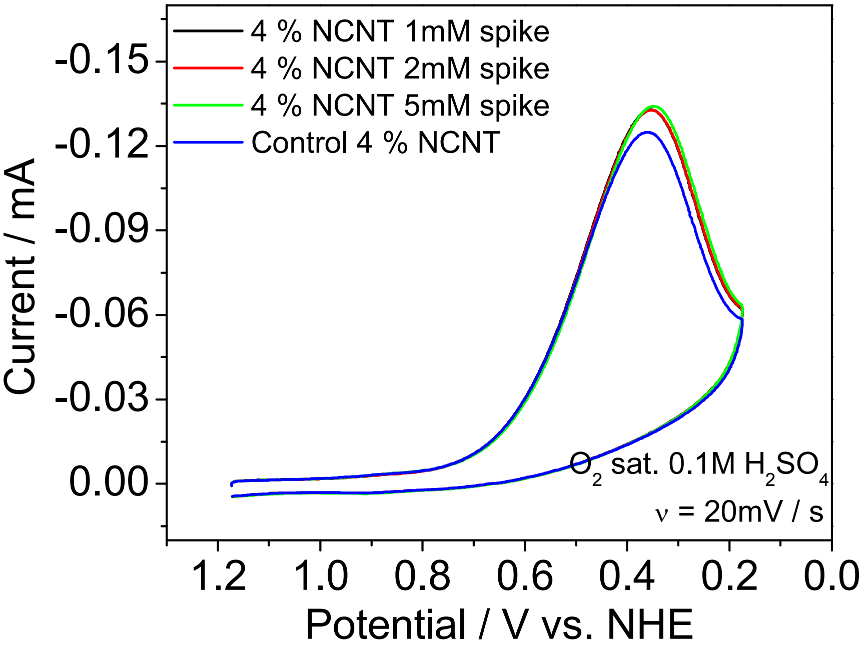

Figure 2.9 Oxygen reduction at 4 % NCNTs with varying concentrations of Fe^{2+} added to the electrolyte solution.

presumed effect on an increased concentration of surface bound Fe^{2+} to an enhanced activity for ORR.

Experiments were also performed to deduce whether an increased concentration of Fe in the precursor mix led to an enhanced activity for ORR at 4 % NCNTs. Accordingly, the concentration of Fe in the precursor mix was increased in predetermined amounts resulting in mass loadings of Fe in the as prepared NCNTs from 11 wt. % to 22.6 wt. %. Fe mass loading in the 4 % NCNTs was measured using TGA analysis. The resulting carbons were analyzed for their activity towards ORR. It was seen that there was a negative effect to an increase in the mass of Fe in NCNTs. Figure 2.10 shows a plot of the peak potential for ORR for each of the 4 % NCNTs synthesized using varying masses of Fe in the precursor mix. The peak potential for ORR shifts negative by ~ 100 mV with an increase in 10 wt. % Fe. XPS measurements conducted on the same carbon samples indicated that there was a decrease in the pyridinic nitrogen fraction by 0.5 at. % corresponding to a decrease in total surface nitrogen content by 1.2 at. % between NCNTs with Fe loadings of 11 wt. % and 22.6 wt. %. These observations suggest a strong correlation between oxygen reduction efficiency and the pyridinic surface nitrogen content rather than Fe content in the NCNTs.

2.3.7 Electrochemical Analysis at CNTs

2.3.7.1 ORR at Fe catalyzed CNTs

The activity of Fe catalyzed NCNTs and undoped CNTs for ORR was tested in oxygen saturated 0.1 M H_2SO_4. Figure 2.11 shows representative cyclic voltammograms for oxygen reduction at undoped CNTs and 4 % and 7.5 %

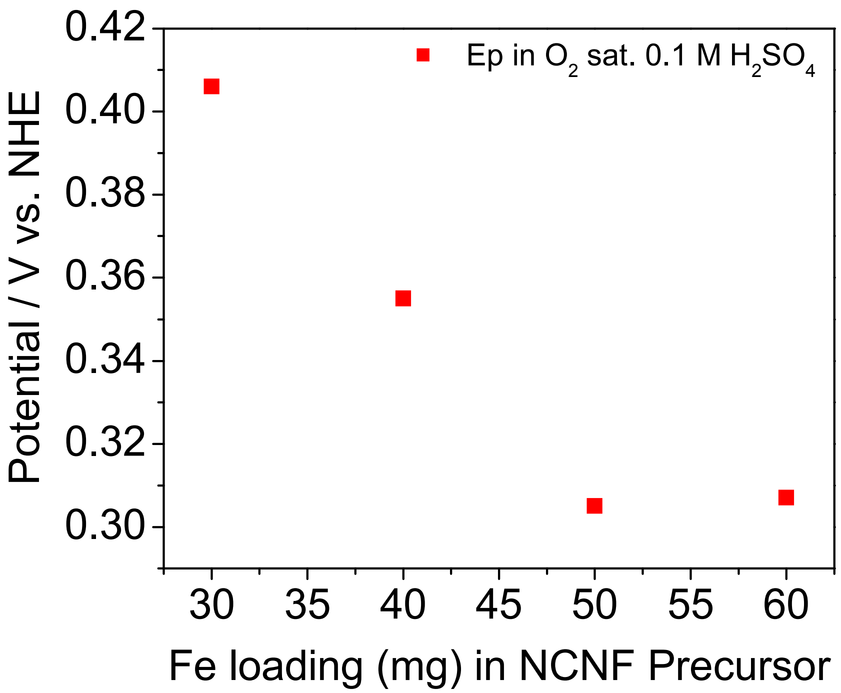

Figure 2.10 Plot showing correlation between peak potential for ORR activity corresponding to mass of iron precursor used to synthesize NCNTs.

NCNTs. The peak potentials for ORR at 4 % and 7.5 % NCNTs are shifted positive by 580 mV and 730 mV respectively compared to the undoped CNTs. Although the commonly accepted explanation for this increase in activity in NCNTs is attributed in general to nitrogen doping, quite a few hypotheses exist as to the exact nature of the active sites that adsorb and reduce oxygen.

Attempts to find a correlation between the surface area and ORR activity at the NCNTs and undoped CNTs were not successful, contradictory to previous reports that attempted to explain enhanced activity at nitrogenated carbons to increased surface areas.[28] While the difference in surface areas between the undoped CNTs and 4 % NCNTs was only 5 m^2 / g, the peak potential for ORR in 0.1 M H_2SO_4 was shifted positive by 580 mV. Peak potentials were shifted positive by 150 mV between 4 % NCNTs and 7.5 % NCNTs although the difference in surface areas was 96 m^2 / g indicating no strong correlations between surface area and activity at undoped CNTs and NCNTs. While the undoped CNTs and NCNTs had pore size distributions within the same range as described in a previous section dealing with surface area and porosity, the ORR activity at NCNTs is significantly higher than undoped CNTs as shown in Figure 2.11. These observations suggest that the presence of micropores at these carbons does not seem to be an influencing factor in the enhanced activity for ORR at NCNTs.

The cyclic voltammetry data viewed in conjunction with the Raman analysis reveals that there was an inverse relationship between the activity for ORR at CNTs and NCNTs with L_a values at these carbons. This is evidenced by a

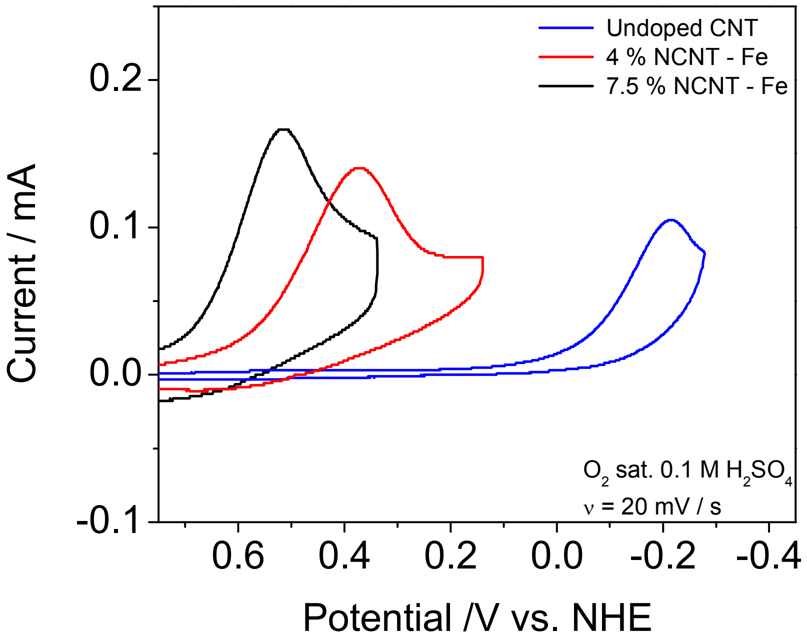

Figure 2.11 ORR activity for undoped CNTs and NCNTs in oxygen saturated 0.1 M H_2SO_4. $\nu = 20$ mVs^{-1}

decrease in L_a from 3.4 nm to 1.7 nm for the 4 % NCNTs and 7.5 % NCNTs respectively. These studies provide strong arguments that systematic induction of structural disorder on the NCNT surface characterized by an increase in edge plane sites corresponding to nitrogen doping plays an important role in the adsorption and reduction of oxygen at these sites.

2.3.7.2 ORR at Ni Catalyzed CNTs

Figure 2.12 shows representative cyclic voltammograms for ORR at Ni catalyzed NCNTs containing 3.7 at. % N compared to Fe based undoped CNTs and NCNTs containing 4 and 7.5 at. % N in oxygen saturated 0.1 M H_2SO_4. The Ni catalyzed NCNTs are more active for ORR compared to Fe catalyzed undoped CNTs. The peak potential for ORR was shifted positive by ~360 mV for the Ni catalyzed NCNTs against the undoped CNTs. The peak potential for ORR at Fe based 4 % NCNTs was shifted positive by ~ 220 mV compared to the Ni based NCNTs. While the 3.7 % Ni based NCNTs had a slightly lower overall surface nitrogen concentration than the 4 % NCNTs, the pyridinic fraction at the Ni NCNTs was found to be 1.5 at. % compared to 2.1 at. % found in Fe based 4 % NCNTs offering a correlation for ORR activity to the amount of pyridinic nitrogen.

The voltammetry data correlate well with Raman observations at the Ni based NCNTs. Raman analysis suggests a lower degree of structural disorder corresponding to an increase in surface nitrogen content at Ni based NCNTs compared to Fe based NCNTs (as detailed in the Raman analysis section). This results in a smaller number of edge plane sites that are more active than regular

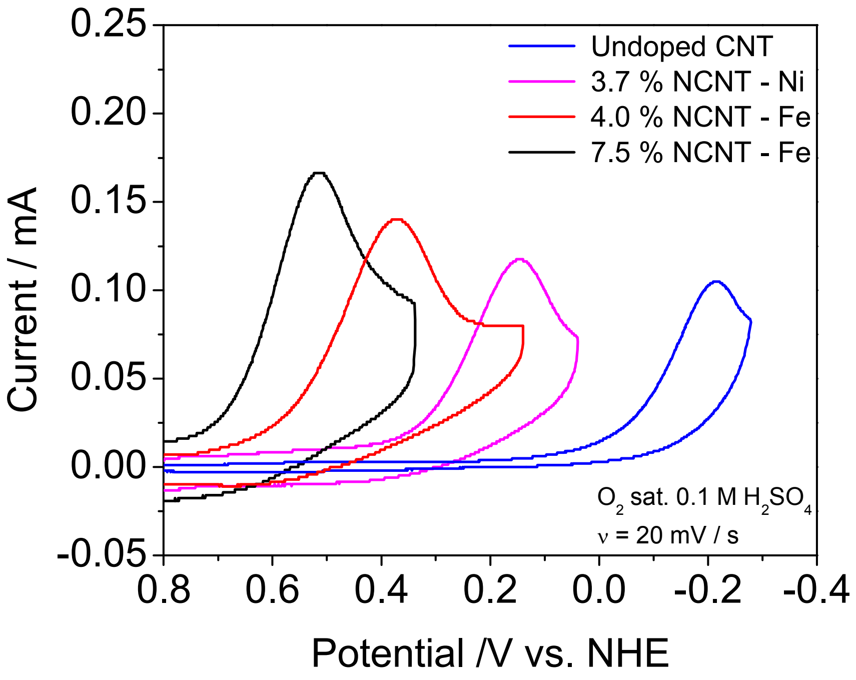

Figure 2.12 Comparison of cyclic voltammograms for ORR at undoped CNTs and NCNTs synthesized using Fe and Ni precursors in oxygen saturated 0.1 M H_2SO_4. $\nu = 20\ mVs^{-1}$.

basal plane sites for adsorption and reduction of oxygen. Figure 2.13 shows a plot of 1 / L_a values calculated for Fe and Ni based NCNTs with respect to E_p values for ORR at the corresponding carbons. A direct correlation between these two parameters emphasizes the effect of edge plane sites on ORR activity.

2.3.7.3 Effect of Pyridinic Nitrogen on ORR

A plot correlating the amount of pyridinic nitrogen at Ni and Fe based NCNTs to the peak potential for ORR at these carbons is shown in Figure 2.14. The pyridinic fraction was calculated for each of the NCNTs by performing a quantitative analysis of the peak near 400 eV with respect to the total nitrogen concentration on the NCNT surface. It is seen that the peak potential for ORR shifts by ~750 mV corresponding to an increase of 2.7 at. % pyridinic nitrogen across the entire variety of carbons. This corresponds to a positive shift of ~ 295 mV with respect to an increase in each at. % of pyridinic nitrogen in the Fe based NCNTs. No strong correlations were found between pyrrolic and quaternary nitrogen contents with ORR activity.

Figure 2.14 shows that the Ni based NCNTs and the Fe based NCNTs have ORR activities that track well with the pyridinic nitrogen content (R^2 = 0.99). A lesser degree of correlation (R^2 = 0.94) was seen with ORR activities compared to total nitrogen content as seen in Figure 2.15. These results are a clear indication that the ORR activity at these NCNTs is independent of the Fe or Ni catalyst that was used in the synthesis of these NCNTs. Earlier reports by Maldonado et al.[11] have correlated the amount of pyridinic fraction of the total nitrogen content to the amount of edge plane sites created due to the nitrogen

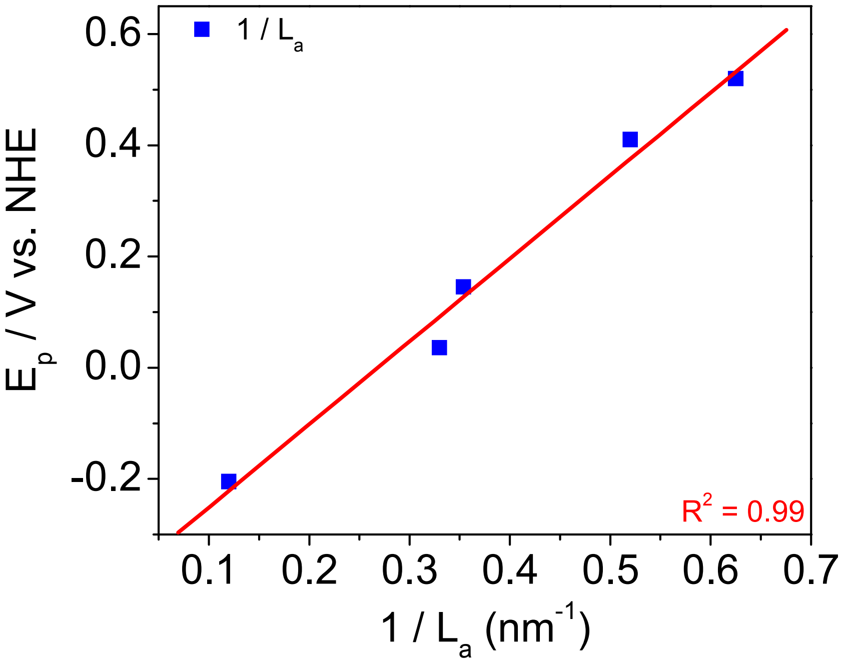

Figure 2.13 Plot showing correlation between peak potential for ORR activity corresponding to edge plane content calculated from Raman spectra at Fe and Ni based NCNTs. ORR activity was measured in oxygen saturated 0.1 M H_2SO_4.

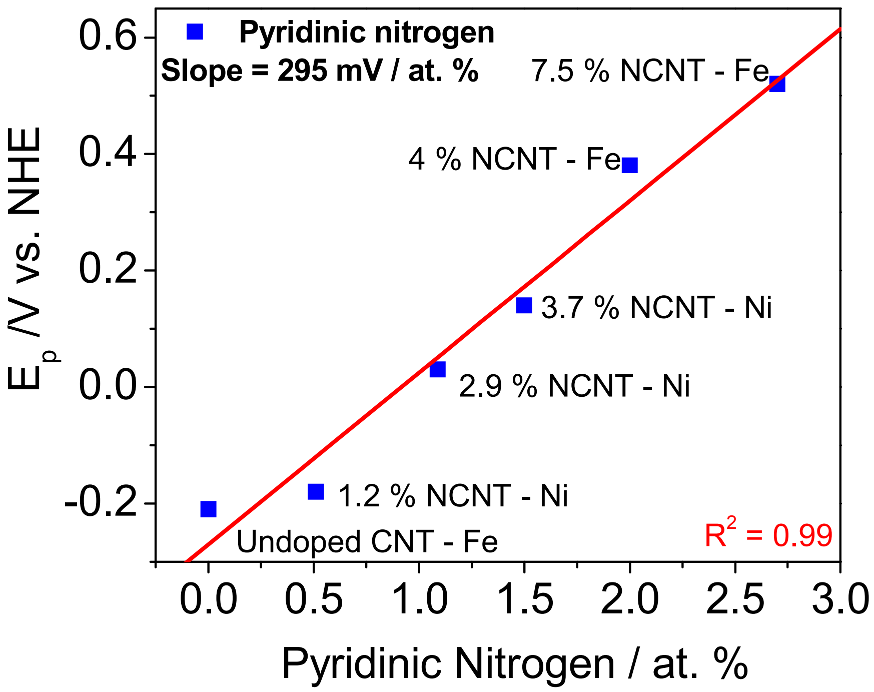

Figure 2.14 Plot showing correlation between peak potential for ORR activity corresponding to the pyridinic nitrogen fraction at Fe and Ni based NCNTs. ORR activity was measured in oxygen saturated 0.1 M H_2SO_4.

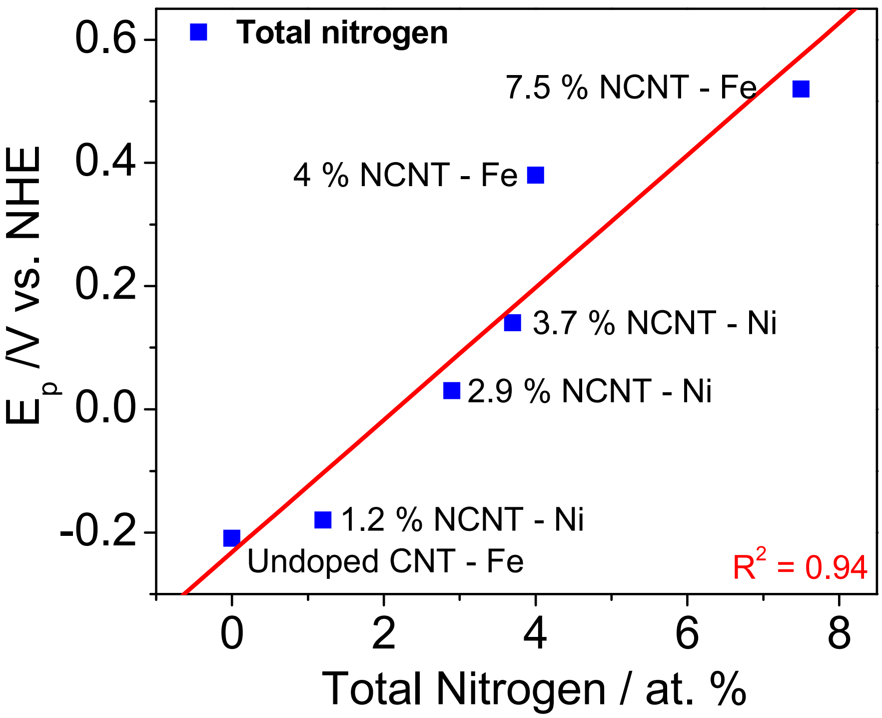

Figure 2.15 Plot showing correlation between peak potential for ORR activity corresponding to the total nitrogen content at Fe and Ni based NCNTs. ORR activity was measured in oxygen saturated 0.1 M H_2SO_4.

doping in conjunction to Raman analysis at NCNTs. These background studies and the present set of data as shown in Table 2.1 compile a strong correlation for ORR activity to the pyridinic nitrogen content and the presence of edge plane sites at the NCNT surface.

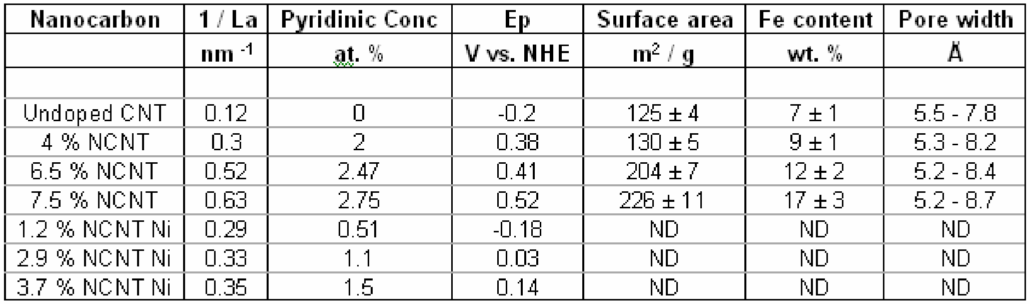

Nanocarbon	1 / La	Pyridinic Conc	Ep	Surface area	Fe content	Pore width
	nm $^{-1}$	at. %	V vs. NHE	m^2 / g	wt. %	Å
Undoped CNT	0.12	0	-0.2	125 ± 4	7 ± 1	5.5 - 7.8
4 % NCNT	0.3	2	0.38	130 ± 5	9 ± 1	5.3 - 8.2
6.5 % NCNT	0.52	2.47	0.41	204 ± 7	12 ± 2	5.2 - 8.4
7.5 % NCNT	0.63	2.75	0.52	226 ± 11	17 ± 3	5.2 - 8.7
1.2 % NCNT Ni	0.29	0.51	-0.18	ND	ND	ND
2.9 % NCNT Ni	0.33	1.1	0.03	ND	ND	ND
3.7 % NCNT Ni	0.35	1.5	0.14	ND	ND	ND

Table 2.1 Comparison of parameters derived from Raman, XPS, cyclic voltammetry, surface area analysis and TGA analysis for Fe and Ni catalyzed NCNTs.

2.4 CONCLUSIONS

The ability to tune the physicochemical properties such as length, diameter, structural orientation and composition of as grown Fe or Ni catalyzed NCNTs was established. Structural and compositional variations brought upon by systematic nitrogen doping on CNTs as quantified by Raman and XPS analysis were correlated to the enhanced activity for ORR at the surface of these NCNTs. These studies provide fundamental knowledge that can be used in understanding and manipulating NCNTs for use as metal catalyst supports for ORR as dealt with in subsequent chapters.

2.5 REFERENCES

1. Planeix, J. M.; Coustel, N.; Coq, B.; Brotons, V.; Kumbhar, P. S.; Dutartre, R.; Geneste, P.; Bernier, P.; Ajayan, P. M. *J. Am. Chem. Soc.* **1994**, *116*, 7935.

2. McCreery, R. L. Carbon Electrodes: Structural Effects on Electron Transfer Kinetics. In *Electroanalytical Chemistry*; Bard, A. J., Ed.; Dekker: New York, 1991; Vol. 17.

3. Glenis, S.; Nelson, A. J.; Labes, M. M. *Journal of Applied Physics* **1999**, *86*, 4464.

4. Endo, M.; Hayashi, T.; Hong, S. H.; Enoki, T.; Dresselhaus, M. S. *J. Appl. Phys.* **2001**, *90*, 5670.

5. Berber, S; Kwon, Y-K.; Tomanek, D. *Phys. Rev. Lett.* **2000**, *84*, 4613.

6. Nevidomskyy, A. H.; Csanyi, G.; Payne, M. C. *Phys. Rev. Lett.* **2003**, *91*, 105502.

7. Kaneko, K.; Ishii, C.; Ruike, M.; Kuwabara, H. *Carbon*, **1992**, *30*, 1075.

8. Sharda, T.; Soga, T.; Jimbo, T.; Umeno, M. *Diamond Relat. Mater*. **2000**, *9*, 1331.

9. Maldonado, S.; Stevenson, K. J. *J. Phys. Chem. B* **2004**, *108*, 11375.

10. Maldonado, S.; Stevenson, K. J. *J. Phys. Chem. B* **2005**, *109*, 4707.

11. Maldonado, S.; Morin, S.; Stevenson, K. J. *Carbon* **2006**, *44*, 1429.

12. Brezina, M.; Jindra, J.; Mrha, J. *Coll. Czech. Chem. Comm.* **1967**, *33*, 2363.

13. Boehm, H. P.; Mair, G.; Stoehr, T.; DeRincon, A. R.; Tereczki, B. *Fuel* **1984**, *63*, 1061.

14. Lahaye, J.; Nanse, G.; Bagreev, A.; Strelko, V. *Carbon* **1999**, *37*, 585.

15. Sjostrom, H.; Stafstrom, S.; Boman, M.; Sundgren, J. E. *Phys. Rev. Lett.* **1995**, *75*, 1336.

16. Stohr, B.; Boehm, H. P.; Schlogl, R. *Carbon* **1991**, *29*, 707.

17. Wang, H.; Cote, R.; Faubert, G.; Guay, D.; Dodelet, J. P. *J. Phys. Chem. B* **1999**, *103*, 2042.

18. Gooding, J. J. *Electrochimica Acta* **2005**, *50*, 3049.

19. Chou, A.; Bocking, T.; Singh, N. K.; Gooding, J. J. *Chem. Commun*. **2005**, *7*, 842.

20. Banks, C. E.; Moore, R. R.; Davies, T. J.; Compton, R. G. *Chem. Commun*. **2004**, *16*, 1804.

21. Salimi, A.; Banks, C. E.; Compton, R. G. *Analyst*, **2004**, *129*, 225.

22. Strelko, V. V.; Kuts, V. S.; Thrower, P. A. *Carbon* **2000**, *38*, 1499.

23. Sidik, R. A.; Anderson, A. B.; Subramanian, N. P.; Kumaraguru, S. P.; Popov, B. N. *J. Phys. Chem. B* **2006**, *110*, 936.

24. Jouen, F.; Charreteur, F.; Dodelet, J. P. *J. Electrochem. Soc.* **2006**, *153*, A689.

25. Sljukic, B.; Banks, C. E.; Compton, R. G. *Nano Lett*. **2006**, *6*, 1556.

26. Lyon, J. L.; Stevenson, K. J. *Langmuir* **2007**, *in press*.

27. Schmidt, J.; Gasteiger, H. A; Stab, G. D.; Urban, P. M.; Kolb, D. M.; Behm, R. J. *J. Electrochem. Soc.* **1998**, *145*, 2354.

28. Jaouen, F.; Lefevre, M.; Dodelet, J. P.; Cai, M. *J. Phys. Chem. B* **2006**, *110*, 5553.

29. Cuesta, A.; Dhamelincourt, P.; Laureyns, J.; Martinezalonso, A.; Tascon, J. M. D. *Carbon* **1994**, *32*, 1523.

30. Sjostrom, H.; Stafstrom, S.; Boman, M.; Sundgren, J. E. *Phys. Rev. Lett.* **1995**, *75*, 1336.

31. Stohr, B.; Boehm, H. P.; Schlogl, R. *Carbon*, **1991**, *29*, 707.

32. Choi, H. C.; Park, J.; Kim, B. *J. Phys. Chem. B* **2005**, *109*, 4333.

33. Biniak, S.; Szymanski, G.; Siedlewski, J.; Swiatkowski, A. *Carbon* **1997**, *35*, 1799.

34. Sorum, C. H. *J. Am. Chem. Soc*. **1928**, *50*, 1263.

CHAPTER 3

Synergistic Assembly of Dendrimer Templated Catalysts and Nitrogen Doped Carbon Nanotube Electrodes for Oxygen Reduction

3.1 INTRODUCTION

High surface area carbons such as Ketjenblack and Vulcan carbon used as supports for electrocatalysis applications are beneficial in terms of providing electronic conductivity and high dispersion of metal catalysts.[1,2] Unfortunately, the multitude of preparation strategies for carbon supported catalysts makes it difficult to understand the role of the carbon support on electrocatalysis including the degree of catalyst utilization, promotion of catalyst-support interactions, and the stability of the catalyst towards dissolution, agglomeration, and other degradation processes. Moreover, carbon supports are typically prepared via aggressive processes for activation including refluxing in concentrated acids[3] (HNO_3, H_2SO_4, HCN) or strong oxidizing agents[4] (H_2O_2, $KMnO_4$) to create surface functionalities (carbonyl, carboxylate, ester-like oxygen, alcohol) to facilitate more efficient anchoring and loading of the metal catalyst via impregnation[5], coprecipitation[6], microemulsion[7] or sonochemical[8] methods. The activation methods often significantly degrade the preferred structural and compositional properties of both the carbon support and active metal catalyst and have typical drawbacks of large average catalyst size, broad size distribution, and poor reproducibility.[9] Of vital importance is the need to significantly improve catalyst dispersion and utilization (typically <20% is catalytically active) on the carbon support, and to reduce catalyst sintering and poisoning processes. Carbon nanotubes (CNTs) have attracted significant interest as catalyst supports after their recent discovery,[10] as they have optimal electronic conductivity, proper surface area and pore structure.[11,12,13,14] While as synthesized CNTs have some of the desirable properties required for supports, efficient anchoring and utilization of loaded metal catalysts is still achieved through extensive surface modification of the CNTs[15,16,17] using some of the aggressive and time consuming conditioning protocols listed above. To this end, we have been exploring facile synthetic strategies for preparing both robust, high surface area nitrogen doped CNT supports[18,19] and active metal catalysts with well controlled properties that circumvent the majority of processing steps required by more traditional loading routes, such as washing, drying, calcination, and reduction.

This chapter describes the use of nitrogen doped carbon nanotube (NCNT) supports [19] that strongly bind size monodisperse mono- and bimetallic dendrimer encapsulated catalysts prepared by a dendrimer template method[20] without necessitation for covalent[21] or non-convalent[22] functionalization of the carbon support prior to catalyst loading. The dendrimer template method of synthesizing nanoparticles is versatile since a variety of nanoparticle properties such as size, structure and composition[23] can be modified with relative ease compared to various other methods[24,25,26] employed to synthesize nanoparticles. The ability to modify properties of the interior and exterior functional groups in a dendrimer template facilitates control of the way in which precursor metal ions coordinate within the dendrimer template. This is due to a difference in basicity between the interior and exterior functional groups in the dendrimer. For example, in the case of amine terminated dendrimers, the interior amines have a pK_a value of 6.30 while the exterior amines have a pK_a value of 9.23 which facilitates easier protonation of the exterior amines and thus allows for selective coordination of metal ions with the interior amines. The presence of specific functionalities on the dendrimer exterior also provides an efficient way to anchor the resultant encapsulated nanoparticle to a specific substrate. For example the Crooks group has shown that amine terminated PAMAM dendrimers show strong adsorption to HOPG.[27] The use of a particular dendrimer generation allows for efficient control of size of the nanoparticle based on the number of available interior functional groups that coordinate with metal ions from the precursor.[23,24,25] While the diameter of the dendrimer molecule increases logarithmically with each dendrimer generation, the number of functional groups increases exponentially. For this particular study, PAMAM generation 4, amine terminated dendrimers (G4-NH_2) were used. The number (62) of interior functional groups in G4 dendrimers was best suited to synthesize ~2 nm size nanoparticles and the amine terminated peripheral functional groups allowed for facile adsorption onto NCNTs.

Scheme 1 demonstrates the basic approach for the assembly of the CNT-DEN composites. The advantage of this scheme is that the compositional and structural properties of both the carbon support [18] and dendrimer encapsulated Pt

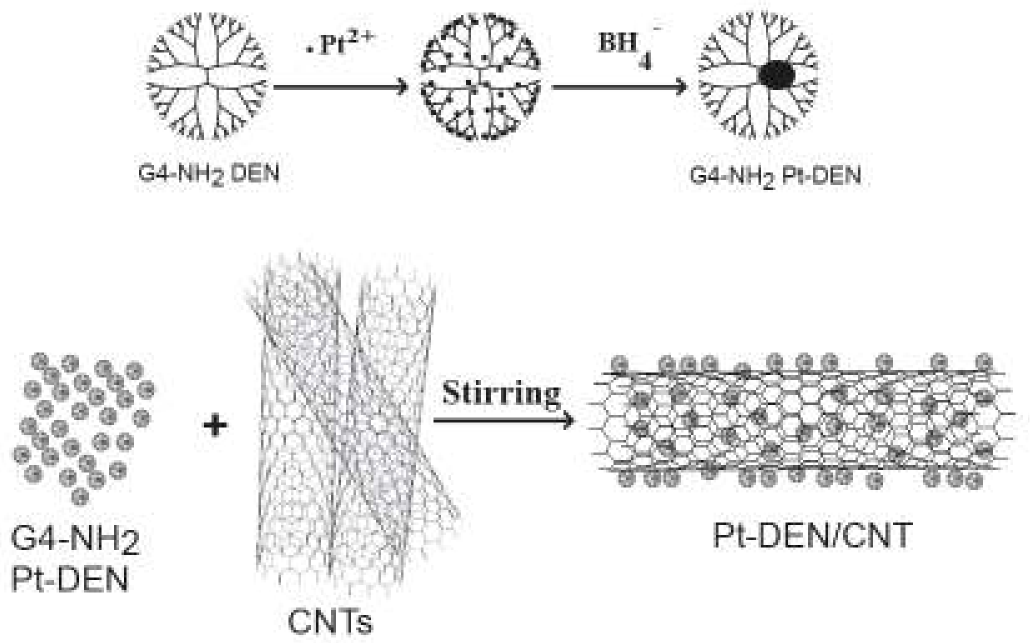

Scheme 3.1 Preparation of amine terminated PAMAM dendrimer encapsulated Pt nanoparticles (G_4-NH_2 Pt-DENs) and adsorption onto carbon nanotube (CNT) supports.

nanoparticle (Pt-DEN) catalyst can be reproducibly prepared and synergistically tuned to directly assemble carbon-supported catalyst composites via adsorption from aqueous solution. This chapter focuses on the uniform dispersion and loading of dendrimer encapsulated mono- and bimetallic catalysts supported on undoped CNTs and NCNTs that show enhanced catalytic behavior for the oxygen reduction reaction (ORR) in fuel cells. The ability to prepare high quality, well dispersed supported metal catalysts, with sizes in the 2-5 nm range that avoid painstaking and lengthy synthetic and post processing activation steps is required to advance electrocatalysis performance.

3.2 EXPERIMENTAL

3.2.1 Synthesis of Monometallic Dendrimer Encapsulated Nanoparticles

Fourth generation, amine terminated, poly(amidoamine) PAMAM dendrimers ($G4\text{-}NH_2$) (Dendritech) were used as templates to prepare Pt-DENs and Pd-DENs. The $G4\text{-}NH_2$ templates were received in a 10 % methanol solution that was removed under vacuum prior to DEN synthesis. K_2PtCl_4 and K_2PdCl_4 (Aldrich) were used as precursors for Pt and Pd DENs respectively.[27] A carefully measured volume of $G4\text{-}NH_2$ dendrimers was dried off methanol and suspended in a pH adjusted HCl solution (pH 5 for Pt-DENs and pH 3 for Pd-DENs) resulting in 5 – 20 μM dendrimer solutions. This pH adjustment facilitated in selective protonation of the exterior amines. Aqueous 0.1 M K_2PtCl_4 or 0.1 M K_2PdCl_4 constituting 40 mol equivalent of the dendrimers was added to the dendrimer solution. A slight increase in pH resulting from the addition of the metal precursors was countered with addition of small aliquots of dilute 0.1 M HCl until the acidity was restored to the original pH levels. The resulting solution was left to stir for 72 hrs due to sluggish co-ordination times between the Pt ions and interior amines.[28,29] Pd co-ordination rates were much faster with the reaction happening within 30 min. A 20 mol excess (w.r.t metal ion concentration in solution) of 0.5 M $NaBH_4$ (Fisher) was added drop by drop after allowing for appropriate co-ordination times. The resulting DEN solutions were dark brown in color which is consistent with the formation of nanoparticles by reduction. After reduction the DEN solutions were adjusted to pH 8 to prevent agglomeration of the nanoparticles. Following pH adjustment the DEN solutions were subjected to dialysis against 10 L of 18 MΩ cm nanopure water for 12 hrs to remove impurities resulting from the synthesis. Cellulose dialysis sacks with MWCO 12000 (Sigma) were employed in the dialysis step.[30] Dialyzed DEN solutions were stored in acid washed airtight vials prior to further analysis.

3.2.2 Synthesis of Bimetallic Dendrimer Encapsulated Nanoparticles

Bimetallic PdAu DENs were synthesized primarily to compare ORR activity at a non Pt based catalyst and to gain insight into ORR activity at a Pd alloy surface. A carefully measured volume of G4-NH_2 dendrimers was dried off methanol and suspended in an aqueous HCl solution that was adjusted to pH 3 resulting in a 20 μM dendrimer solution. A 0.1 M K_2PdCl_4 solution constituting 20 mol equivalent of the dendrimers was added to the dendrimer solution and the pH was adjusted back to 3. Pd ions were allowed to coordinate with the interior amines for 30 min after which a 20 mol equivalent of 0.1 M $HAuCl_4$ was added and the solution allowed to stir for an additional 10 min. A 20 mol excess 0.5 M $NaBH_4$ solution was added drop by drop after stirring was completed and pH of the resultant DEN solution was adjusted to 8 to prevent agglomeration. The resulting DEN solution was brown in color and was dialyzed against 10 L of 18 MΩ nanopure water for 12 hrs to remove impurities resulting from the synthesis. The same type of dialysis sacks used for the monometallic DENs (cellulose with 12000 MWCO) was used in the dialysis step. PdAu DEN solutions were stored in acid washed airtight vials prior to further analysis. While a number of synthesis protocols[31] like co-complexation and sequential loading using quaternized dendrimers have been utilized to prepare bimetallic particles, this present scheme was suited for studies on ORR activity at PdAu surfaces.

3.2.3 Synthesis of Undoped CNTs and NCNTs

CNTs were prepared using the floating catalyst chemical vapor deposition method[18,19] described in chapter 2. Briefly, xylene (Aldrich) as carbon source and ferrocene (Aldrich) as catalyst were used for the growth of the undoped CNTs while a pyridine (Fisher) and ferrocene precursor combination was used for the synthesis of nitrogen-doped CNTs. The use of a pyridine precursor allowed for a controlled doping of ~ 4 at. % N on the NCNT surface. Higher surface nitrogen concentrations (5-10 at. % N) were obtained by introducing a regulated stream of ammonia gas (Aldrich) into the CVD furnace system along with the pyridine and ferrocene precursors. As grown undoped CNTs and NCNTs were carefully extracted from the inner walls of the quartz tube used as a reaction chamber and stored in airtight vials prior to characterization and further use.

3.2.4 Adsorption of Pt-DENs on CNTs and NCNTs

Pt-DEN standard solutions ranging from 5-20 μM were prepared and characterized using UV-Vis spectroscopy using a Varian Cary 5000 instrument by monitoring the featureless absorption at 350 nm that reports on the formation and concentration of colloidal Pt. A calibration curve from 0-20 μM was constructed to follow the adsorption of the Pt-DENs onto the various CNT supports by monitoring the decrease in absorbance of the supernatant at 350 nm as a function of immersion time from 1 to 24 h for a 1 mg/ml carbon sample dispersed in a stirred solution containing known amounts of Pt-DENs.[32] The absorbance at 350 nm has been attributed to the presence of colloidal Pt resulting from the synthesis.[27] A calibration curve was constructed from absorbance values at 350 nm from Pt-DEN solutions of varying concentrations from 5-20 μM.

Absorbance readings were taken every 30 min during the adsorption process by first centrifuging the solution for 2 min so as not to withdraw any of the CNTs suspended in solution. A 3 ml volume of the supernatant was then carefully withdrawn from solution and placed in a quartz cuvette used for absorbance measurements. After the measurements were completed, the supernatant was injected back into the CNT/ DEN solution and the adsorption process was allowed to continue accompanied by stirring. Nylon filters (GE corp.) with an average of 0.2 μm pore size were employed in the filtration process. Background experiments revealed that the filters did not adsorb any significant quantities of the DENs. After the initial 3 hrs, measurements were taken every hour since the adsorption slowed down considerably. While the NCNTs used in this experiment were hydrophilic and went into solution immediately after introduction, the undoped CNTs were not and took longer times to be completely wet in solution. Care was taken to ensure that CNTs were well dispersed before they were introduced into the DEN solution. In the case of 7.5 % NCNTs, the DEN solution was regenerated with a fresh solution after absorbance measurements indicated complete adsorption of DENs from the initial solution. These studies were conducted to measure the maximum amount of adsorption of DENs at the NCNTs. Once the adsorption process was deemed complete, the CNT / DEN solutions were centrifuged and the supernatant was extracted carefully. The resultant CNT/ Pt-DEN composites were washed with de ionized water and allowed to dry. Pt-DEN composites were stored in air tight vials prior to further analyses.

3.2.5 Electron Microscopy

Transmission electron microscope (TEM) analysis of the CNTs was performed on a JEOL 2010F instrument operating at 200 kV. DEN samples were drop cast on a Cu TEM grid covered with a thin layer of amorphous carbon and allowed to dry overnight in a dessicator prior to TEM analysis. CNT samples with adsorbed DENs were allowed to dry after recovery from the DEN solution and suspended in anhydrous ethanol prior to drop casting on a lacey carbon covered Cu TEM grid.

3.2.6 Thermo Gravimetric Analysis

Thermo gravimetric analysis (TGA) was performed using a Perkin Elmer 7000 TGA. CNT/ DEN samples (3-5 mg) were held in platinum pans heated to 800 $^{\circ}$C in flowing air (Praxair, 99.998%) at a rate of 5 ^{0}C / min. The resulting mass contained Fe_2O_3 from the residual Fe catalyst in the CNTs and Pt from Pt-DENs. Control TGA studies performed using particular varieties of the blank CNTs enabled the mass of hematite to be subtracted facilitating calculations of the mass loading of Pt on CNTs.

3.2.7 Electrochemistry at CNT/ DEN Composites

Electrochemical measurements were carried out on an EG&G Instruments 263A potentiostat equipped with a Pine Instruments MSRX controller for rotating disk electrode (RDE) measurements. Data acquisition and analysis was performed on a Corrware (Scribner Associates) software package. CNT/ DEN sample slurries prepared with 0.15 wt. % nafion in anhydrous ethanol and de-ionized water were drop cast as a film on a glassy carbon (GC) RDE (0.5 cm diameter, Pine Instruments) polished to a mirror finish and allowed to dry under a stream of Ar (Praxair 99.98%) prior to electrochemical measurements.

Cyclic voltammograms were obtained in a standard three electrode cell with a gold counter electrode and an Hg/Hg_2SO_4 reference electrode in O_2 (Praxair) saturated 0.1 M H_2SO_4 prepared with deionized water (>18 MΩ cm). All potentials were converted to NHE for comparison to literature values. Prior to oxygen reduction, the CNT/ DEN film was cycled between 0.8 and -0.2V in order to make the film hydrophilic and achieve steady state voltammograms. This step was primarily used for undoped CNT/ DEN catalyst films that required atleast 10 CV cycles before exhibiting hydrophilicity. NCNTs on the other hand are easily wettable due to the presence of positively charged nitrogen groups on the surface and to the existence of more edge plane sites than the undoped CNTs.

Rotating disk electrode measurements were performed on the same films after the completion of cyclic voltammetry measurements. The electrode was rotated between 250 and 2000 rpm in increments of 250 rpm except for the potentiodynamic voltammogram obtained at 1600 rpm.[33] The electrolyte solution was replenished with O_2 in between two potentiodynamic measurements and also between consecutive CVs. Potentials were typically scanned from 1 V vs. NHE to 0 V vs. NHE.

3.3 RESULTS AND DISCUSSION

3.3.1 Structure and Composition of DENs

A representative TEM image in Figure 3.1 shows G4 NH_2 Pt-DENs from a 20 μM solution. The particles are well dispersed and do not exhibit any agglomeration. The corresponding histogram reveals that the particle size distribution is narrow and nearly monodisperse consistent with earlier reports.[27] The average diameter of the Pt nanoparticles was found to be 2.2 ± 0.3 nm. Pd-DENs had an average diameter of 2.0 ± 0.4 nm (Figure 3.2) while the PdAu DENs (Figure 3.3) had average diameters of 2.3 ± 0.4 nm. Energy dispersive spectroscopy (EDS) analysis performed on single PdAu nanoparticles (Figure 3.4) showed that these were bimetallic and had compositions of Pd 31 ± 5 % and Au 69 ± 5 %. The standard deviations result from challenges associated with obtaining reliable EDS spectra from particles smaller than 2 nm.[31] The TEM images also show that the DENs are crystalline as evidenced from observations of lattice structures.

3.3.2 Analysis of Pt-DEN Adsorption at Undoped CNTs and NCNTs

Pt-DEN adsorption measurements were performed on undoped CNTs and NCNTs by monitoring the absorbance at 350 nm over 24h. Figure 3.5 shows a representative adsorption profile for Pt-DENs on 4 % NCNTs over a 24h period. The absorbance between 200- 800 nm is seen to decrease consistently as a function of time corresponding to a lowering of the DEN concentration in the supernatant. The broad absorbance between 300 – 800 nm has been associated with the presence of colloidal Pt and is seen to decrease until no significant

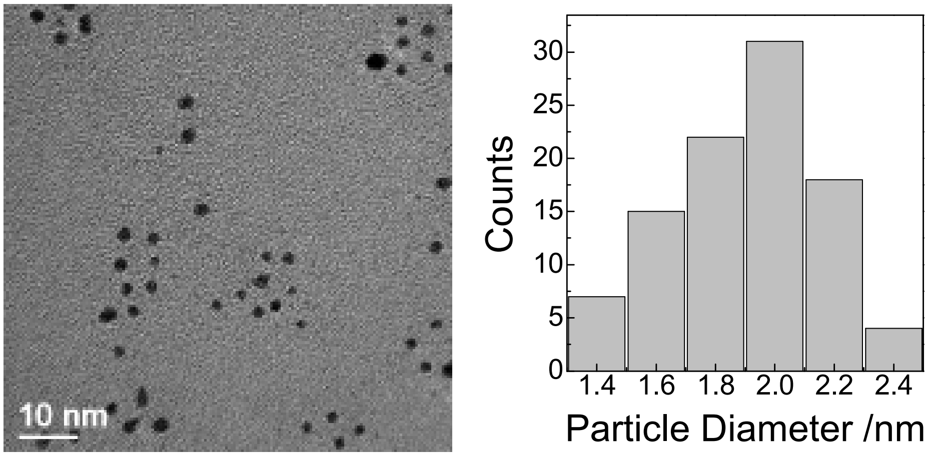

Figure 3.1 Representative TEM image of Pt –DENs. The histogram depicts a typical particle size distribution for the Pt-DENs.

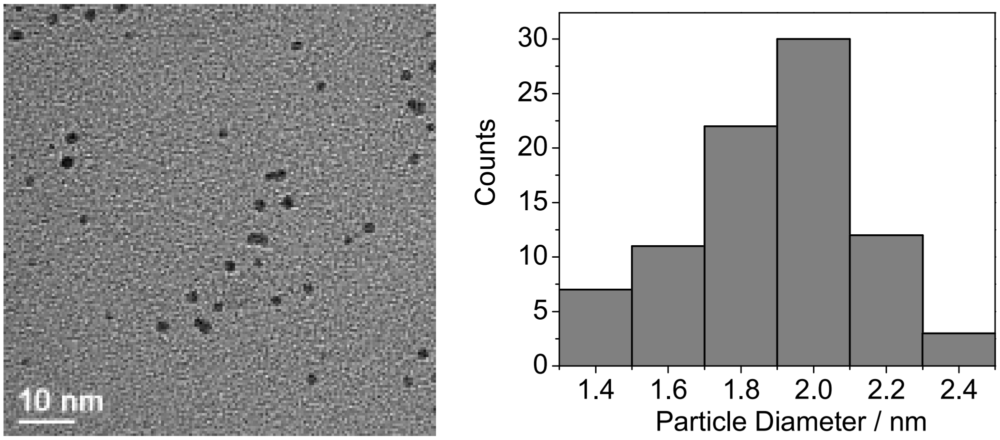

Figure 3.2 Representative TEM image of Pd –DENs. The histogram depicts a typical particle size distribution for the Pd-DENs.

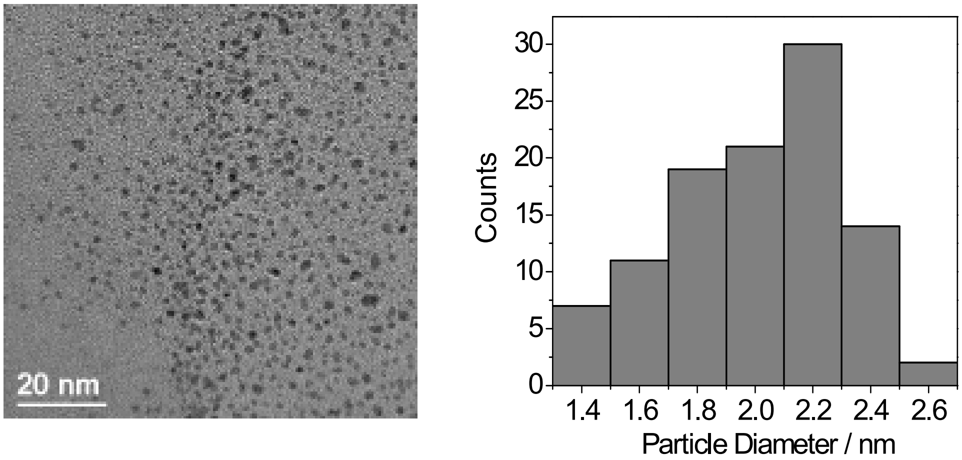

Figure 3.3 Representative TEM image of PdAu –DENs. The histogram depicts a typical particle size distribution for the PdAu-DENs.

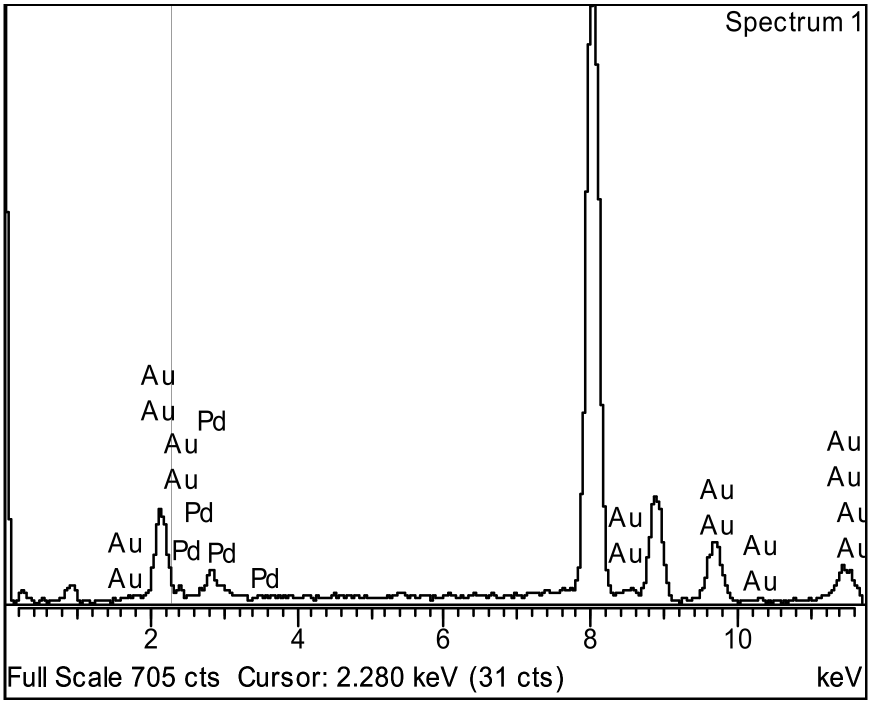

Figure 3.4 Representative energy dispersive spectrum for PdAu- DENs.

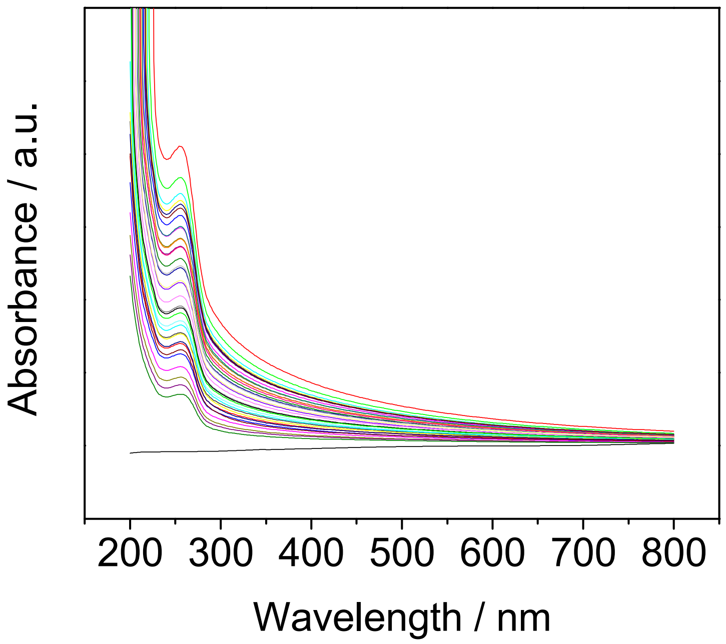

Figure 3.5 UV-Vis spectra showing cumulative adsorption measurements observed over 24 hrs for the adsorption of Pt-DEN on 4 % NCNTs.

absorbance exists over the 24h period. This corresponds to the adsorption of virtually all Pt-DENs from solution on the NCNT surface. The appearance of a broad shoulder at 260 nm has been attributed to the absorbance at unreduced Pt^{2+} that remains bound to the exterior amine groups of the dendrimers.[27] Figure 3.6 shows a picture depicting a visual representation of the Pt-DEN adsorption process. Vial A contained a 20 μM solution of Pt-DENs which were dark brown in color consistent with the presence of colloidal Pt in solution. Vial B contained a 1 mg/ ml of 4 % NCNTs dispersed in the Pt-DEN solution. The NCNTs seem well dispersed in the solution showing no visual evidence of agglomeration. Vial C represents the NCNT/ Pt-DEN solution after 24h of stirring the NCNT/ Pt-DEN solution. The supernatant is transparent, consistent with the adsorption of Pt-DENs from the solution onto the NCNT surface.

The adsorption behavior of the G4-NH_2-terminated Pt-DENs for undoped CNTs, 4 % NCNTs and 7.5 % NCNTs corresponding to different initial bulk Pt-DEN solution concentrations for a 24 h period is shown in Figure 3.7. Adsorption experiments were conducted in triplicate with Pt-DENs in the concentration range of 5-20 μM. For each concentration, there was an increase in the percentage adsorbed with increased immersion time. The extent of uptake of Pt-DEN gradually decreases, finally reaching a limiting value as indicated by the plateau. As discussed in section 3.2.4, UV-Vis data was used to construct adsorption isotherms and estimate adsorption parameters by fitting to a Langmuir based model for the adsorption of Pt-DENs. All of the curves in Figure 3.7 have a similar shape, only differing in the amount of Pt-DEN adsorbed. The adsorption

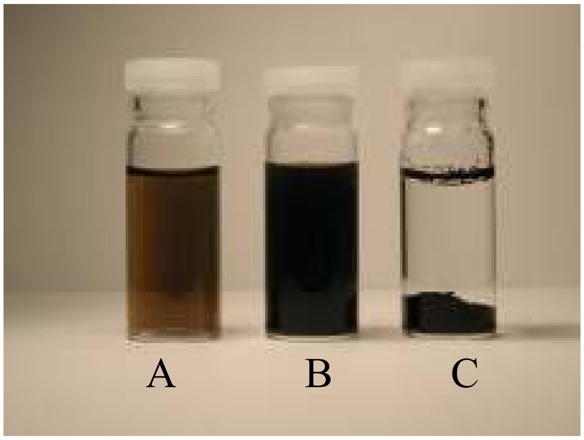

Figure 3.6 Picture representing the Pt-DEN adsorption process on NCNTs. A) 20 μM Pt-DENs. B) Pt-DENs with NCNTs suspended in solution. C) NCNT/ Pt-DEN suspension after 24 hrs showing all DENs having been adsorbed onto the NCNTs rendering the solution colorless.

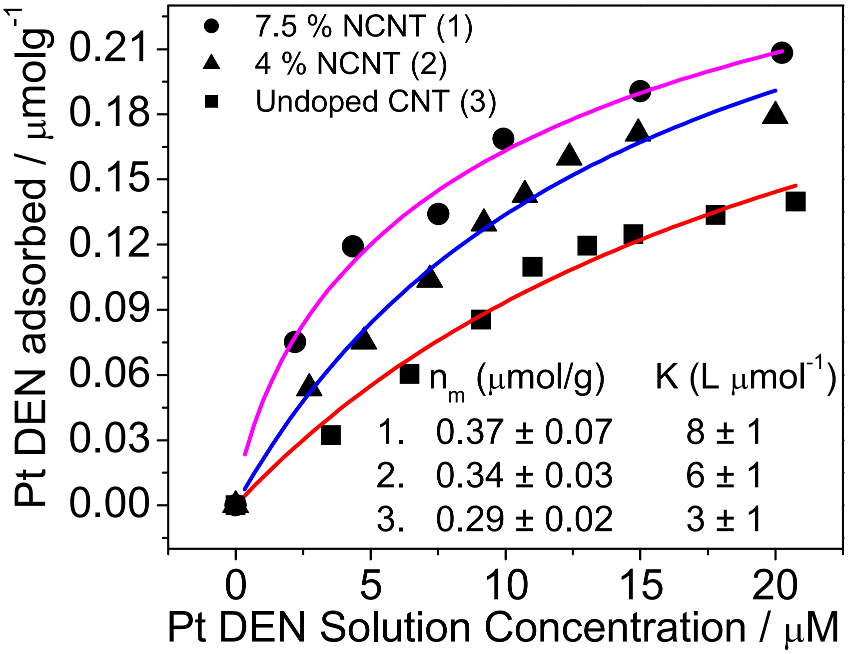

Figure 3.7 Adsorption isotherms for G_4-NH_2 Pt-DEN adsorption on undoped CNT and NCNT supports.

of Pt-DENs onto 7.5 % NCNTs was almost twice as fast as that for undoped CNTs for the same immersion time, especially within the first hour. Adsorption of the Pt-DENs always went to completion for these specific carbons. The solutions were transparent after 24 h, and showed no UV-Vis absorbance between the 250-800 nm range. It should be noted the limited solubility of Pt-DENs in aqueous solution (ca. 20 μM) restricts the range of the adsorption isotherm studies and therefore complete saturation behavior for the adsorption isotherms was not observed. However, trends in the relative characteristics of Pt-DEN adsorption on the various CNT supports are easily discerned.

Pt-DEN adsorption values and adsorption equilibrium constants for 4 % NCNTs, 7.5 % NCNTs and undoped CNT/ Pt-DEN composites calculated from the isotherms are reported in the inset of Figure 3.7. The adsorption of the G4–NH_2 Pt-DENs was attributed to the strong van der Waals interactions [34] with edge plane sites at NCNTs. One of the factors that hinders the adsorption of $–NH_2$ terminated Pt-DENs on the undoped CNTs is the relative difficulty of wetting the CNTs in solution. NCNTs on the other hand are easily wettable due to the presence of positively charged nitrogen groups on the surface and to the existence of more edge plane sites.[18] These observations are supported by Raman spectroscopic studies from Chapter 2 that estimate that 4 % NCNTs have roughly 2.4 times more edge plane sites per unit length compared to the undoped CNTs, which is consistent with the 2.6 times greater adsorption affinity estimated from the Pt-DEN adsorption isotherm data.

Similar studies on the adsorption of aqueous metal ion (Pb^{2+}, Cd^{2+}, Cu^{2+}, Ca^{2+} and Hg^{2+}) species on oxygen and nitrogen functionalized activated carbons conducted by Xiao et al[35] found strong correlations between the concentration of nitrogen groups and metal ion adsorption from solution. While the adsorption mechanism is still a topic of considerable discussion, the Pt-DENs remained anchored to the carbon support and withstood repeated sonication and washings with deionized water. The ability to load catalysts directly from solution onto unmodified NCNTs circumvents a majority of traditional pre-processing steps that modify the carbon and the catalyst and provides advantages in utilizing properties of the pristine carbon and the catalyst.

3.3.3 TEM Analysis of DENs Adsorbed on NCNTs

TEM analysis was performed on the NCNT/ DEN composites to confirm structural and compositional properties of the DENs on the NCNTs. Figure 3.8 shows a representative TEM image of Pt-DENs adsorbed from solution onto 4 % NCNTs. The Pt nanoparticles themselves are stable inside the dendrimer template and appear suspended a few angstroms above the carbon support. It is clear that the DENs are well dispersed throughout the NCNTs and do not show any signs of agglomeration. No evidence of agglomeration was found on undoped CNTs and NCNTs with other nitrogen contents either. The inset in Figure 3.8 shows a high resolution detail of the Pt particles on the NCNT surface. The presence of lattice structures at the Pt nanoparticles shows that they are crystalline. Particle size distributions calculated from the Pt-DENs adsorbed on the NCNTs show that they

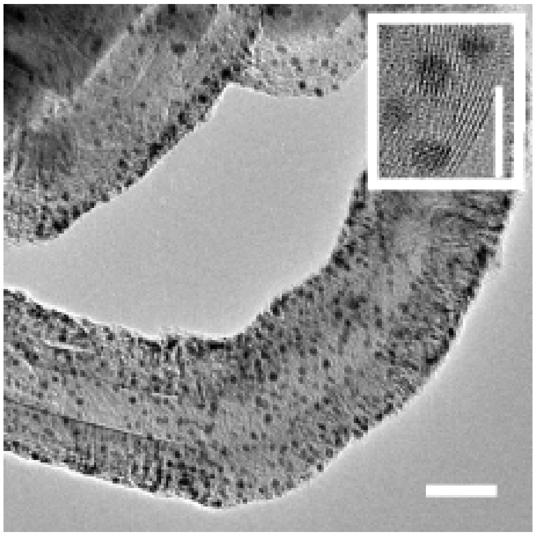

Figure 3.8 TEM image of G4-NH_2 Pt-DENs adsorbed on 4 % NCNT supports (Scale bar is 20nm). The inset shows high resolution structure of Pt nanoparticles (Scale bar is 5nm).

are virtually the same when compared to distributions calculated from as-synthesized particles.

Figure 3.9 shows representative TEM images of Pd and PdAu DENs adsorbed on 4 % NCNTs. The Pd DENs are found to be similarly well dispersed and found to retain the same size as that of the as synthesized DENs. No agglomeration of particles was observed. The PdAu DENs adsorbed on the 4 % NCNTs had similar characteristics as that of the monometallic Pt and Pd-DENs. EDS analysis of the adsorbed PdAu particles showed no changes in the composition. A closer analysis of the left edge at the NCNT in Figure 3.9 B corroborates evidence of the DENs suspended a few angstroms above the NCNTs. Prolonged immersion of the NCNTs in DEN solutions were not found to affect their structure as derived from TEM observations.

3.3.4 Comparison of Adsorption Characteristics of –NH_2 and –OH Terminated DENs

To further elucidate the difference in adsorption and the significance of the terminal –NH_2 groups at the dendrimers, experiments were carried out with G4-OH Pt-DENs in the same concentration range. Pt-DENs synthesized using these different dendrimer varieties were found to have highly comparable particle size distributions. Figure 3.10 shows representative TEM images of Pt DENs adsorbed on 4 % NCNTs from 20 μM solutions of G4-NH_2 Pt-DEN and G4-OH Pt-DENs. While the G4-NH_2 Pt-DENs were well dispersed on the NCNTs, the G4-OH Pt-DENs were found to agglomerate on the surface.

Reduced affinity was also seen for the –OH terminated DENs and was attributed to weaker interactions between the alcohol groups and the carbon

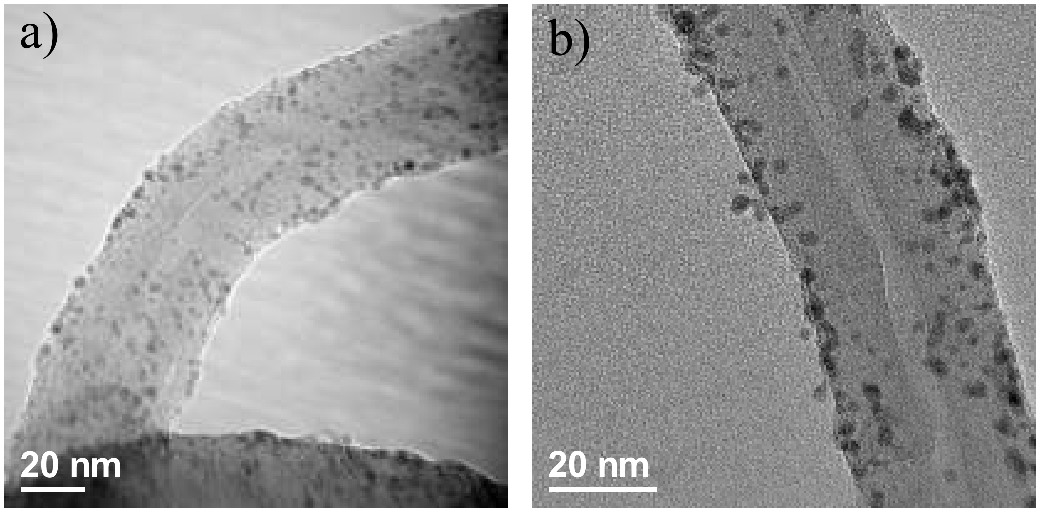

Figure 3.9 TEM images of DENs adsorbed on the NCNT surface. a) Pd DENs adsorbed on 4 % NCNTs. b) PdAu DENs adsorbed on 4 % NCNTs

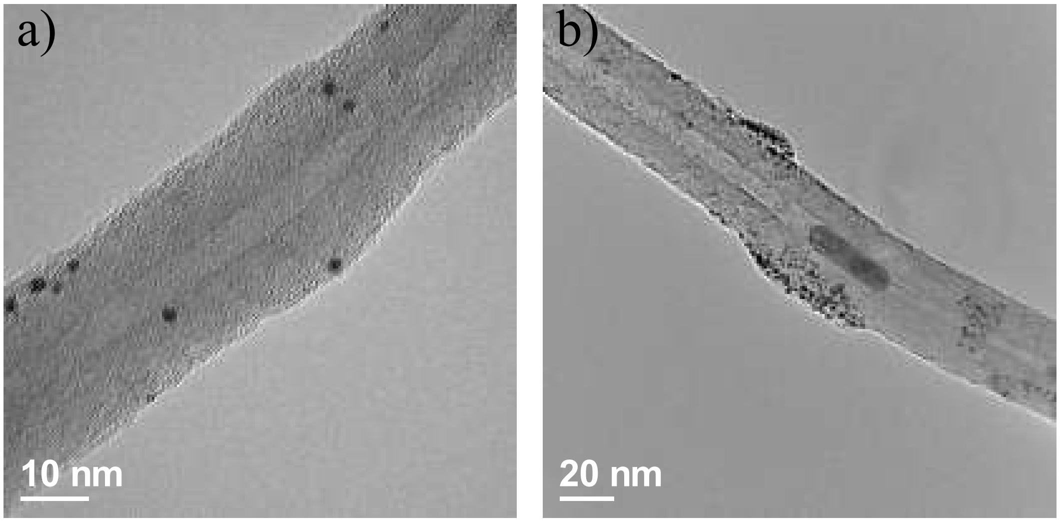

Figure 3.10 Representative TEM images comparing the adsorption of –NH_2 terminated and –OH terminated Pt DENs on 4 % NCNTs. a) G4-NH_2 Pt DENs adsorbed on 4 % NCNTs. b) G4-OH Pt DENs adsorbed on 4 % NCNTs

support. 4 % NCNTs suspended in a 20 μM solution of G4-OH Pt-DEN did not seem to adsorb the Pt-DENs at the same rates as that of the $–NH_2$ terminated Pt-DENs. The supernatant after 24h had significant absorbance at 350 nm consistent with considerable concentration (>40 % of initial concentration) of the G4-OH Pt-DENs left unadsorbed in solution. These observations are consistent with previous reports that G4-NH_2 dendrimers adsorb more strongly than G4-OH dendrimers onto supports including HOPG, gold and glassy carbon.[27,31,34]

3.3.5 Thermo Gravimetric Analysis of Pt DEN loading on NCNTs

Total Pt loadings (wt. %) were quantified by centrifuging undoped CNT/ Pt-DEN and NCNT composites, decanting the supernatant and drying in air prior to TGA analysis. The mass of iron catalyst used for CNT growth (~12 wt. %), was constant for a particular variety of CNTs and was subtracted from the total mass of the residue obtained after each TGA run.

TGA analysis performed on CNT samples with varying immersion times in Pt-DEN solutions enabled control of the Pt loading with respect to immersion times. Figure 3.11 shows TGA heating curves for control 7.5 % NCNT and 7.5 % NCNTs with maximum Pt loadings. Maximum loadings were achieved by replenishing the initial 20 μM Pt-DEN solution with a fresh solution after complete adsorption of the DENs on NCNTs. This solution was allowed to stir until no appreciable change was seen in the absorbance at 350 nm. Pt loadings as high as 26 wt. % were observed using G4-NH_2 terminated Pt-DENs on 7.5% NCNTs after 30 h immersion. In contrast, loadings of only 15 wt. % were

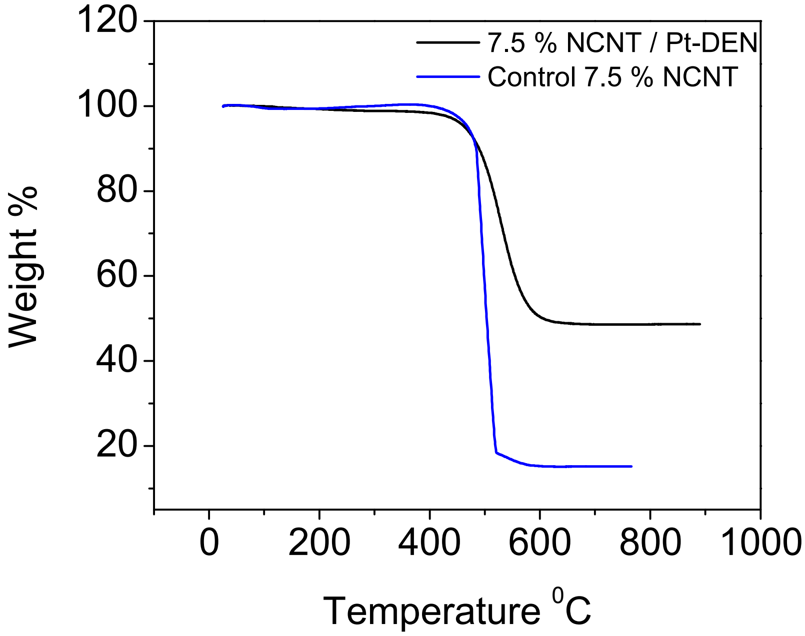

Figure 3.11 Representative TGA heating curves for blank NCNTs and Pt-DENs adsorbed on 7.5 % NCNTs. Mass loading of Pt on NCNTs is calculated by subtracting final wt. % of NCNT/ Pt-DEN from final wt. % at blank NCNT.

achieved using G4-NH_2 Pt-DENs on undoped CNTs and loadings of only ~7 wt. % were achieved using G4-OH Pt-DEN on 7.5% NCNT after 30 h.

These observations are consistent with Raman data (Chapter 2) that estimate higher edge plane content at NCNTs. The presence of a higher number of edge plane sites effects higher adsorption rates and thus a higher mass loading of DENs at the NCNTs as discussed in section 3.3.2.

3.3.6 Electrochemical Analysis of CNT/ DEN Composites

3.3.6.1 Cyclic Voltammetry Studies at CNT/ Pt-DEN Composites

The catalytic activity for ORR of the CNT/ Pt-DEN and NCNT composites was studied using cyclic voltammetry conducted in a standard single compartment three electrode electrochemical cell. To provide a direct basis for comparison, voltammetric studies of CNT/ Pt-DEN and NCNT/ Pt-DEN composites were performed on materials possessing the same Pt loading of 18±1 μg calculated based on a 5 μL aliquot of the composite obtained from a slurry prepared with 1 mg CNT, or 1 mg NCNT, 75 μL of 0.15 wt. % Nafion in anhydrous ethanol and 75 μL of 18 MΩ cm water. The aliquot was then drop cast onto a glassy carbon electrode with a constant geometric surface area. Control studies were also performed on undoped CNTs and NCNTs without Pt-DENs present by casting films in a similar fashion to distinguish the effect of the carbon support on ORR. Importantly, we were able to control the amount of Pt-DEN dispersed on the CNT and NCNT supports by regulating the immersion time. The same slurry preparation procedure was used to prepare a Pt/Vulcan carbon standard composite (Johnson Matthey) with a Pt loading of 20 wt. %.

The peak potential (E_p) corresponding to CV's for ORR at 7.5 % NCNT/ Pt-DEN was 730 mV more positive than the E_p seen for the undoped CNTs at -210 mV as shown in Figure 3.12. This indicates that the Pt-DENs adsorbed on the NCNT surface are in electrical contact with the carbon and are active for ORR. It should be noted that the CV corresponding to ORR at 7.5 % NCNT/ Pt-DEN showed the most positive shift in E_p value for an NCNT/ Pt-DEN composite. Electroactive surface areas (ESAs) for the undoped CNT and NCNT/ Pt-DEN composites were assessed by integration of the amount of charge associated with the hydrogen adsorption on the Pt-DEN catalysts. The ESAs were 17.1 m^2g^{-1} for undoped CNT/ Pt-DEN, 20.6 m^2g^{-1} for 4 % NCNT/ Pt-DEN and 24.9 m^2g^{-1} for 7.5 % NCNT/ Pt-DEN as shown in Table 3.1. Comparative analysis of the surface area at the control CNTs and the ESA's corresponding to adsorbed Pt at the CNTs does not show correlations between those parameters consistent with findings discussed in Chapter 2.

3.3.6.2 Rotating Disk Electrode Studies

Figure 3.13 displays ORR polarization curves for undoped CNT/ Pt-DEN and various NCNT/ Pt-DEN composites in O_2-saturated 0.1 M H_2SO_4 obtained using an RDE at 1600 RPM.[33] The performance of the as prepared CNT/ Pt-DEN composites is consistent with previous voltammetry and RDE studies of Pt-DENs immobilized on glassy carbon electrodes.[36,37,38] However, the activity of Pt-DENs supported on NCNT supports is higher than Pt-DENs supported on undoped CNTs. Furthermore, the onset potential for ORR and activity of Pt-DENs supported on NCNTs tracks with the amount of incorporated nitrogen, as

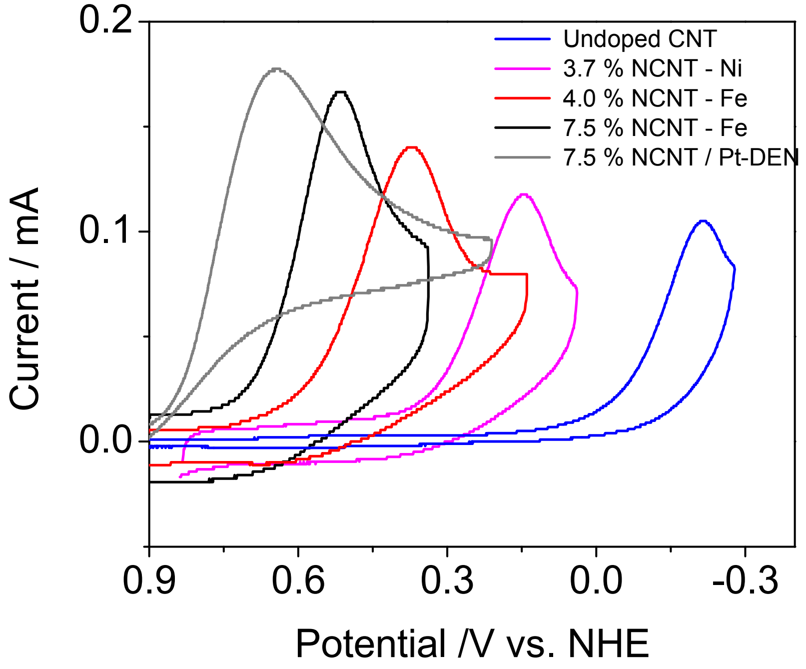

Figure 3.12 Cyclic voltammograms for ORR at control undoped CNTs and NCNTs synthesized using Fe and Ni precursors compared to NCNT/ Pt-DEN composites in oxygen saturated 0.1 M H_2SO_4. ν = 20 mVs^{-1}.

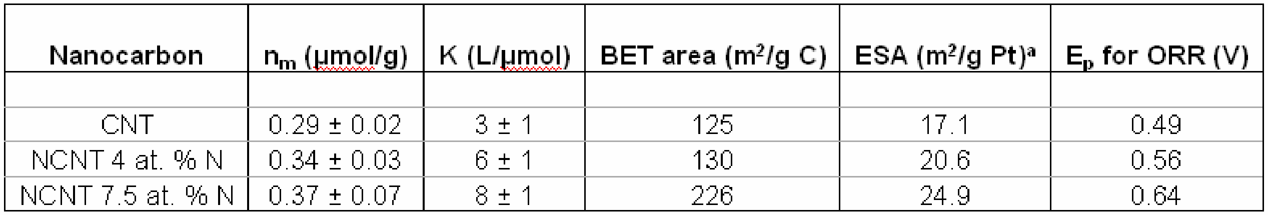

Nanocarbon	n_m (µmol/g)	K (L/µmol)	BET area (m^2/g C)	ESA (m^2/g Pt)[a]	E_p for ORR (V)
CNT	0.29 ± 0.02	3 ± 1	125	17.1	0.49
NCNT 4 at. % N	0.34 ± 0.03	6 ± 1	130	20.6	0.56
NCNT 7.5 at. % N	0.37 ± 0.07	8 ± 1	226	24.9	0.64

Table 3.1 Comparison of Pt-DEN adsorption parameters, BET surface area, electroactive surface area and E_p for ORR at undoped CNT/ Pt-DEN, and NCNT/ Pt-DEN composites for 4 % NCNTs and 7.5 % NCNTs.

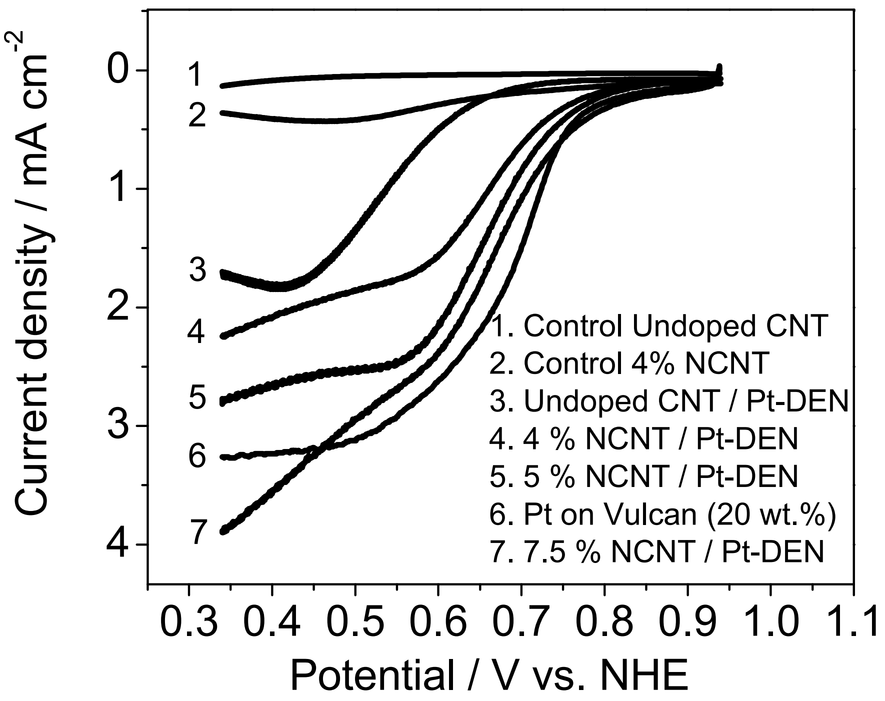

Figure 3.13 Polarization curves for the ORR on G_4-NH_2 Pt-DEN/CNT and NCNT composites supported on a glassy carbon electrode immersed in an O_2 saturated 0.1M H_2SO_4 solution. In all cases the Pt loading is 18±1 μg. Also shown are polarization curves for CNT and NCNT supports. Rotation rate =1600 rpm, scan rate =20 mV s^{-1}.

illustrated in Figure 3.13 for Pt-DENs supported on 4 %, 5 % and 7.5 % NCNTs. We attribute the increase in catalytic activity at NCNTs to an improved carbon-catalyst binding and increased electrical conductivity and also hypothesize that a synergistic support effect is present with the NCNTs as they are known to decompose reactive intermediates such as hydrogen peroxide into oxygen during ORR.[18] Furthermore, the mass transport limited current densities and mass activities (estimated from RDE curves at +350 mV) for 7.5 % NCNT/ Pt-DEN composites were 2.3 mA cm^{-2} and 0.05 mA g^{-1}, respectively. These values are on par with reported values of 3.4 mA cm^{-2} and 0.085 mA g^{-1} for conventional Pt catalysts in the 2 nm size range.[36] The quasi ideal electrocatalytic response for NCNT/ Pt-DEN composites is attributed to improved mass transport and electronic interactions of the Pt-DENs with the NCNT support. Clearly the CV and RDE studies indicate that the Pt-DENs are catalytically active and function as active centers for ORR.

3.4 CONCLUSIONS

In summary, a facile method for preparing catalytically active carbon supported Pt catalysts is demonstrated. The choice of the PAMAM G4-NH_2 dendrimer template and terminal amine functional groups provides for uniform preparation of size monodisperse catalysts and facilitates the controlled dispersion and loading of the catalysts onto NCNT supports with well controlled structural and compositional properties. The immersion based loading of catalysts onto a carbon support by spontaneous adsorption to achieve specific Pt loadings offers a less aggressive processing approach for preparing carbon supported catalysts compared to the harsher catalyst dispersion and loading methods that generally require oxidative treatment of the carbon support and/or chemical reduction of metal salts to achieve selective binding of the active metal catalyst. Additionally, the Pt-DENs and NCNTs serve as well defined models whose properties can be controlled synergistically to achieve better performance at these composites as depicted in Scheme 3.2. A synergistic activity is envisioned where the NCNT support is reactive and serves to reduce the peroxide formed as a byproduct during oxygen reduction at the metal catalyst. Studies of this nature will foster better understanding of role of the carbon support on catalytic efficiency, catalyst utilization and catalyst stability.

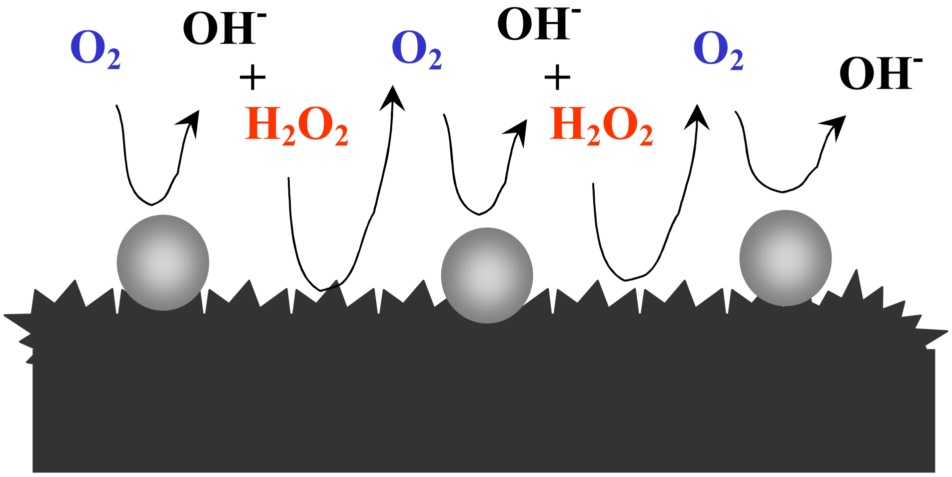

Scheme 3.2 Representation of synergistic ORR activity envisioned at NCNT/ Pt-DEN composites.

3.5 REFERENCES

1. Radovic, L. R.; Rodriguez-Reinoso, F. In *Chemistry and Physics of Carbon*; Thrower, P. A. Ed. Marcel Dekker, 1997, Vol. 25, p 243-358.
2. Wildgoose, G. G.; Banks C. E.; Compton, R. G. *Small* **2006**, *2*, 182.
3. Wang, J.; Musameh, M.; Lin, Y. *J. Am. Chem. Soc*. **2003**, *125*, 2408.
4. Tian, Z. Q.; Jiang, S. P.; Liang, Y. M.; Shen, P. K. *J. Phys. Chem. B.* **2006**, *110*, 5343.
5. Gaur, V.; Sharma, A.; Verma, N. *Carbon* **2005**, *42*, 3041.
6. Li, X.; Hsing, I. -M. *Electrochim. Acta* **2006**, *51*, 5250.
7. Yoon, B.; Wai, C. M. *J. Am. Chem. Soc.* **2005**, *127*, 17174.
8. Xing, Y. *J. Phys. Chem. B* **2004**, *108*, 19255.
9. Serp, P.; Hierso, J. C.; Feurer, R.; Kihn, Y.; Kalck, P.; Faria, J. L.; Aksoylu, A. E.; Pacheco, A. M.; Figueiredo, J. L. *Carbon* **1999**, *37*, 527.
10. Ijima, S. *Nature* **1991**, *354*, 56.
11. Dai, H. *Surface Sci.* **2002**, *500*, 218.
12. Li, W.; Liang, C.; Zhou, W.; Qiu, J.; Zhou, Z.; Sun, G.; Xin, Q. *J. Phys. Chem. B* **2003**, *107*, 6292.
13. Thess, A.; Lee, R.; Nikolaev, P.; Dai, H.; Petit, P.; Robet, J.; Xu, C.; Lee, Y. H.; Kim, S. G.; Rinzler, A.; Colbert, D. T.; Scuseria, D.; Tomanek, J. E.; Fischer, J. E.; Smalley, R. *Science*, **1996**, *273*, 483.
14. Serp, P.; Corrias, M.; Kalck, P. *Appl. Catal. A: Gen.* **2003**, *253*, 337.
15. Ebbesen, T. W. *J. Phys. Chem. Solids* **1996**, *57*, 951.
16. Lordi, V.; Yao, N.; Wei, J. *Chem. Mater.* **1998**, *10*, 718.
17. Yu, R.; Chen, L.; Liu, Q.; Lin, J.; Tan, K. –L.; Ng, S. C.; Chan, H. S. O.; Xu, G. –Q.; Hor, T. S. A. *Chem. Mater.* **1998**, *10*, 718.
18. Maldonado, S.; Stevenson, K. J. *J. Phys. Chem. B* **2005**, *109*, 4707.

19. Maldonado, S.; Morin, S.; Stevenson, K. J. *Carbon* **2006**, *44*, 1429.

20. Scott, R. W. J.; Wilson, O. M.; Crooks, R. M. *J. Phys. Chem. B* **2005**, *109*, 692.

21. Hirsch, A. *Angew. Chem., Int. Ed.* **2002**, *41*, 1853.

22. Guldi, D. M.; Rahman, G. M. A.; Zerbetto, F.; Prato, M. *Acc. Chem. Res.* **2005**, *38*, 871.

23. Niu, Y.; Crooks, R. M. *C. R. Chimie* **2003**, *6*, 1049.

24. Planeix, J. M.; Coustel, N.; Coq, B.; Brotons, V.; Kumbhar, P. S.; Dutartre, R.; Geneste, P.; Bernier, P.; Ajayan, P. M. *J. Am. Chem. Soc.* **1994**, *116*, 7935.

25. Li, W.; Liang, C.; Qiu, J.; Zhou, W.; Han, H.; Wei, Z.; Sun, G.; Xin, Q. *Carbon* **2002**, *40*, 787.

26. Satishkumar, B. C.; Vogl, E. M.; Govindaraj, A.; Rao, C. N. R. *J. Phys. D: Appl. Phys.* **1996**, *29*, 3173.

27. Ye, H.; Scott, R. W. J.; Crooks, R. M. *Langmuir* **2004**, *20*, 2915.

28. Zhao, M.; Crooks, R. M. *Angew. Chem., Int. Ed.* **1999**, *38*, 364.

29. Zhao, M.; Crooks, R. M. *Adv. Mater.* **1999**, *11*, 217.

30. Scott, R. W. J.; Ye, H.; Henriquez, R. R.; Crooks, R. M. *Chem. Mater.* **2003**, *15*, 3873.

31. Scott, R. W. J.; Wilson, O. M.; Oh, S. –K.; Kenik, E. A.; Crooks, R. M. *J. Am. Chem. Soc.* **2004**, *126*, 15583.

32. Vijayaraghavan, G.; Stevenson, K. J. *Langmuir* **2007**, *23*, 5279.

33. Schmidt, J.; Gasteiger, H. A; Stab, G. D.; Urban, P. M.; Kolb, D. M.; Behm, R. J. *J. Electrochem. Soc.* **1998**, *145*, 2354.

34. Sun, L.; Crooks, R. M. *Langmuir* **2002**, *18*, 8231.

35. Xiao, B.; Thomas, K. M. *Langmuir* **2005**, *21*, 3892.

36. Gasteiger, H. A.; Kocha, S. S.; Sompalli, B.; Wagner, F. T. *Appl. Catal. B* **2005**, *56*, 9.

37. Paulus, U. A.; Schmidt, T. J.; Gasteiger, H. A.; Behm, R. J. *J. Electroanal. Chem.* **2001**, *495*, 134.

38. Mayrhofer, K. J. J.; Blizanac, B. B.; Arenz, M.; Stamenkovic, V. R.; Ross, P. N.; Markovic, N. M. *J. Phys. Chem. B* **2005**, *109*, 14433.

CHAPTER 4

Metal Organic Chemical Vapor Deposition of Nanocarbon Supported Mono- and Bimetallic Catalysts for Oxygen Reduction

4.1 INTRODUCTION

The efficiency and utilization of heterogeneous catalysts is directly dependant on the synthetic protocols involved in the loading and subsequent activation of the catalyst. These steps are typically refined to optimize size, composition, dispersion and surface area of the catalyst on the carbon support. While a host of liquid phase methods like microemulsion[1] and impregnation[2] are used to deposit noble metal catalysts on carbon supports, they typically require harsh chemical or physical processing steps of the carbon support to facilitate catalyst loading and dispersion. Typical procedures used for activating carbon supports and creating surface oxygen functionalities use strong acids[3] such as HNO_3 or H_2SO_4 or strong oxidizing agents.[4] These methods alter the intrinsic properties of the support and tend to be variable and time consuming processes. The use of the above mentioned procedures can also hinder understanding of the role of the carbon support properties on specific catalytic activity. To this end, we have been studying the specific role of nitrogen doped carbon nanotube (NCNT) supports in technologically important reactions such as ORR as dealt with in Chapter 2. Previous reports from the Stevenson research group have demonstrated that NCNTs show inherent catalytic activity for both ORR and the heterogeneous decomposition of hydrogen peroxide.[5, 6] While as grown NCNTs are less active than Pt supported on carbon supports, we speculate that they promote a catalytic synergism by scavenging intermediates from ORR such as hydrogen peroxide.[5] The removal of these reactive intermediates is a key step in improving the catalytic activity of a support/ catalyst combination and also leads to supports that are better resistive to corrosion[7] over extended periods. These properties of the NCNTs has been taken advantage of in previous studies that pair these supports with catalysts synthesized using dendrimer templates,[8] as discussed in Chapter 3. Although the NCNT/ dendrimer composites were active catalysts, their electrochemical surface areas were lower compared to commercial catalysts. The cost of the dendrimer templates also hinders commercialization aspects of this particular scheme for preparing templated nanoparticles and alternate routes are necessary to prepare cost effective active carbon/ catalyst composites.

Literature reports have dealt with the surface selective nature of CVD for a variety of metals such Pt[9], Pd[9], Rh[10] and Ag[11] using metal organic chemical vapor deposition (MOCVD) precursors. The influence of surface area, porosity and the presence of anchoring sites at specific supports on the preparation of supported catalysts using MOCVD routes have also been discussed.[12] A number of different techniques have been employed to effect the CVD process and a few hypotheses exist as to the nucleation and growth mechanism. Nuzzo et al. have performed extensive studies on the CVD of hexafluoroacetylacetonate metal precursors on various substrates and have proposed a fairly comprehensive mechanism.[13,14] A combination of XPS, RAIRS and TPD studies on the CVD of bis(hexafluoroacetylacetonate)-palladium(II) Pd(hfac)$_2$ on a copper surface has shown that this process involved several principal steps. The first was the adsorption of Pd(hfac)$_2$ molecules on the Cu surface at the appropriate sublimation temperatures. The second step involved the reduction of Pd^{II} to Pd^0 by the Cu surface. Processes that involve CVD on a non metallic surface have effected this step by employing a reductive gas such as H_2 during the deposition.[15,16] The use of a reductive gas flow or a reductive surface, results in the dissociation of the hfac ligands from the Pd that constitutes the third step. The hfac ligands were seen to react with the surface Cu to form Cu(hfac)$_2$ which was then desorbed from the surface. In the case of CVD at a non metallic surface, the decomposition and removal of the precursor ligands was seen to be facilitated by the H_2 gas during reduction of the metal.

A majority of the CVD processes are applied for the deposition of thin films on relatively smooth surfaces.[17] Deposition of particles through CVD has been typically nucleated by the creation of aberrations and induction of specific functionalities on the surface of the support by aggressive processes as discussed in the preceding paragraphs. Several groups have studied the dependence of the nucleation rate of metals on the nature of the support and have agreed in principle that surfaces customized with specific composition and structure can be used to control the nucleation step of CVD facilitating tailored growth of nanoparticles.[13,16]

Traditional CVD processes employed towards the deposition of nanoparticle catalysts on a carbon support utilize a fluidized bed.[18,19] Fluidized bed processes use a gas stream flowing from the bottom of a reactor to suspend highly functionalized carbon supports in the deposition zone. This enables better interaction of the precursor with the carbon in the deposition zone resulting in a fairly uniform dispersion of the metallic nanoparticles on the carbon surface.

The ability to manipulate *in-situ*,[5,6] the structure, composition, surface area and the amount of edge plane sites on NCNTs provides a significant advantage over traditional carbons for use as supports in the CVD scheme because there is no further need to modify the surface to facilitate catalyst loading. The capability to synthesize NCNTs with a remarkable degree of alignment and uniformity on a variety of substrates facilitates the direct deposition of metal nanoparticles. Substrates with the as synthesized NCNTs can then be directly exposed to the CVD precursors for controlled and uniform nanoparticle growth without necessitation of a fluidized bed reactor.

The attractive properties of NCNTs along with the ease of tailoring and availability of a variety of catalyst precursors used in MOCVD provides significant advantages over other schemes for direct synthesis of support/ catalyst combinations without extensive pre- and post processing steps. Since MOCVD precursors can serve as sources for both the synthesis of the carbon support and the ORR metal catalyst, it should be possible to create active catalysts directly on high-surface area carbons in fewer processing steps. This chapter details the loading of monodisperse Pt, Pd and PtPd catalysts in a subsequent step after the synthesis of NCNTs. However, it is also possible to synthesize carbon/ catalyst combinations from a single precursor source- a topic that is currently being explored at the Stevenson research lab. The MOCVD route offers promise for the direct dispersion and activation of mono- and multimetallic ORR catalysts on carbon supports and eliminates the current inevitable problems involving loading, sintering and activation steps associated with traditional solvent based catalyst preparation schemes.

While this chapter discusses the synthesis aspects of monometallic Pt, Pd and bimetallic PtPd nanoparticles on nanocarbons in detail, emphasis is placed on the characterization of the bimetallic PtPd catalysts. Although Pt catalysts show high activity for ORR, their performance decreases over time due to the formation of Pt-OH[20] that inhibits adsorption and reduction of oxygen on the catalyst surface. Recent studies by the Adzic group[20] conducted on carbon supported monometallic Pt (Pt/C) and bimetallic PtAu (PtAu/C) have shown that the Pt/C catalyst loses over 45 % of its electroactive surface area after 30,000 cycles (0 – 1.2 V vs. NHE) in oxygen saturated 0.1 M $HClO_4$. Under the same experimental conditions the bimetallic PtAu/C retained its original electroactive surface area. Adzic et al attributed the stability of the PtAu bimetallic catalyst to the decreased oxidation of the Pt nanoparticles covered by the Au surface. Multimetallic Pt catalysts with synergistic components that help prevent oxide formation on Pt are of vital importance in improving ORR efficiency.

4.2 Experimental

4.2.1 Synthesis of Undoped CNTs and NCNTs

CNTs were prepared using the floating catalyst chemical vapor deposition method[5,6] described in chapter 2. Briefly, xylene (Aldrich) as carbon source and ferrocene (Aldrich) as catalyst were used for the growth of the undoped CNTs while a pyridine (Fisher) and ferrocene precursor combination was used for the synthesis of nitrogen-doped CNTs. The use of a pyridine precursor allowed for a controlled doping of ~ 4 at. % N on the NCNT surface. Higher surface nitrogen concentrations (5-10 at. % N) were obtained by introducing a regulated stream of ammonia gas (Aldrich) into the CVD furnace system along with the pyridine and ferrocene precursors.

4.2.2 CVD of Mono- and Bimetallic Nanoparticles on CNTs

Monometallic Pt, Pd and bimetallic PtPd catalyst nanoparticles were directly deposited via CVD in a sequential step on the as grown CNTs using thermally labile precursors. Once the synthesis step for a particular variety of the CNTs was completed, a carefully measured mass of $Pt(acac)_2$ or $Pd(acac)_2$ (Alfa Aesar, 99.9%) was weighed and placed in a ceramic boat in zone 1 of the furnace for deposition of Pt or Pd nanoparticles respectively. While the gas flow stream comprised of 400 sccm Ar and 70 sccm H_2, zone 1 was maintained at 170 $^{\circ}$C (190 $^{\circ}$C for Pd) and zone 2 was maintained at 220 $^{\circ}$C for sublimation and subsequent decomposition respectively of the Pt or Pd catalysts on the CNTs. The sublimation and decomposition process spanned a 20 minute period and a dark organic mass was left in the ceramic boat. After the furnaces were allowed to cool to room temperature, the catalysts were retrieved from the interior of the quartz tube and stored in airtight vials prior to characterization.

In the case of bimetallic PtPd nanoparticles, a 50:50 mass ratio of $Pt(acac)_2$ and $Pd(acac)_2$ was weighed and placed in a ceramic boat at zone 1 of the furnace system. The carrier gas stream consisted of 400 sccm Ar and 70 sccm H_2. Zone 1 was maintained at 190 °C and zone 2 at 220 °C for sublimation and decomposition respectively of the catalyst precursors.

4.2.3 Electron Microscopy

Transmission electron microscopy (TEM) characterization of the CNT supported catalysts was performed on a JEOL 2010F microscope operating at 200 kV. Energy dispersive spectroscopy was performed on an Oxford instruments INCA detector that was part of the TEM instrumentation. TEM samples were prepared by dispersing the catalysts in anhydrous ethanol and drop casting on a Cu TEM grid covered with lacey carbon film.

4.2.4 Raman Characterization

A Renishaw inVia system equipped with a 514.5 nm Ar laser at 3 mW/cm^2 and 100X aperture was used. Spectra were scan averaged for 300 s. Bands at 1220, 1351, 1487, 1583 and 1624 cm^{-1} corresponding to I, D, D″, G, and D′ bands denoted by Cuesta et al[13] were fit using a Peak Fit 4 software package to correlation factors greater than 0.998. A linear baseline correction was used to compensate for photoluminescence background.

4.2.5 X-Ray Photoelectron Spectroscopy Characterization

X-ray photoelectron spectroscopy characterization of the samples was performed using a PHI 5700 ESCA system operating at a scan step size of 0.1 eV and an Al Kα monochromatic line (1486.6 eV) calibrated with Au $4f_{7/2}$, Ag $3d_{5/2}$ and Cu $2p_{3/2}$ signals. All spectra were scan averaged 5 times. Atomic percentages were quantified from survey scans relative to carbon, iron and nitrogen. FITT 1.2 (Photoelectron Spectroscopy lab, Seoul National University) software with Shirley background corrections was used to analyze the spectra.

4.2.6 Thermo Gravimetric Analysis

Thermo gravimetric analysis (TGA) was performed using a Perkin Elmer 7000 analyzer. Samples (~5 mg) were held in platinum pans heated to 800 °C at 5 °C / min in flowing air (Praxair, 99.998%).

4.2.7 Electrochemical Analysis

Electrochemical measurements were carried out on a EG&G Instruments 263A potentiostat equipped with a Pine Instruments MSRX controller for rotating disk electrode (RDE) measurements. Data acquisition and analysis was performed on a Corrware (Scribner Associates) software package. Sample slurries prepared with 0.15 wt. % nafion in anhydrous ethanol and de-ionized water were drop cast as a film on a glassy carbon RDE (0.5 cm diameter, Pine Instruments) polished to a mirror finish and allowed to dry under a stream of Ar (Praxair 99.98%) prior to electrochemical measurements. Cyclic voltammograms were obtained in a standard three electrode cell with a gold counter electrode and a Hg/Hg_2SO_4 reference electrode in O_2 (Praxair) saturated 0.1 M H_2SO_4 prepared with deionized water (>18 MΩ cm). All potentials were converted to NHE for comparison to literature values. For electro-active surface area measurements, CO (Praxair) was dosed into the electrolyte solution for 20 min while the electrode was held at a constant potential and the solution then purged with Ar for 30 min to remove CO from the bulk.

Prior to oxygen reduction and CO stripping experiments, the CNT/catalyst film was cycled between 0.8 and -0.2V in order to make the film hydrophilic and achieve steady state voltammograms.

Chronoamperometry experiments were carried out in CO saturated 0.1 M H_2SO_4. CO was dosed into the electrolyte for 10 min while the electrode was held at 0.11V. CO in bulk was purged by bubbling in a stream of Ar for 20 min. Electrode potentials were subsequently stepped up and chronoamperometric transients recorded on a 30 S time scale.

4.3 RESULTS AND DISCUSSION

4.3.1 Morphological Properties of Catalysts Synthesized by MOCVD

The surface interaction between a catalyst precursor and the carbon support is important in the synthesis of carbon supported catalysts through chemical vapor deposition.[12] The choice of specific precursors, the composition and flow rate of the feed gas stream highly influences the size, crystallinity, structure and composition of the catalyst particle. The presence of a reducing agent such as hydrogen[21] in the feed stream greatly reduces the deposition of free carbon contaminations from the metal organic precursor that significantly decreases the available surface area of the metal. The introduction of the catalyst precursor into zone 1 of the furnace after the synthesis of CNTs in zone 2 was carefully controlled and the quartz tube purged with Ar for 30 minutes to remove trace oxygen. The presence of oxygen could lead to the formation of oxygen functionalities on the surface of the CNT support, affect efficient decomposition of the precursor and the electrochemical performance of the catalyst composite. Initial experiments with the sublimation and decomposition of $PtMe_2(COD)$ on CNT supports left substantial amounts of carbon impurities[22] on the surface of the CNT/catalyst composites. While the amount of carbon impurities was reduced using appropriate flow rates of hydrogen in the feed stream, the particle sizes were found to vary over a wide range (15-30 nm) and were not evenly distributed.

The use of $Pt(acac)_2$ and $Pd(acac)_2$ precursors allowed for a narrower size distribution and smaller particle sizes compared to the $PtMe_2(COD)$ precursor used for the Pt source. Figure 4.1 shows TEM images of Pt and Pd catalysts directly deposited on NCNT supports without additional processing or post activation steps. As shown in Figure 4.1a and the corresponding particle size histogram in Figure 4.1b the Pt nanoparticles are fairly monodisperse with an average diameter of 2.1 nm and appear to be dispersed uniformly over the NCNT support. The Pt catalysts also appear to be strongly anchored with the NCNT support and withstand repeated washing and sonication steps. In comparison Pd catalysts prepared using a Pd(acac)$_2$ precursor under similar conditions were of a larger average particle size of 11.8 nm (Figure 4.1c and 4.1d).

Figure 4.2 shows a representative TEM image and the particle size distribution of PtPd on 6.5 % NCNTs. Literature data[12,21] suggest that the carbon impurities from the precursor constitute less than 1% of the total mass consistent with TEM observations. The inset in Figure 4.2 shows that PtPd bimetallic particles deposited on 6.5% NCNTs were crystalline with an average particle size of 3.1 nm. The graphitic nature of the carbon substrate is also clearly represented. Overall the particles were fairly monodisperse with no evidence of agglomerations. Average particle size and particle size distributions were calculated from a total of at least 100 particles measured across three different batches. The energy dispersive spectrum (Figure 4.2c) of single PtPd bimetallic particles averaged across at least three different samples shows that the particles consist of 62 ± 2 % Pt and 38 ± 3 % Pd.

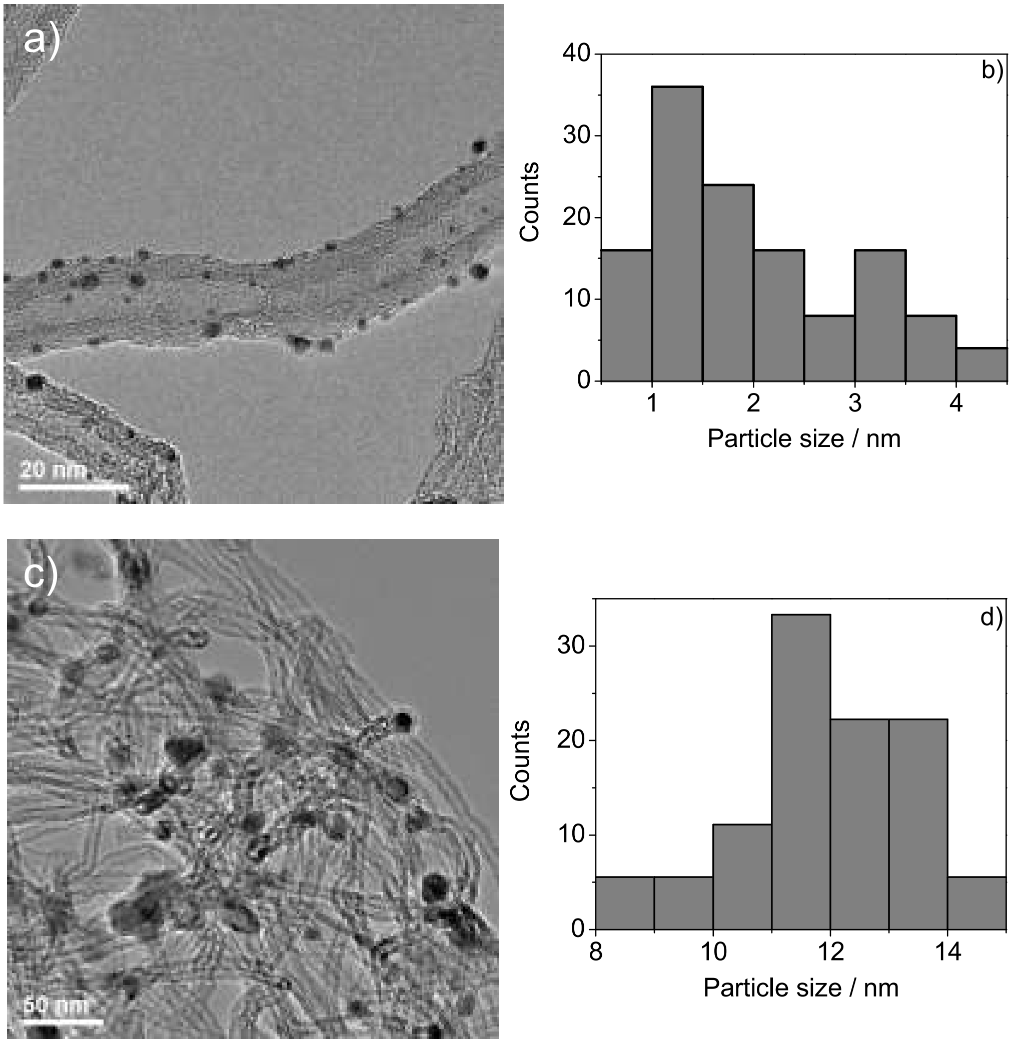

Figure 4.1 TEM images of a) Pt and c) Pd catalysts on NCNT supports. Corresponding particle size histograms for b) Pt and d) Pd catalysts.

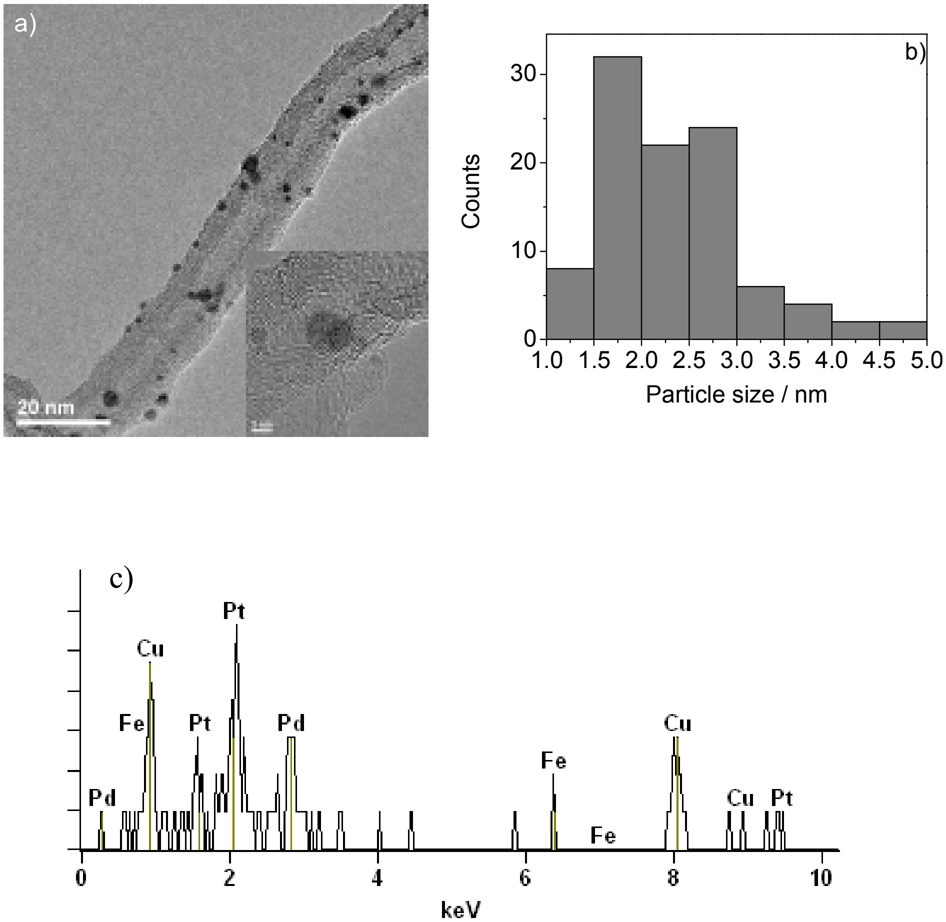

Figure 4.2 TEM image of a) PtPd particles on 6.5 % NCNT supports. Inset shows high resolution image of a PtPd bimetallic catalyst particle. b) Corresponding particle size histogram for PtPd catalysts. c) Representative energy dispersive spectrum of a single PtPd nanoparticle.

4.3.2 Raman Analysis

First order Raman spectra of the catalysts supported on different varieties of CNTs (Figure 4.3) were collected primarily to quantify and ensure that the amount of edge plane sites on the CNT supports loaded with catalysts was comparable to that of the pristine CNT varieties thereby minimizing ambiguity on other factors that might influence catalyst loading. The amount of disorder on each of the CNT supports were measured by fitting and integrating the intensities of the D and G bands over an average of three different batches as shown by Cuesta et al.[23] $1/ L_a$ values calculated for undoped CNTs, 4 % NCNTs and 6.5 % NCNTs loaded with PtPd were 0.12, 0.3 and 0.52 nm^{-1} respectively and were agreement to reported values. Raman analysis was found to be an accurate indicator of the amount of edge plane content in the CNTs.

4.3.3 XPS Analysis

Figure 4.4a shows a representative XPS survey spectrum of the PtPd catalysts on 6.5% NCNT. The carbon peak at 284.7 eV is close to values reported earlier.[5, 24] It should be noted that there are no remarkable peaks in the 286-289 eV shoulder region that indicate a significant presence of oxygen like functionalities on the surface of the NCNTs, which lends credence to reasoning that these groups do not influence the deposition of catalysts on the NCNTs. High resolution spectra of the Pt and Pd regions are shown in Figure 4.4b and 4.4c respectively. The Pt 4f region shows doublets arising from the spin-orbital splitting of the $4f_{7/2}$ and the $4f_{3/2}$ states. Peaks at 71 and 74.5 eV are attributed to metallic Pt (Pt(0)). The Pd region shows peaks at 335 and 341 eV that have been

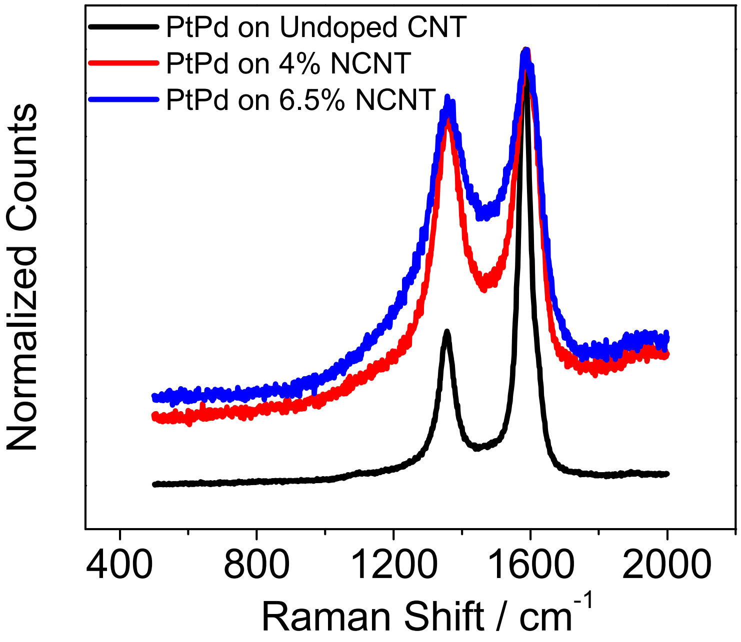

Figure 4.3 Raman spectra of PtPd bimetallic catalysts on NCNT supports with varying surface concentrations of nitrogen.

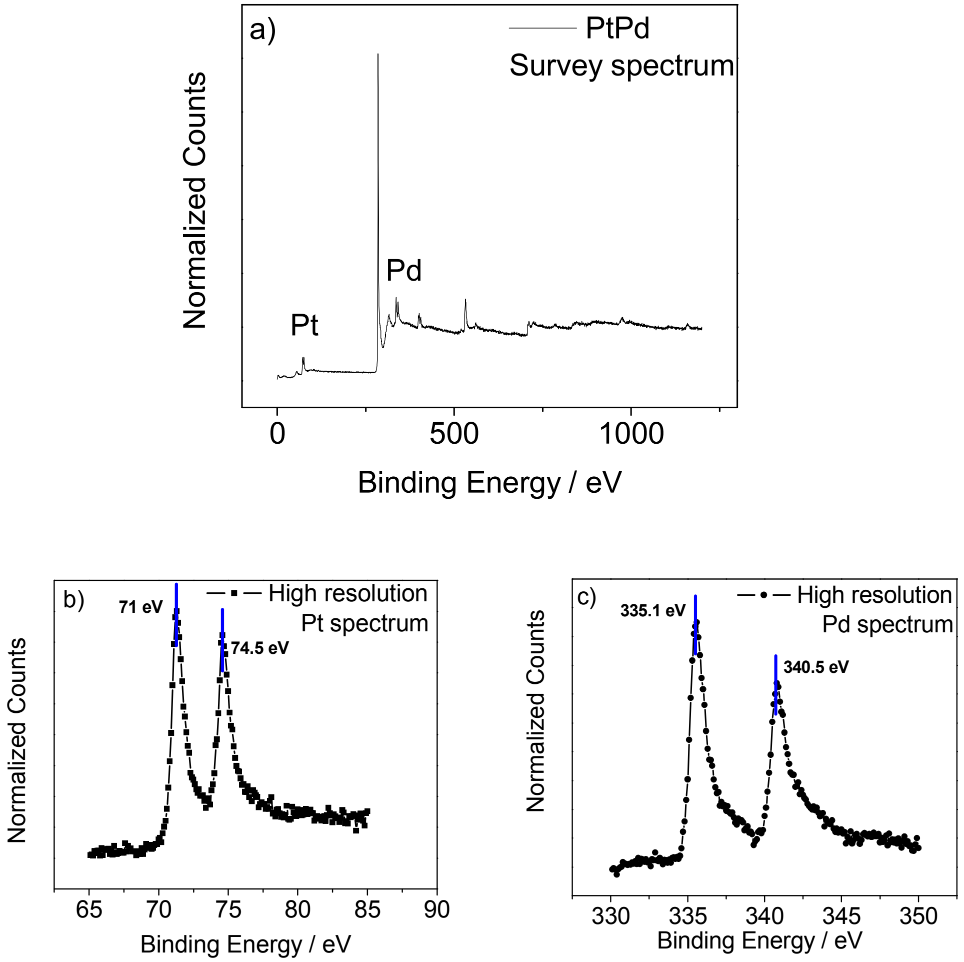

Figure 4.4 XPS spectra of PtPd supported on 6.5 % NCNTs. a) Survey spectrum of PtPd showing Pt and Pd regions. b) High resolution XPS spectrum of Pt and c) Pd catalysts supported on 6.5 % NCNTs.

attributed to zerovalent Pd. As reported by S.H.Y Lo at al,[25] the $3d_{3/2}$ peak can be fit to different oxidation states of Pd with peaks at 340.5, 341.4 and 342.6 corresponding to Pd, PdO and PdO_2. The peak at 335 eV was also fit to the same oxidation states with bands at 335.1, 336.2 and 337.2 corresponding to Pd, PdO and PdO_2. Peak fits for the PtPd catalysts were similar across the different varieties of CNT supports analyzed. High resolution spectra of the nitrogen region were compared to NCNT spectra without any catalyst loading and agreed with reported literature data[5] with respect to the position of the pyridinic, pyrrolic and quaternary nitrogen and quantitation of the corresponding nitrogen moieties.

4.3.4 TGA Analysis

Quantitation of catalyst loading amounts on the CNTs was performed by TGA. TGA analysis in conjunction with Raman spectral analysis of the amount of edge plane content in CNTs provided strong correlations to the influence of the edge plane sites on catalyst loading. For comparison purposes, data presented correspond to catalysts loaded on undoped CNT, 4 % NCNT and 6.5 % NCNT supports.

Figure 4.5 shows TGA curves of various CNTs that were subjected to the same loading protocols utilizing the same precursor mass. Control undoped CNTs, 4% NCNTs and 6.5% NCNTs studied at the same temperature range had residual iron (Fe_2O_3) mass percentages of 7 ± 1 %, 9 ± 1 % and 12 ± 1 % respectively. Subtracting the mass of iron from the final mass obtained at 800 °C, PtPd loadings of 0.9 ± 0.3 %, 4 ± 1 % and 18 ± 1 % were obtained for undoped CNTs, 4% NCNTs and 6.5% NCNTs respectively. The difference in loading was

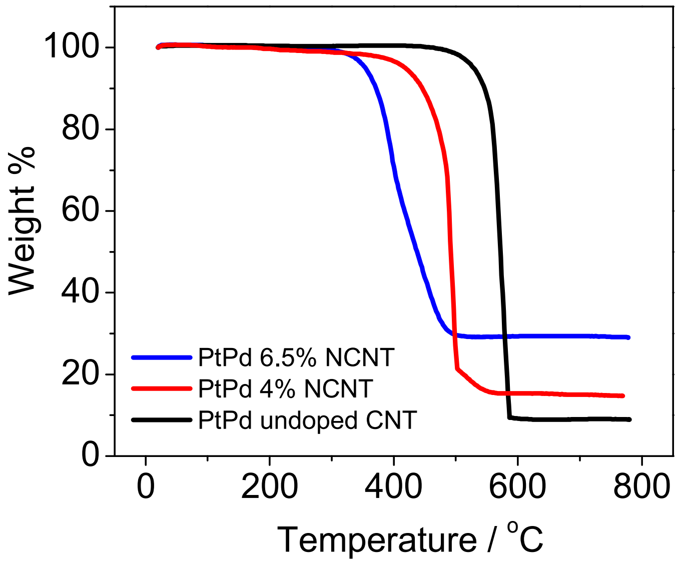

Figure 4.5 TGA heating curves for PtPd catalysts on various CNT supports

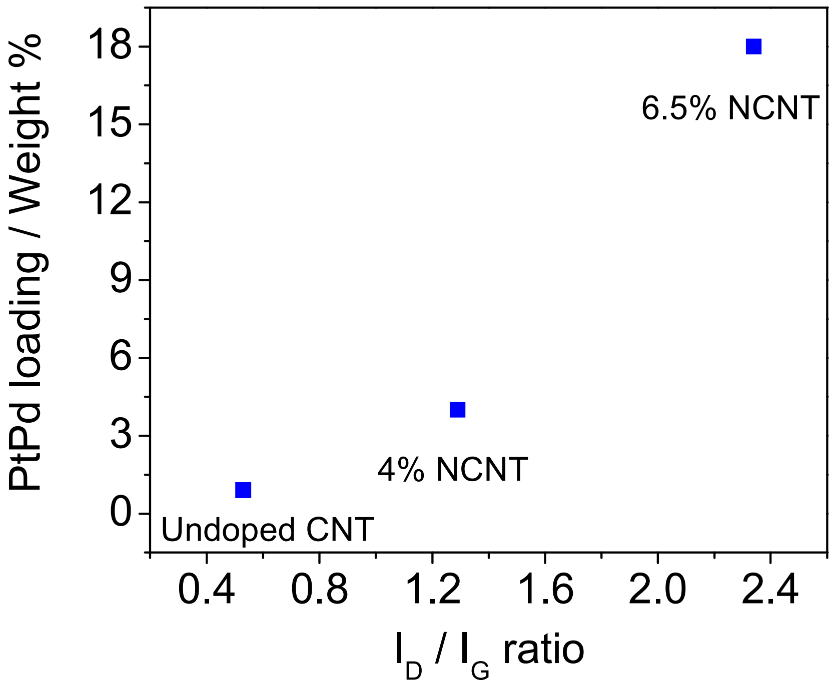

Figure 4.6 Effect of edge plane content at NCNTs on PtPd loading as determined by TGA.

directly correlated to the amount of edge plane content in the respective CNTs as shown in Figure 4.6. Careful control of TGA analysis conditions also provides insight into burn off temperatures and rates for various CNTs that can be directly correlated to the amount of disorder on the surface.[23] The measured burn off rates were slightly lower than pristine CNTs reported by Maldonado et al[5] and were consistent with literature reports.[26]

4.3.5 Electrochemical Analysis

4.3.5.1 Cyclic Voltammetry

The electroactive surface area is an important benchmark in comparing catalysts.[27] The commonly accepted method of determining the electroactive surface area (ESA) of a catalyst is the integration of charge associated with the amount of hydrogen adsorbed/desorbed on the surface of the electrode. While this method of determining the ESA is fairly accurate for Pt catalysts, it is difficult to normalize the surface areas of non noble metal catalysts and in cases of Pt based bimetallic catalysts. The adsorption/ desorption of hydrogen on the surface of PtPd is known to be particularly dependant on the size and surface composition of the catalyst.[28] Voltammograms of PtPd catalysts of varying compositions have been shown to have distinct differences in the 'hydrogen region' and subsequently lead to significant differences in the surface areas calculated through the integration of the charge associated with the adsorption/ desorption of hydrogen. Figure 4.7 shows a typical cyclic voltammogram of the PtPd catalysts supported on 6.5% NCNT. The voltammogram is similar to that of other PtPd catalysts on the nanoscale as reported in literature.[29] This voltammogram was also comparable

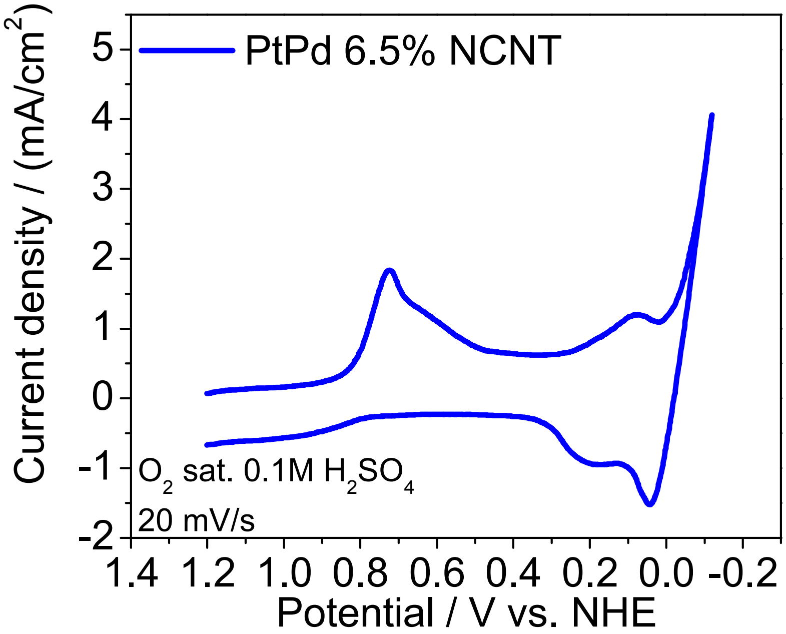

Figure 4.7 Representative cyclic voltammogram for PtPd catalysts supported on 6.5 % NCNTs in O_2 saturated 0.1M H_2SO_4.

to pure Pd catalysts and the peak near 0 V has been ascribed to the combination of hydrogen desorbed from the bulk of the metal with that of hydrogen at the surface. The peak at 0.2 V has been ascribed to the desorption of hydrogen on the surface and also in the α- phase of the Pd catalyst.[30] Grden et al[29] and Eley et al[31] have shown that the appearance of two distinct peaks related to the desorption of hydrogen suggest there are two distinct phases of adsorbed hydrogen that exist on the Pd surface that affect the ESA. ESA values calculated from hydrogen adsorption on PtPd supported at undoped CNTs, 4 % NCNTs and 6.5 % NCNTs were 1.8 ± 0.6 m^2/g, 13 ± 1 m^2/g and 56 ± 3 m^2/g respectively.

4.3.5.2 ESA Analysis by CO Stripping

With some of the inherent problems in using the hydrogen region to calculate the ESA, CO adsorption and oxidation on the surface of catalysts is an effective method that provides information on the ESA regardless of whether the catalyst is composed of noble or non-noble metals and insight into surface poisoning. Current-time transients with respect to CO oxidation at various potentials also provide insight into the effects of particle size and mechanism of CO monolayer oxidation especially with regard to OH_{ads} on the surface of the catalysts.[32] CO electro-oxidation was carried out on PtPd films drop cast on a highly polished glassy carbon (GC) RDE and dried under argon to prevent oxidation of the catalyst layer. CO stripping on PtPd catalysts deposited on 6.5% NCNT is shown in Figure 4.8 The portion of the CO stripping voltammogram in the hydrogen region was devoid of any features associated with the adsorption/ desorption of hydrogen indicating that the catalyst surface was saturated with CO.

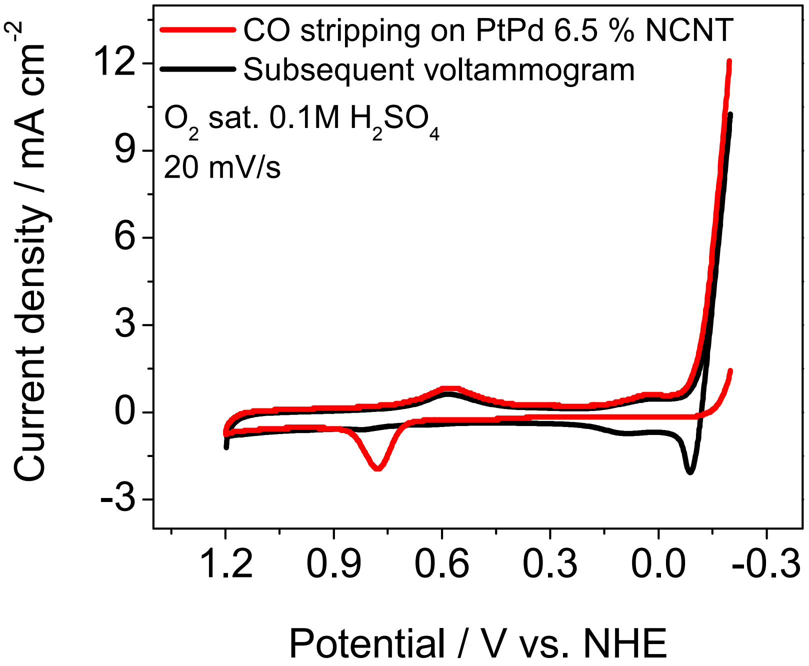

Figure 4.8 CO stripping voltammogram on PtPd catalysts supported on 6.5 % NCNTs. CO was dosed into solution for 20 min followed by 30 min of Ar purge to remove CO in bulk.

Furthermore, it was also indicative of oxidation of CO on the surface and not from the bulk solution. The peak potential and onset for the PtPd catalysts were 0.77 V and 0.65 V respectively and were found to be comparable to Pt catalysts in the same size range.[32] The feature around 0.5 V was attributed to the reduction of surface oxide. The voltammogram recorded in succession to the CO stripping showed peaks associated with the adsorption/ desorption of hydrogen and is indicative of the regeneration of the surface after CO oxidation.

ESA values calculated from CO electro-oxidation experiments were compared over three consecutive cycles and displayed no significant decrease in the surface area of the catalysts. ESA values for the PtPd catalysts estimated by hydrogen adsorption/ desorption and CO stripping are reported in Table 4.1. It should be noted that the voltammogram recorded in succession to the CO stripping voltammogram was used to calculate the charge associated with the adsorption/ desorption of hydrogen. The differences in the surface areas calculated from CO and hydrogen adsorption peaks are apparent from Table 4.1. The ESA's calculated from hydrogen adsorption/ desorption are greater than the ESA's calculated from CO oxidation because of errors associated with the integration of the amount of charge due to hydrogen adsorption/ desorption. We believe that surface areas calculated from CO stripping serve as more accurate indicators for comparison to activity benchmarks.

4.3.5.3 Chronoamperometric Studies

Chronoamperometric transients for CO oxidation on the PtPd catalysts were conducted to study the influence of the catalyst particle size on activity.

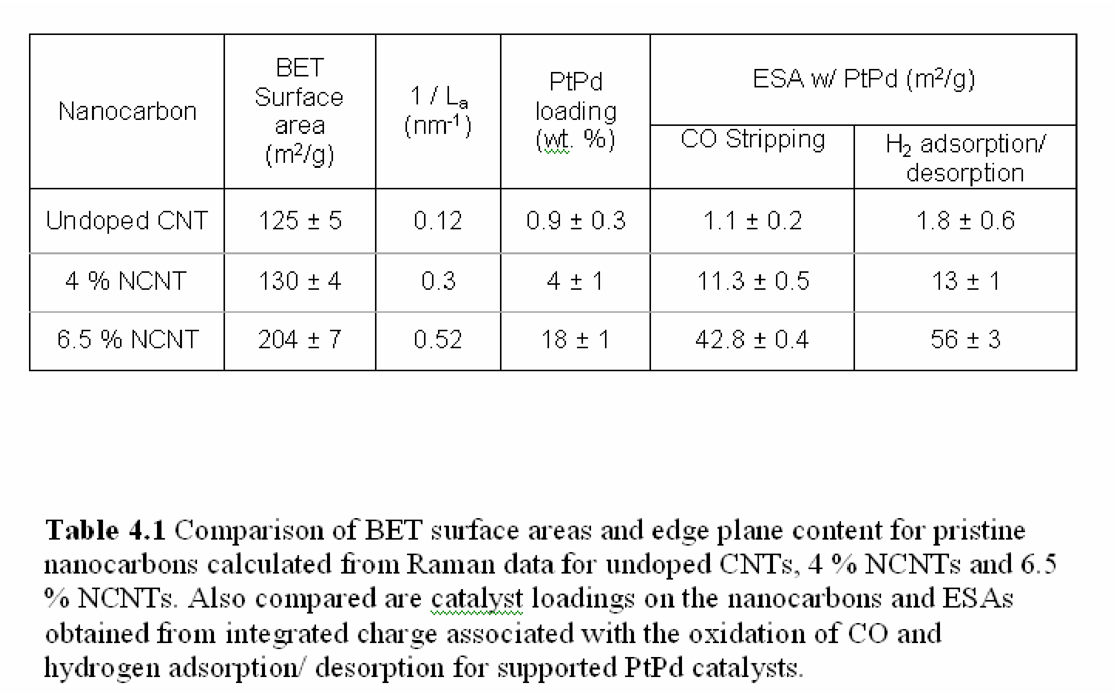

Nanocarbon	BET Surface area (m^2/g)	$1 / L_a$ (nm^{-1})	PtPd loading (wt. %)	ESA w/ PtPd (m^2/g)	
				CO Stripping	H_2 adsorption/ desorption
Undoped CNT	125 ± 5	0.12	0.9 ± 0.3	1.1 ± 0.2	1.8 ± 0.6
4 % NCNT	130 ± 4	0.3	4 ± 1	11.3 ± 0.5	13 ± 1
6.5 % NCNT	204 ± 7	0.52	18 ± 1	42.8 ± 0.4	56 ± 3

Table 4.1 Comparison of BET surface areas and edge plane content for pristine nanocarbons calculated from Raman data for undoped CNTs, 4 % NCNTs and 6.5 % NCNTs. Also compared are catalyst loadings on the nanocarbons and ESAs obtained from integrated charge associated with the oxidation of CO and hydrogen adsorption/ desorption for supported PtPd catalysts.

These experiments also provide insight into the mechanism of CO oxidation and the effect of OH_{ads} on the surface.[33] Figure 4.9 shows chronoamperometric transients for the PtPd catalysts supported on 6.5% NCNT. These transients were comparable to Pt particles of the same average size supported on GC as reported in Maillard at al[32] and show current maxima at faster time scales. This particular aspect was attributed to the presence of smaller particles less than 0.8 nm that result from the CVD process. The transients show well defined peaks for the current rise and decay[34] and the current maximum increases and shifts to faster time scales corresponding to an increase in the oxidation potential. The rise and decay of the current maxima is a subject of considerable argument due to ambiguity in attributing multistep electrochemical processes and rate limiting steps to particular characteristics of the curve, but it is generally agreed that the formation of CO_2 occurs during the initial current rise. As has been dealt with in several literature sources[35] transients were not background subtracted due to the influence of CO coverage on surface oxidation and double layer charging.

4.3.5.4 RDE Studies

The activity of PtPd catalysts and the synergistic role of the nanocarbon support were studied for ORR using RDE experiments. The carbon support plays a vital role in enhancing the activity of the catalysts prepared by the MOCVD route since the NCNTs are known to spontaneously decompose peroxide which is a byproduct of ORR.[36] ORR peak potentials were more positive for catalysts supported on NCNTs than on undoped CNTs with identical catalyst loadings.[8] RDE experiments facilitated calculations as to the efficiency of ORR on the

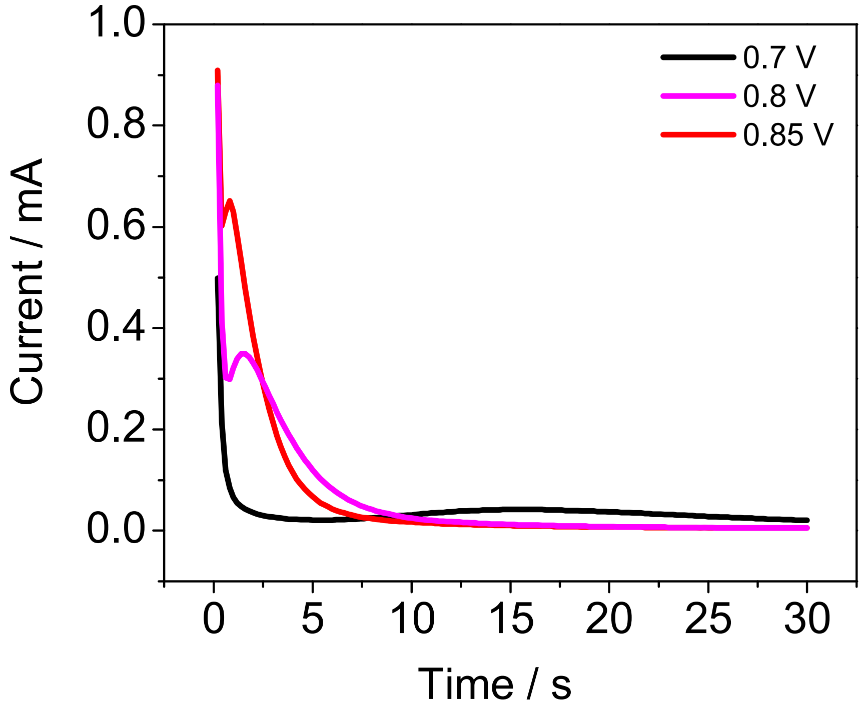

Figure 4.9 CO stripping transients on PtPd catalysts supported on 6.5 % NCNTs. CO was dosed into solution for 20 min followed by 30 min of Ar purge to remove CO in bulk. The working electrode was held at 0.11V during CO dosing and raised to stripping potentials.

catalysts and compare activities to commercial Pt values in literature. RDE polarization curves shown in Figure 4.10 for PtPd catalysts supported on 6.5% NCNT were comparable to benchmark catalyst systems. The mass transport limited current density at 1600 rpm[37] was 2.5 mA/ cm^2 which was comparable to commercial Pt catalysts on XC-72 in the same size range.[27] Koutecky- Levich plots derived from the RDE data indicate that 3.6 electrons were involved in ORR which also compares well to published literature data.[27] To account for the effects of the bisulfate in sulfuric acid, RDE experiments were carried out in 0.1 M $HClO_4$. This resulted a significant decrease in the current density of a peak shaped feature attributed to the bisulfate adsorbed on the catalyst surface as shown in Figure 4.11.

4.3.5.5 Stability of PtPd Catalysts

One of the primary advantages of MOCVD is that it allows for the synthesis of nanoparticles directly on the CNT surface without the need for templates to control size distributions of the as synthesized nanoparticles. This allows for direct interrogation of the synergistic effects of the substrate and the catalyst devoid of possible interactions with templating agents or influence from multiple synthesis and processing steps that are typically needed to design catalysts of similar size distribution. While MOCVD is a ‘soft’ chemical route that does not require heat treatment at high temperatures, the stability of these catalysts are on par with commercial Vulcan based catalysts. Figure 4.12 shows representative voltammograms for the 1st and the 50th cycles for PtPd catalysts supported on 6.5% NCNTs. It was seen that the oxygen reduction peak shifts

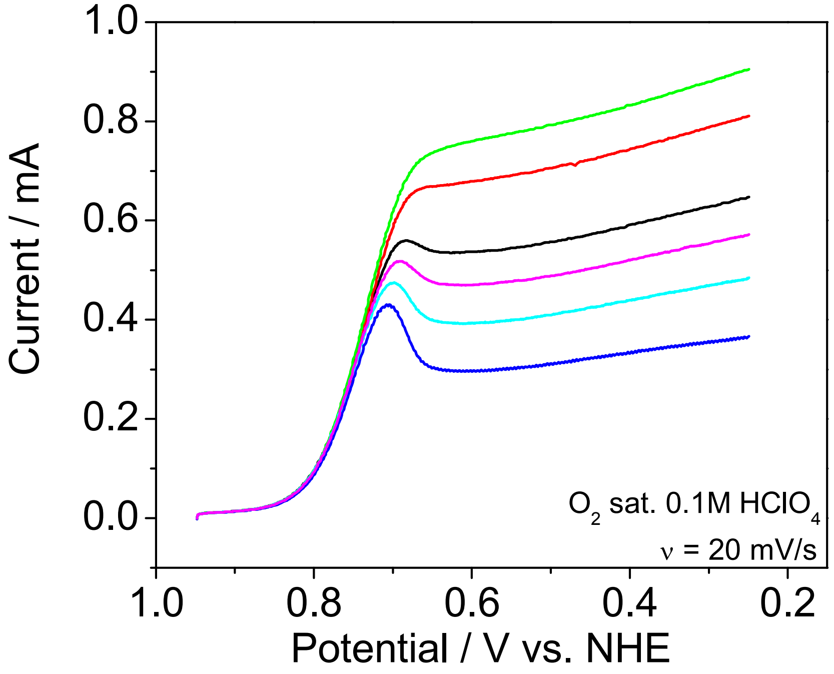

Figure 4.10 Polarization curves for ORR on PtPd catalysts supported on 6.5 % NCNTs in O_2 saturated 0.1 M $HClO_4$. The RDE was rotated between 250 – 3000 rpm in increments of 250 rpm. Scan rates were 20 mV /s.

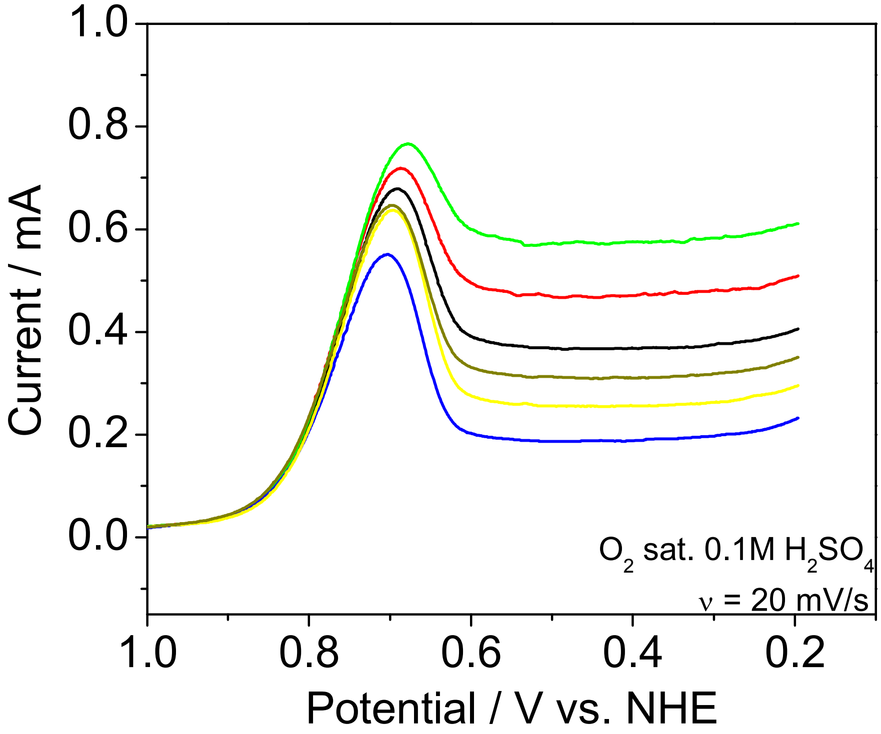

Figure 4.11 Polarization curves for ORR on PtPd catalysts supported on 6.5 % NCNTs in O_2 saturated 0.1 M H_2SO_4 showing the effects of adsorbed bisulfate. The RDE was rotated between 250 – 3000 rpm in increments of 250 rpm. Scan rates were 20 mV /s.

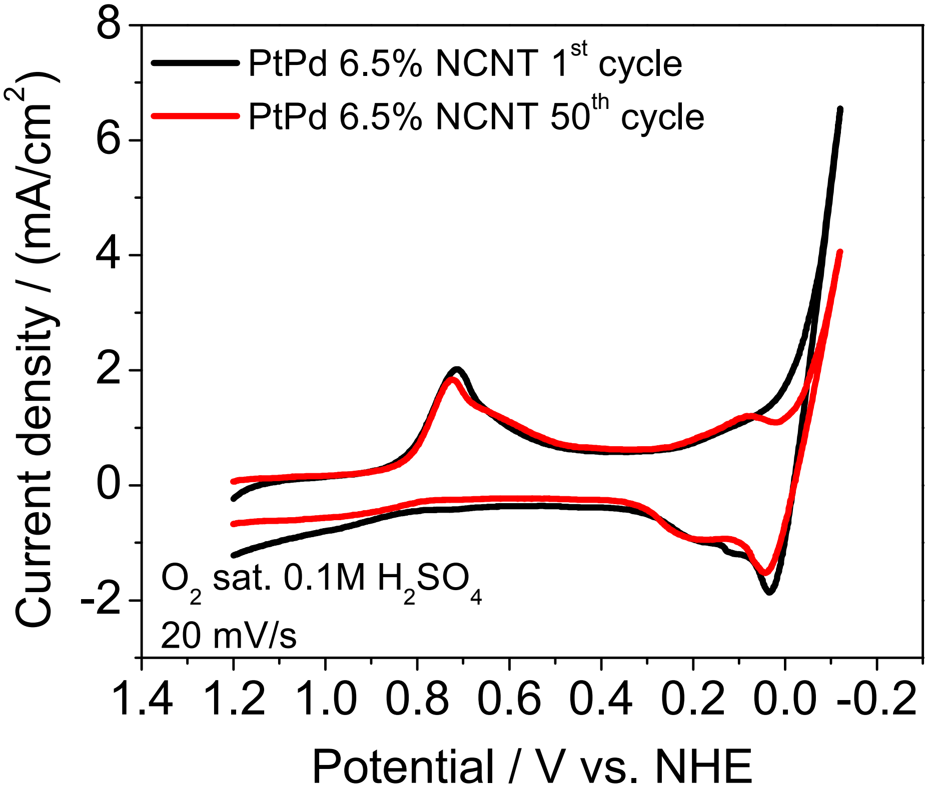

Figure 4.12 Extended cycling of PtPd catalysts supported on 6.5 % NCNTs in O_2 saturated 0.1 M H_2SO_4.

positive by 12 mV for the PtPd catalysts. This was attributed to cleansing the catalyst surface of impurities associated with the MOCVD process. A marginal decrease in the current density of 0.18 mA/ cm^2 for PtPd was also seen. This loss in current density for PtPd was attributed to the possible rearrangement of the catalyst surface. For the PtPd catalysts, the plateau observed between 0.55 and 0.7 V on the cathodic sweep was attributed to the reduction of PdO.[38] Features in the hydrogen region become more resolved over extended cycling while no significant loss was seen with the amount of charge associated with hydrogen adsorption/ desorption supporting the idea that the PtPd is electrocatalytic and stable.

4.4 CONCLUSION

In conclusion, the MOCVD scheme for preparing mono- and bimetallic catalysts directly on undoped and nitrogen doped carbon supports was shown to compare well with catalysts prepared through other processes that require a sequence of pre- and post synthesis steps. The ability to deposit fairly monodisperse catalyst nanoparticles that bind strongly to the NCNT supports and display synergistic effects on the oxygen reduction reaction was unambiguously defined through a series of experiments. The tunability of the amount of edge plane content on the nanocarbon substrate offers distinct advantages with regard to preferential catalyst loading and decomposition of peroxide specific to ORR. The MOCVD process is expected to serve as a model system for rapid and direct assembly of carbon supports and varied catalyst compositions that provide promising activity for oxygen reduction. This method of catalyst screening is expected to be straightforward for a wide variety of combinations due to the availability of thermally labile precursors for a range of different metals that show promise for ORR activity either by themselves or in multimetallic combinations. This could be taken advantage of for studies on catalyst dispersion, availability and stability in combination with a variety of carbon supports.

4.5 REFERENCES

1. Yoon, B.; Wai, C. *J. Am. Chem. Soc.* **2005**, *127*, 17174.
2. Gaur, V.; Sharma, A.; Verma, N. *Carbon* **2005**, *42*, 3041.
3. Wang, J.; Musameh, M.; Lin, Y. *J. Am. Chem. Soc*. **2003**, *125*, 2408.
4. Tian, Z. Q.; Jiang, S. P.; Liang, Y. M.; Shen, P. K. *J. Phys. Chem. B.* **2006**, *110*, 5343.
5. Maldonado, S.; Morin, S.; Stevenson, K. J. *Carbon* **2006**, *44*, 1429.
6. Maldonado, S.; Stevenson, K. J. *J. Phys. Chem. B.* **2005**, *109*, 4707.
7. Chaparro, A. M.; Mueller, N.; Atienza, C.; Daza, L. *J. Electroanal. Chem.* **2006**, *591*, 69.
8. Vijayaraghavan, G.; Stevenson, K. J. *Langmuir* **2007**, *23*, 5279.
9. Jeon, N. L.; Lin, W.; Erhardt, M. K.; Girolami, G. S.; Nuzzo, R. G. *Langmuir* **1997**, *13*, 3833.
10. Crane, E. L.; You, Y.; Nuzzo, R. G.; Girolami, G. S. *J. Am. Chem. Soc.* **2000**, *122*, 3422.
11. Lin, W.; Warren, T. H.; Nuzzo, R. G.; Girolami, G. S. *J. Am. Chem. Soc.* **1993**, *115*, 11644.
12. Serp, P.; Kalck, P.; Feurer, R. *Chem. Rev.* **2002**, *102*, 3085.
13. Crane, E. L.; Girolami, G. S.; Nuzzo, R. G. *Acc. Chem. Res.* **2000**, *33*, 869.
14. Tagge, C. D.; Simpson, R. D.; Bergman, R. G.; Hosteler, M. J.; Girolami, G. S.; Nuzzo, R. G. *J. Am. Chem. Soc.* **1996**, *118*, 2634.
15. Xue, Z.; Strouse, M. J.; Shuh, D. K.; Knobler, C. B.; Kaesz, H. D.; Hicks, R. F.; Williams, R. S. *J. Am. Chem. Soc.* **1989**, *111*, 8779.
16. Xue, Z.; Thridandam, H.; Kaesz, H. D.; Hicks, R. F. *Chem. Mater.* **1992**, *4*, 162.

17. Norman, J. A. T.; Muratore, B. A.; Dwyer, D. N.; Roberts, D. A.; Hochberg, A. K. *J. Phys. IV* **1991**, *1(C2)*, 271.

18. Powell, Q. H.; Kodas, T. T.; Anderson, B. M. *Chem. Vap. Deposition* **1996**, *2*, 179.

19. Zhu, Y.; Li, C.; Wu, Q. *Surf. Coat. Technol.* **2000**, *135*, 14.

20. Zhang, J.; Sasaki, K.; Sutter, E.; Adzic, R. R. *Science*, **2007**, *315*, 220.

21. Vahlas, C.; Juarez, F.; Feurer, R.; Serp, P.; Caussat, B. *Chem. Vap. Deposition* **2002**, *8*, 127.

22. Chen, Y. J.; Kaesz, H. D.; Thridandam, H.; Hicks, R. F. *Appl. Phys. Lett.* **1988**, *53*, 1591.

23. Cuesta, A.; Dhamelincourt, P.; Laureyns, J.; Martinez-Alonso, A.; Tascon, J. M. D. *J. Mater. Chem.* **1998**, *8*, 2875.

24. Papakonstantinou, P.; Lemoine, P. *J. Phys-Condens. Matter* **2001**, *13*, 2971.

25. Lo, S. H. Y.; Wang, Y-Y.; Wan, C-C. *J. Colloid Interface Sci.* **2007**, *310*, 190.

26. Serp, P.; Corrias, M.; Kalck, P. *Appl. Catal. A.* **2003**, *253*, 337.

27. Gasteiger, H. A.; Kocha, S. S.; Sompalli, B.; Wagner, F. T. *Appl. Catal. B.* **2005**, *56*, 9.

28. Solla-Gullon, J.; Rodes, A.; Montiel, V.; Aldaz, A.; Clavilier, J. *J. Electroanal. Chem.* **2003**, *554*, 273.

29. Grden, M.; Piascik, A.; Koczorowski, Z.; Czerwinski, A. *J. Electroanal. Chem.* **2002**, *532*, 35.

30. Pang, L. S. K.; Saxby, J. D.; Chatfield, S. P. *J. Phys. Chem.* **1993**, *97*, 6941.

31. Eley, D.D.; Pearson, E.J. *J. Chem. Soc. Faraday I* **1978**, *74*, 223.

32. Maillard, F.; Savinova, E. R.; Stimming, U. *J. Electroanal. Chem.* **2007**, *599*, 221.

33. Andreaus, B.; Maillard, F.; Kocylo, J.; Savinova, E.; Eikerling, M. *J. Phys. Chem. B.* **2006**, *110*, 21028.

34. Mc Callum, C.; Pletcher, D. *J. Electroanal. Chem.* **1976**, *70*, 277.

35. Arenz, M.; Mayrhofer, K.J.J.; Stamenkovic, V.; Blizanac, B.B.; Tomoyuki, T.; Ross, P.N.; Markovic, N.M. *J. Am. Chem. Soc.* **2005**, *127*, 6819.

36. Maldonado, S.; Stevenson, K. J. *J. Phys. Chem. B.* **2004**, *108*, 11375.

37. Climent, V.; Markovis, N. M.; Ross, P. N. *J. Phys. Chem.* **2000**, *104*, 3116.

38. Lukaszewski, M.; Czerwinski, A. *J. Electroanal. Chem.* **2006**, *589*, 38.

CHAPTER 5

Future Directions

5.1 INTRODUCTION

One of the primary factors that prevents the commercialization of fuel cells is kinetic limitations associated with the oxygen reduction reaction (ORR) at the cathode.[1] Fundamental understanding of the design, synthesis and utilization of efficient catalysts is of vital importance in addressing these limitations. Current research in the design of efficient catalysts for ORR primarily focuses on Pt based multimetallic catalysts that work in a synergistic fashion. For example, recent reports from the Adzic group[2,3] that have compared carbon supported monometallic Pt (Pt/C) and bimetallic PtAu (PtAu/C) have shown that the Pt/C catalyst loses over 45 % of its electroactive surface area after 30,000 cycles in oxygen saturated $HClO_4$. Under the same experimental conditions the bimetallic PtAu/C showed no change in the electroactive surface area. The stability of the PtAu bimetallic catalyst was attributed to the decreased oxidation of the Pt nanoparticles covered by the Au surface. Similar studies performed by Markovic et al.[4] on Pt_3Ni (111) have shown that the particular bimetallic combination was 10 fold more active than a Pt (111) surface and 90 fold more active than currently available commercial Pt/C catalysts for ORR. Strong ORR activity at the Pt_3Ni (111) surface was attributed to a highly favorable arrangement of the surface atoms that promoted weak interactions between Pt surface atoms and non reactive oxygenated species which increased the number of surface sites available for oxygen adsorption and reduction. These fundamental studies serve as good indicators for directions that need to be explored towards synthesis, characterization and utilization of efficient ORR catalysts.

The previous three chapters were devoted to the fundamental understanding of ORR at nitrogenated carbon nanotubes (NCNTs) and progress in understanding ORR activity at metal organic chemical vapor deposition (MOCVD) based and dendrimer templated catalysts supported on the NCNTs.

This chapter will focus on a three aspects of ongoing research, the first of which is related to the efficient synthetic strategies to electrodeposit mono- and multimetallic nanoparticle catalysts directly on NCNTs, second, research on characterization protocols that enable understanding of the ORR process at electrochemically dealloyed PtCu bimetallic catalysts supported on carbon that are speculated to have undergone selective Cu dissolution and finally, preliminary data from CNT supported catalysts utilized in a half cell ORR process that simulated fuel cell conditions. These experiments were carried out in collaboration with members of the Stevenson and Manthiram research groups.

5.2 RESULTS AND DISCUSSION

5.2.1 Electrodeposition of Nanoparticle Catalysts on NCNTs

The concept of electrochemical deposition of nanoparticle catalysts has been explored by a few research groups recently. Notable schemes include nanoparticles deposited electrochemically on glassy carbon (GC) substrates,[5] nanoparticles deposited on CNTs grown on carbon cloth[6] and nanoparticles deposited on CNTs cast on GC substrates.[7]

Some of the problems associated with electrodeposition on GC involve irregular dispersion of the nanoparticles on the GC surface and poor control of nucleation and growth of the nanoparticle due to difficulties in defining surface sites on the GC.[5] Difficulties in the electrodeposition of catalysts on CNTs have much in common with difficulties at the GC surfaces but can be overcome with aggressive preprocessing steps that create surface functionalities on the CNTs allowing for better anchoring, nucleation and dispersion of nanoparticles.[8] The drawback to using these preprocessing steps is that they degrade structure and composition of the CNT, leading to broad variations in stability.

The use of NCNTs is an attractive option for the synthesis and characterization of nanoparticles through electrodeposition in the face of the difficulties described above. As discussed in the previous chapters, properties of NCNTs can be controlled to a remarkable degree. Systematic manipulation of the edge plane sites and surface concentration of nitrogen facilitate controlled nucleation, dispersion and growth of nanoparticles that make active carbon/ catalyst composites for ORR.

Studies involving electrodeposition of Au and PtAu nanoparticles on NCNTs are primarily detailed in this section. These studies were conducted in collaboration with Mr. Jay Sawyer Croley at the Stevenson research lab. The NCNTs used for electrodeposition were grown directly on a nickel mesh substrate cut to specific dimensions so as to normalize the surface area as described in the experimental section in chapter 2.

Au nanoparticles were deposited on 4 % NCNTs from a solution of 0.2 mM $HAuCl_4$. A step in potential from open circuit to -0.01 V vs. NHE for 0.1 ms facilitated the electrodeposition. PtAu bimetallic nanoparticles were synthesized in a subsequent step after the deposition of Au at -0.1 V for 0.1 ms. The underpotential electrodeposition of Au on Pt is currently being explored. Figure 5.1 shows a representative chronocoulometric curve from the electrodeposition of Au nanoparticles on 4 % NCNT supports. The systematic study of the charge associated with the deposition of nanoparticles with respect to time provides a guideline that facilitates effective control of the nanoparticle size and composition.

Figure 5.2 shows representative TEM images of nanoparticles electrodeposited on 4 % NCNTs. Figure 5.2a shows that the Au nanoparticles are nearly spherical and uniformly dispersed on the NCNT surface. Edge plane sites at the NCNT surface are speculated to play a role in the uniform dispersion of the Au particles as evident by an absence of particle agglomeration. PtAu bimetallic

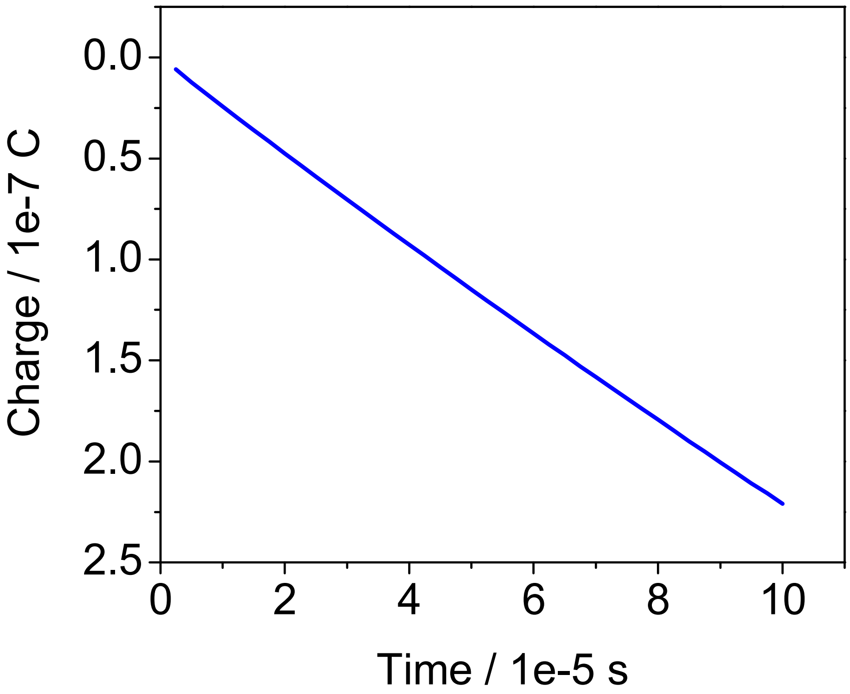

Figure 5.1 Chronocoulometric profile of the electrodeposition of Au nanoparticles from 0.2 mM $HAuCl_4$ solutions on NCNTs

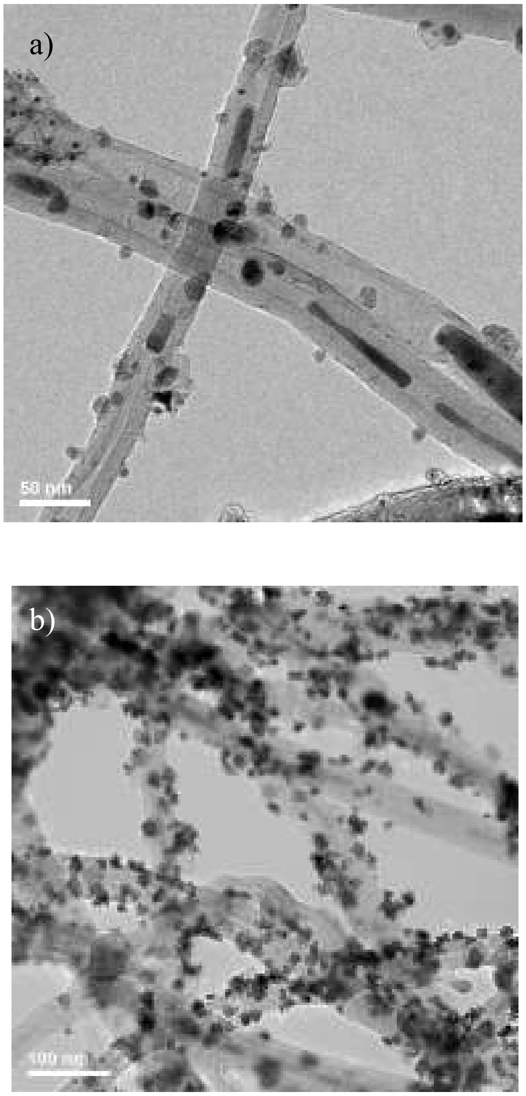

Figure 5.2 Representative TEM images of nanoparticle catalysts deposited on 4 % NCNTs. a) Au nanoparticles. b) PtAu nanoparticles.

particles shown in Figure 5.2b were found to be similarly well dispersed. A high resolution image of the PtAu nanoparticles in Figure 5.3 shows that the as deposited nanoparticles were crystalline.

The activity for ORR at the PtAu/ NCNT composites was tested in oxygen saturated 1 M KNO_3 since the NCNTs were grown on a Ni mesh substrate. Figure 5.4 shows representative cyclic voltammograms for ORR at PtAu nanoparticles supported on 4 % NCNTs. A 200 mV positive shift in the peak potential for ORR was seen at the 4 % NCNT/ PtAu composites, showing that they were active for ORR. Further studies in order to provide better control of the particle size and composition of these bimetallic catalysts are underway.

Fundamental studies on the synthesis of mono- and multimetallic nanoparticles on NCNTs through electrodeposition provide insight into direct synthetic strategies for producing active ORR catalysts. These studies also provide solutions that circumvent a majority of pre- and post processing steps required for synthesis of traditional carbon supported catalysts. For example the Adzic group used galvanostatic displacement to deposit Au on Pt which showed remarkable enhancement in ORR activity. The use of NCNTs in the electrodeposition process enables synthesis of varying compositions of AuPt bimetallic catalysts without the need for galvanostatic displacement. The electrodeposition of well defined nanoparticles without the need for expensive templating agents also emphasizes the cost effective nature of this strategy.

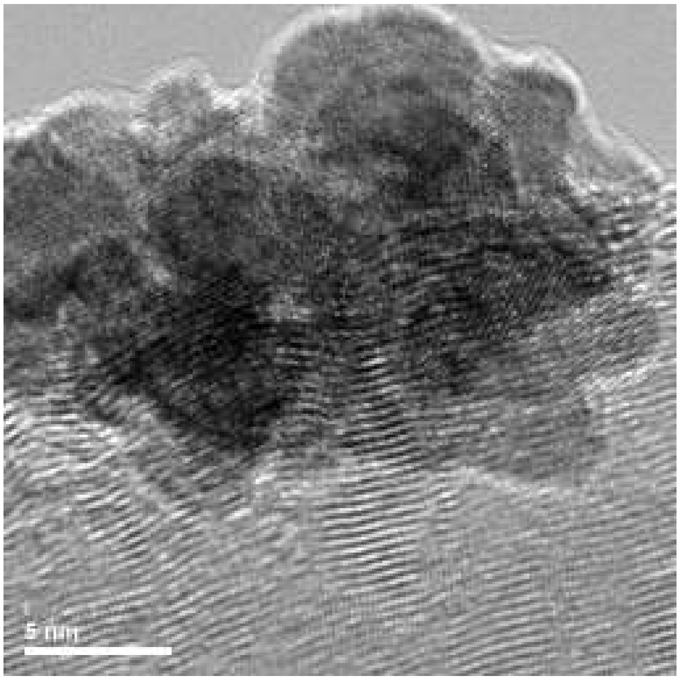

Figure 5.3 High resolution TEM image of PtAu nanoparticles electrodeposited on NCNTs.

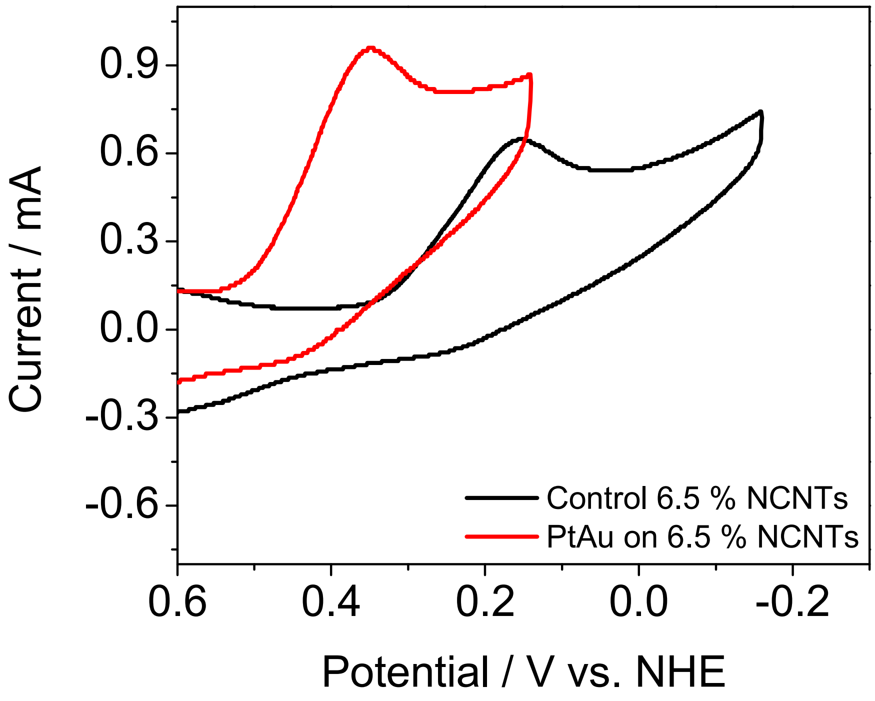

Figure 5.4 Cyclic voltammograms for oxygen reduction at PtAu catalysts deposited on NCNTs. CV's were run in oxygen saturated 1 M KNO_3.

5.2.2 Synthesis and Characterization of ORR at NCNT supported PtCu Catalysts

Selective electrodissolution of Cu atoms from PtCu bimetallic nanoparticle catalysts has been a topic of interest recently due to significant enhancement in the ORR activity at the resultant catalyst. It has been speculated that the selective electrochemical dealloying of the surface Cu atoms creates preferred structural rearrangement of the Pt atoms.[9,10] The structural rearrangements are hypothesized to include active crystal facets or favorable Pt-Pt interatomic distances that enhance the adsorption and reduction of oxygen at these catalyst surfaces.

While selective dissolution studies clearly show significant enhancement in the catalytic activity for ORR at carbon supported PtCu[9] and PtCuCo[10] catalysts, the mechanistic details still remain topics of debate. Although it has been hypothesized that dealloying of Cu does not increase the surface area of the resultant catalyst, characterization steps performed on those specific catalysts lack convincing proof to support those specific claims.

In an effort to improve upon the existing characterization data that try to explain enhanced catalytic activity at dealloyed surfaces, a set of basic measurements were made. These involved i) understanding dealloying aspects at Au surfaces through repeated alloying/ dealloying cycles with Zn. ii) synthesis of PtCu nanoparticle catalysts using dendrimer templates (as described in chapter 3) and testing for ORR activity at dealloyed PtCu dendrimer encapsulated nanoparticles (DENs) supported on NCNTs. iii) the development of new characterization strategies that enable interrogation of the PtCu catalyst surface before and after dealloying.

5.2.2.1 Fundamental Studies on Dealloying at Au Thin Films

Figure 5.5 shows an SEM image of a Au thin film after 30 alloying/ dealloying cycles with Zn. Au films were deposited on an Indium tin oxide (ITO) substrate. Electrochemical alloying/ dealloying was carried out in a standard three electrode electrochemical cell with the Au film serving as the working electrode, a thin zinc strip serving as a reference and another piece of zinc serving as a counter electrode. 1.6 M $ZnCl_2$ in benzyl alcohol was used as the electrolyte and the working electrode was cycled between -0.7 and 1.8 V vs. Zn.[11] The resultant film was found to have a roughened surface and exhibited a presence of pores created by the alloy/ dealloy process. The Au film also had a few spots on the surface where the Au had been removed from the ITO surface due to the cycling.

The difference in the electrochemical surface area for the Au film before and after the alloy/ dealloy cycling was measured by cyclic voltammetry of the film in 0.5 M H_2SO_4. The Au film served as the working electrode while a Pt wire and an Hg/ Hg_2SO_4 electrode were used as counter and reference electrodes, respectively. Potentials are reported vs. NHE for comparison. Cyclic voltammograms of the Au films before and after Zn alloying/dealloying are shown in Figure 5.6. Electrochemical surface area of the Au film was determined by integration of the charge associated with the reduction of AuO during the cathodic sweep of the voltammogram. An 17.1 % increase in the electrochemical

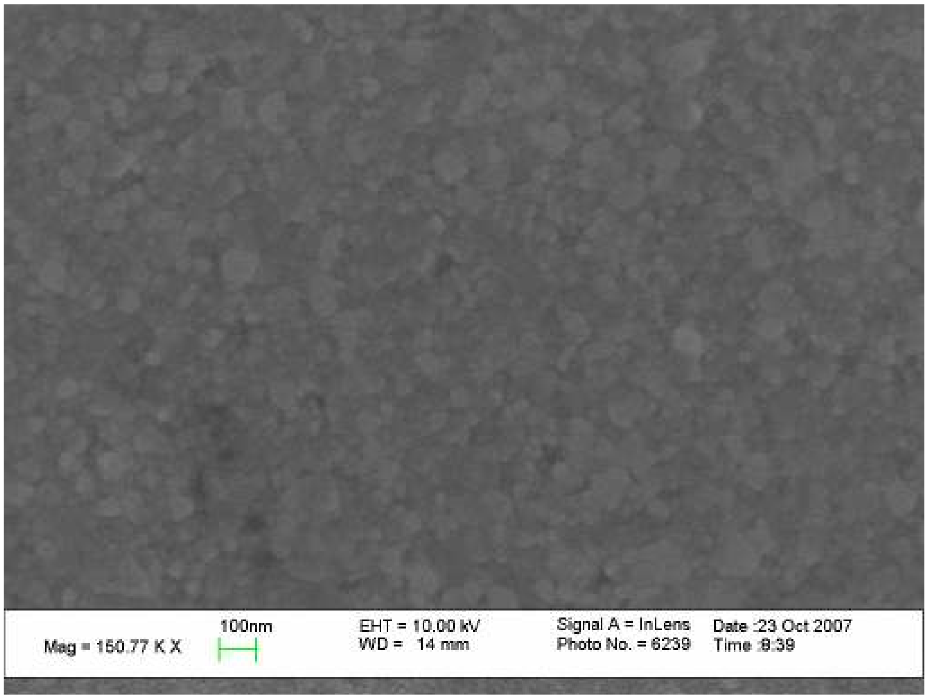

Figure 5.5 Scanning electron microscope image of Au film subjected to 30 alloy/ dealloy cycles in a ZnCl2 / benzyl alcohol solution.

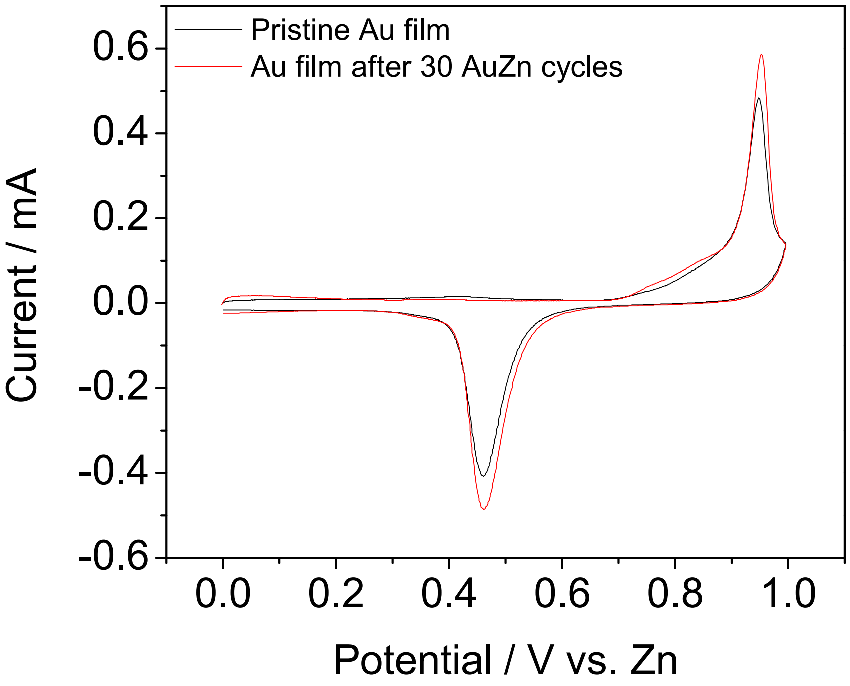

Figure 5.6 Cyclic voltammograms of an Au film in 0.5 M H_2SO_4 before and after alloying/ dealloying cycles in a $ZnCl_2$ / benzyl alcohol solution. Integration of the cathodic AuO peak showed a 17.1 % increase in the electrochemical surface area on the dealloyed Au film.

surface area was seen at the Au film after 30 alloying/ dealloying cycles with Zn. While it is clear that there is an increase in the electrochemical surface area it would be of interest from a fundamental standpoint to determine if there was an increase in the physical surface area of the resultant Au film and how the geometric surface area changes with respect to the electrochemical surface area. Studies involving spectroscopic ellipsometry in conjunction with a custom made cell that would enable toluene dosing at the Au films are planned to elucidate differences in the physical surface area as a result of alloying/ dealloying steps. These fundamental studies are expected to improve understanding of the ORR process at dealloyed nanoparticle catalysts.

5.2.2.2 Effects of Electrochemical Dealloying on ORR at PtCu DENs supported on 6.5 % NCNTs.

Preliminary studies were conducted to determine the effects of electrochemical dealloying for ORR activity at PtCu nanoparticle catalysts. PtCu DENs were prepared with assistance of Ms. Wenly Ruan. Briefly, generation 4, amine terminated dendrimers were used to coordinate with Pt and Cu ions from solution and then reduced with $NaBH_4$ to form 1.4 nm PtCu bimetallic nanoparticles. The as synthesized PtCu DENs were adsorbed onto 6.5 % NCNTs by suspending the NCNTs in the DEN solution and stirring for 12 h similar to protocols described in chapter 3.

Selective Cu dissolution from the PtCu DENs was carried out in 0.1 M $HClO_4$. A sample slurry of a measured mass of the PtCu DENs supported on NCNTs in ethanol was drop cast on a GC working electrode suspended in a three

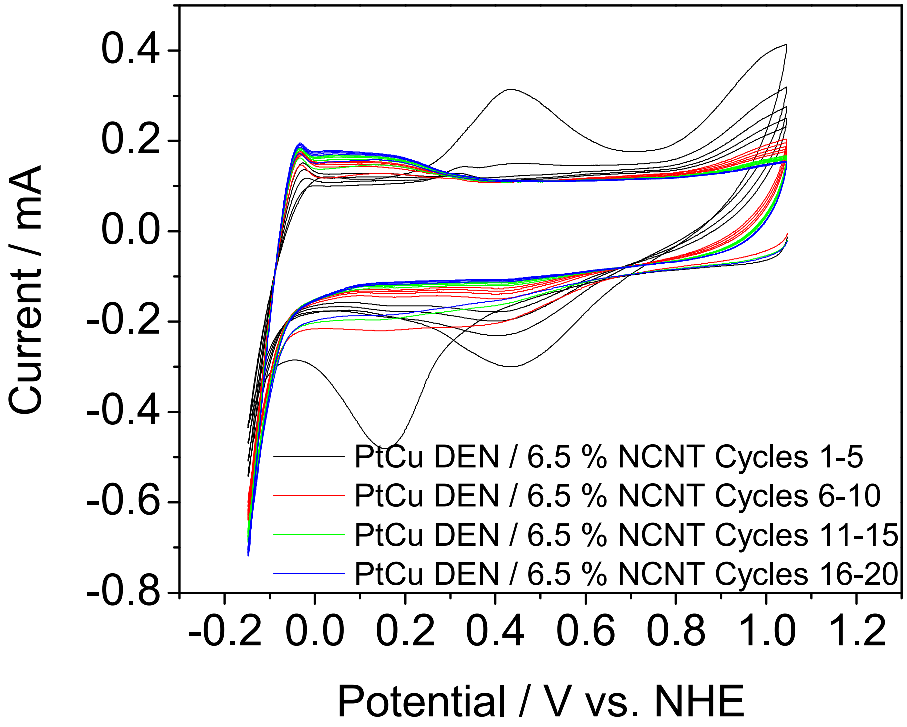

Figure 5.7 Electrochemical dissolution of Cu from PtAu bimetallic catalysts synthesized using dendrimer templates. The PtCu/ DEN catalysts were supported on 6.5 % NCNTs. Dissolution studies were carried out in 0.1 M $HClO_4$.

electrode cell with a gold counter and Hg/ Hg_2SO_4 reference. Potentials are reported vs. NHE for comparison. Figure 5.7 shows dealloying cycles 1-20 at the PtCu DENs. Features on the CV's related to the alloying and dealloying of Zn with Au compare well with literature reports on similar systems. Current densities of the peak at 0.4 V associated with the Cu decrease with the number of dealloying cycles due to the oxidation of Cu from the catalyst surface. More significantly, features associated with the adsorption/ desorption of hydrogen (0 - 0.2 V) at the Pt surface seem to increase in current density due to a larger number of Pt atoms being exposed on the surface for hydrogen adsorption/ desorption. Fundamental studies involving varied compositions of PtCu are currently being carried out to elucidate ORR activity at dealloyed surfaces.

5.2.2.3 Devising Improved Synthesis and Characterization Strategies for ORR Catalysts

While a large number of reports have delved on ORR over the past few decades, the need for effective and cost efficient catalysts still exists. Most reports have discussed empirical and applied aspects of catalysts and fuel cells but have not conducted fundamental studies that understand ORR at catalyst composites through advanced characterization strategies. Towards this end, some of the research at the Stevenson research lab has been focused on devising hybrid characterization strategies that elucidate the state of a nanoparticle catalyst before and after it is subject to ORR.

Some of the recent efforts involve the growth of NCNTs directly on customized Ni and Au TEM grids. Nanoparticle catalysts can then be incorporated on the NCNT surface either by suspending the grid in a DEN solution or by electrochemical means – similar to protocols discussed in chapter 3 and section 5.2.1. The NCNT supported catalysts might be characterized at the TEM, subject to ORR in acidic or basic media and then characterized again using the TEM. These measurements enable direct analysis of the nanoparticle surface using TEM and energy dispersive spectroscopy (EDS) before and after ORR. The size, structure and composition of the catalyst before and after ORR can be directly correlated to the corresponding activity enabling significantly better understanding of the catalysis, thereby helping design efficient catalysts.

5.2.3 CNT Supported Catalysts in Fuel Cells

CNT supported ORR catalysts were tested in a half cell configuration for oxygen reduction under simulated fuel cell conditions. These studies were conducted in collaboration with Dr. Raghuveer Vadari at the Manthiram research group. Pt DEN catalysts were adsorbed on CNTs resulting in CNT/ Pt-DEN composites that were spray coated on a carbon cloth from a suspension in nafion. A 1 cm^2 area of the thus coated electrode containing 0.05 mg / cm^2 Pt loading was tested for ORR activity in 1 M H_2SO_4.

Figure 5.8 shows a representative half cell ORR process at CNT/ Pt-DENs compared to commercial 20 wt. % Pt on Vulcan XC-72. While the current densities are lower for the CNT/ Pt-DENs, it should be noted that the catalyst loading was lower than 50 % than that at the commercial catalyst. Such studies show promise for CNT supported catalysts and further studies involving NCNT supported catalysts are planned for the future.

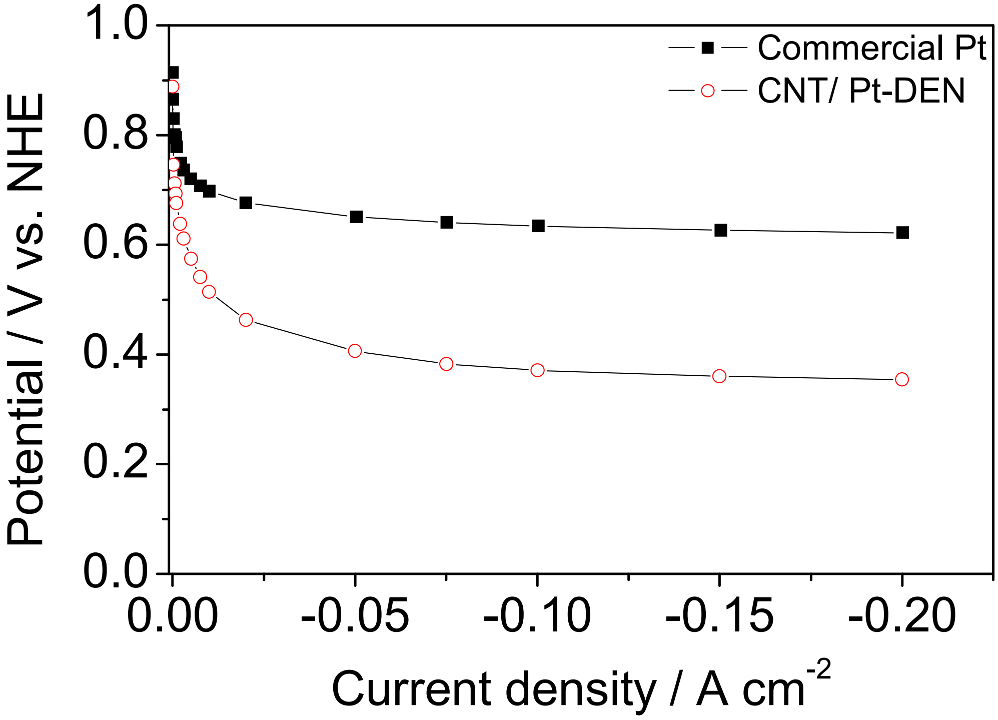

Figure 5.8 Half cell trial of CNT supported Pt DEN catalysts for ORR in 1 M H_2SO_4.

5.3 CONCLUSIONS

Efficient synthetic strategies for cost effective and active ORR catalysts have been explored through electrodeposition. Preliminary data show promise for extending these studies to different catalyst compositions that minimize the amount of Pt loading while increasing ORR activity.

Studies on selective electrochemical dealloying of bimetallic catalysts were carried out in effort to elucidate the effects of this process on ORR activity. Auxiliary studies on alloying/ dealloying at Au surfaces and studies on PtCu alloys synthesized using dendrimer templates and supported on NCNTs aim to detail changes in the catalyst surface structure, surface area and composition that correlate to enhanced ORR activity.

Preliminary half cell ORR studies on CNT supported Pt-DEN catalysts show promise for carbon nanotube supported catalysts in fuel cells.

5.4 REFERENCES

1. Gasteiger, H. A.; Kocha, S. S.; Sompalli, B.; Wagner, F. T. *Appl. Catal. B* **2005**, *56*, 9.
2. Zhang, J.; Sasaki, K.; Sutter, E.; Adzic, R. R. *Science*, **2007**, *315*, 220.
3. Strbac, S.; Adzic, R. R. *J. Electroanal. Chem.* **1996**, *403*, 169.
4. Stamenkovic, V. R.; Fowler, B.; Mun, B. S.; Wang, G.; Ross, P. N.; Lucas, C. A.; Markovic, N. M. *Science*, **2007**, *315*, 493.
5. Papadimitriou, S.; Tegou, A.; Pavlidou, E.; Kokkinidis, G.; Sotiropoulos, S. *Electrochimica Acta*, **2007**, *52*, 6254.
6. Tsai, M. –C.; Yeh, T. –K.; Tsai, C. –H. *Electrochem. Comm*. **2006**, *8*, 1445.
7. Zhao, Y.; Fan, L.; Zhong, H.; Li, Y.; Yang, S. *Adv. Funct. Mater*. **2007**, *17*, 1537.
8. Xu, Y.; Lin, X. *Electrochimica Acta* **2007**, *52*, 5140.
9. Koh, S.; Strasser, P. *J. Am. Chem. Soc*. **2007**, *129*, 12624.
10. Srivastava, R.; Mani, P.; Hahn, N.; Strasser, P. *Angew. Chem. Int. Ed.* **2007**, *46*, 1.
11. Jia, F.; Yu, C.; Ai, Z.; Zhang, L. *Chem. Mater*. **2007**, *19*, 3648.

Vita

Ganesh Vijayaraghavan, the son of Saraswathi and Vijayaraghavan Velayutham was born in Madurai, India in June 1978. After graduating from high school, he pursued a Bachelor's degree in Chemical and Electrochemical Engineering at the Central Electrochemical Research Institute in Karaikudi, India. After completion of a Master's degree in Analytical Chemistry from Texas Tech University in 2004, he joined the University of Texas at Austin to pursue his Doctorate in Analytical Chemistry under the guidance of Prof. Keith J. Stevenson.

Permanent address: 3405 Helms St #104, Austin TX 78705

This dissertation was typed by the author.